III-Sb-based solar cells and their integration on Si

Julie Tournet

▶ To cite this version:

HAL Id: tel-02171849
https://theses.hal.science/tel-02171849

Submitted on 3 Jul 2019

THÈSE POUR OBTENIR LE GRADE DE DOCTEUR
DE L'UNIVERSITÉ DE MONTPELLIER

En Électronique, Optronique et Systèmes

École doctorale : Information, Structures, Systèmes

Unité de recherche Institut d'Electronique des Systèmes - UMR 5214

III-Sb-based solar cells and their integration on Si

Présentée par Julie TOURNET
Le 21/03/2019

**Sous la direction de Éric TOURNIÉ
et Yves ROUILLARD**

Devant le jury composé de

Olivier DURAND, Professeur, INSA Rennes	Président du jury
Mustapha LEMITI, Professeur, INSA Lyon	Rapporteur
Pere ROCA i CABAROCAS, Directeur de recherche, LPICM, X	Rapporteur
Yvan CUMINAL, Maître de conférence, HDR, IES, Université de Montpellier	Examinateur
Jean DÉCOBERT, Ingénieur, HDR, III-V Lab	Examinateur
Louise HIRST, *Lecturer*, University of Cambridge	Examinateur
Éric TOURNIÉ, Professeur, IES, Université de Montpellier	Directeur de thèse
Yves ROUILLARD, Maître de conférence, HDR, IES, Université de Montpellier	Co-encadrant

UNIVERSITÉ
DE MONTPELLIER

Abstract

III-Sb materials have demonstrated their potential for multiple opto-electronic devices, with applications stretching from communications to environment. However, they remain an almost unexplored segment for classical photovoltaic systems. In this research, we intend to demonstrate that III-Sb-based devices are promising candidates for high-efficiency, low-cost solar cells. Their benefits are two-fold: not only do they offer a wide range of lattice-matched alloys and low-resistivity tunnel junctions, but they also enable direct growth on Si substrates. We thus investigate the building blocks of a $GaSb$-based multi-junction solar cell integrated onto Si. First, we develop the photovoltaic growth and processing by fabricating homo-epitaxial $GaSb$ cells. Intensity-voltage (J-V) measurements approach the state of the art with 1-sun efficiency of 5.9%. Then, we integrate a $GaSb$ single-junction cell on a Si substrate by molecular beam epitaxy (MBE). X-ray diffraction (XRD) and atomic force microscopy (AFM) analysis show structural and morphological properties close to the best reported in the literature for similar metamorphic buffers. We further adapt the cell configuration to circumvent the high defect density at the $GaSb/Si$ interface. The heteroepitaxial cell results in a reduced efficiency of 0.6%. Nevertheless, this performance is close the most recent advancements on $GaSb$ heteroepitaxial cells on $GaAs$, despite a much larger mismatch. Last, we investigate the epitaxy of $AlInAsSb$. This alloy could in theory reach the widest range of bandgap energies while being lattice-matched to $GaSb$. However, it presents a large miscibility gap, making it vulnerable to phase segregation. $AlInAsSb$ only counts few experimental reports in the literature, all referring to unoptimized growth conditions and abnormally low bandgap energies. We successfully grow good-quality layers with Al composition x_{Al} ranging from 0.25 to 0.75, showing no macroscopic sign of decomposition. Yet, transmission electron microscopy (TEM) observations point to nanometric fluctuations of the quaternary composition. Photoluminescence (PL) data is studied to determine the alloy's electronic properties. We eventually propose and fabricate a tandem cell structure, resulting in 5.2% efficiency. Quantum Efficiency (QE) measurements reveal that the top subcell is limiting the tandem performance. Numerical fits to both J-V and QE data indicate improvement paths for each building block.

ii

Acknowledgements

Looking back to these years of PhD, I realize what a journey it has been. The work presented here would not have been possible without the help of many people.

First and foremost, I would like to thank my PhD supervisor, Pr. Eric Tournie, for being such a remarkable director of research. It has been an honor for me to work under your lead and I cannot thank you enough for all your teaching in terms of science, writing skills and lab management. Thank you also for sharing your always honest views on research and society with us, young innocent researchers, and being this outgoing person I took a great pleasure working with. I particularly appreciated your availability and the good balance between research freedom and guidance you granted me. Receiving this amount of trust and support helped me gain confidence in a future research career. I would also like to acknowledge Dr. Yves Rouillard, second PhD supervisor, for his mentorship and support during the PhD. Thank you for your enthusiasm at each new result and your communicative cheerfulness. Thank you also for your help with the theory and simulations of solar cells. You helped me starting (and re-starting!) on the right solar tracks.

An equally important thank you goes to Dr. Stephanie Parola, without whom this thesis would not be half as meaningful. The considerable amount of time spent discussing the physics of solar cells really fostered my understanding of photovoltaics and helped gain a better view of our research. Also, it is encouraging for a woman in science to look up to successful dynamic models. Thank you for sharing your experience and enthusiasm with me! I am really hoping to work with you again in the future.

I am also grateful to the members of my committee for the time they dedicated to this thesis and the trip to my defense. Their comments helped me reorganize the work and push the reflexion further.

I could not have dreamed of a better environment than the NANOMIR lab for this PhD. I already miss the team and lunch break jokes. Thank you in particular to Guilhem for being my MBE companion and protector of the VARIAN. Thank you to Laurent for his helpful pedagogy and availability. A more personal thank you goes to JB for keeping me entertained and taking such good psychological care of the PhD students. Thank you for

your support managing harsh journal reviews or complex life situations! Thank you also to the clean room team, specifically Greg, Hoang, Mike, Roland, Jean, Jean-Marie and Fred for your precious insights and training. Thank you to Dilek and Marta who helped me keeping the work going even when pregnancy did not allow me to access the clean room anymore. Thank you Andrea for being the founder of the VARIAN team and keeping the gods of MBE happy for me. Thank you finally to all the other members of the team. Becoming a mother is not an easy transition in an engineering research career, especially when it keeps you away from the labs! Thank you for helping me finish the thesis on time, and cheering me up during rough times. I am particularly thankful to Zeineb for her help and support at every single step of this PhD. Thank you for your implication, despite your already busy schedule! Thank you also to the Women in Science organization of Montpellier and to my mentor, Martine Lumbreras, for the motivational and philosophical discussions we had this year.

This project has been part of the European PROMIS framework and I would like to acknowledge the European Commission for giving me this opportunity and funding this work. Bringing together all these people from different backgrounds and with complementary skills was an extremely enriching experience. I will grow deeply nostalgic of our workshops and hope to remain close to the PROMIS family. Among the fellow ESRs, I would like to particularly thank Stefano for his extensive help in setting up the cells processing and Denise for our many discussions on solar characterization (and our amazing outreach products). Thank you also to Dr. Jean Decobert for his mentorship through the PhD and even a little after. Thank you for your availability and commitment to encourage girls to get into Science! Thank you more generally to our partners in this project, especially III-V LAB, the University of Lancaster and the University of Cadiz. Thank you also to the M@csee team for sharing their expertise with us.

Of course, none of this could have been possible without the support of my family, and more particularly of my husband. Thank you for convincing me to do a PhD in the first place and always encouraging me to tackle new challenges. Thank you for supporting me even if it means relocating to the other side of the planet and being always so enthusiastic for the crazy ideas I can come up with. Thank you for reviewing my papers and listening to my presentation practices millions of times before I am finally satisfied. Thank you for

Table of Contents

vi

List of Tables

List of Figures

xiii

List of Acronyms

AFM atomic force microscopy.

AM air mass.

AM0 air mass 0.

AM1.5 air mass 1.5.

APB anti-phase boundary.

APD anti-phase domain.

ARC anti-reflective coating.

BEP beam equivalent pressure.

BG-QWTJ broken-gap quantum-well tunnel junction.

BSF back surface field.

CPV concentrated photovoltaic.

DI deionized.

EDX energy-dispersive X-ray spectroscopy.

EELS electron energy loss spectroscopy.

EQE external quantum efficiency.

FF fill factor.

FWHM full width at half maximum.

HAADF high-angle annular dark-field.

HRTEM high-resolution transmission electron microscopy.

ICP inductively coupled plasma.

IMF interfacial misfit dislocation array.

IQE internal quantum efficiency.

LWIR long wavelength infrared.

MBE molecular beam epitaxy.

MEE migration-enhanced epitaxy.

MIR mid-infrared.

MJ multi-junction.

ML monolayer.

MOVPE metal organic vapor phase epitaxy.

PDMS polydimethylsiloxane.

PECVD plasma-enhanced chemical vapor deposition.

PL photoluminescence.

PV photovoltaic.

QD quantum dot.

QE quantum efficiency.

QMS quadrupole mass spectrometer.

QW quantum well.

RHEED reflection high-energy electron diffraction.

RIE reactive ion etching.

RMS root mean square.

rpm rotations per minute.

RTA rapid thermal annealing.

SJ single-junction.

SLS strained-layer superlattice.

SR spectral response.

STEM scanning transmission electron microscopy.

TCA thermal cycle annealing.

TCG thermal cycle growth.

TDD threading dislocation density.

TEM transmission electron microscopy.

TJ tunnel junction.

TLM transmission line measurement.

UHV ultra-high vacuum.

XPS X-ray photoelectron spectroscopy.

XRD X-ray diffraction.

Chapter 1

Introduction

In this chapter, we discuss the current progress in the development of low-cost, high-efficiency solar cells. First, we tackle the global energy crisis, which is the main driver of photovoltaic (PV) research. We then give a short review of the progress made with multi-junction (MJ) solar cells and detail the fabrication methods. We present the benefits of III-Sb materials for high-efficiency MJ systems and their integration onto silicon (Si) from the perspective of lower cost. Last, we set out the objectives and strategy of this thesis.

1.1 Energy crisis and solar cells

If we are to succeed in facing tomorrow's challenges, we need to entirely rethink our modes of energy production and consumption. France, like other countries, is thus investing in the development of renewable sources of energy. The 2015 *Energy Transition for Green Growth Law* aims to increase the share of renewable energies to 32% of all electricity consumption by 2030 (only 19.6% in 2016 [2]). In order to meet this objective, renewable energies would have to make up 40% of the total electricity production [3].

1.1.1 Sunlight: a renewable source of energy

In 2009, the remaining fossil resources on Earth were estimated at 1655 Terawatt-years (TW-yr) [4]. Human activities consume 16 TW-yr yearly, but this quantity is inexorably rising with changes in industry, technology and demographics. Understandably, it is now urgent to develop new sources of energy and, preferably, they should be sustainable. For example, the solar radiation reaching Earth every year is more than 23000 TW-yr, making solar energy a very promising candidate as an alternative energy source. Admittedly, it is not a *renewable* source in that the Sun does not regenerate but, given the time scale, it can be regarded as such. The data mentioned above are summarized in Figure 1.1.
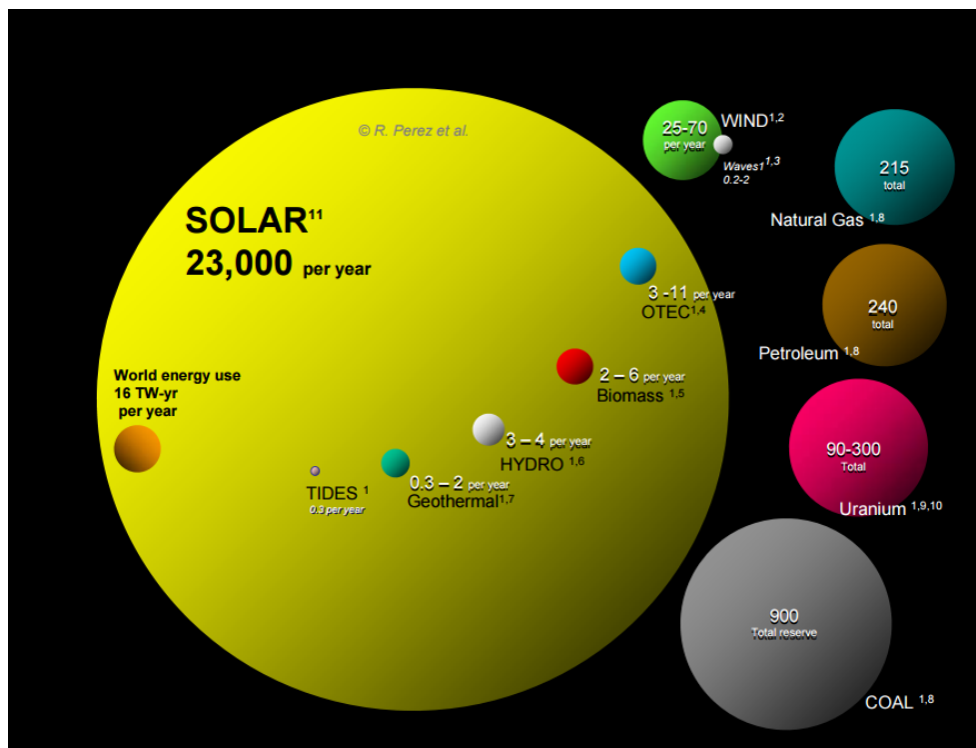
Figure 1.1: Comparison of finite (total recoverable resources) and renewable (yearly potential) energy reserves on Earth as described by [4].

1.1.2 Photovoltaic technologies

The PV effect was discovered by Edmond Becquerel in 1839. He observed the appearance of a current when shining light on silver-covered platinum electrodes dipped in an electrolyte. A few decades later, in 1873, the photoconductivity of selenium was discovered, followed by the fabrication of the first selenium solar cell in 1877. The first Si solar cell was only made about a century later, in 1954, by Chaplin, Fuller and Pearson at Bell Labs. Its efficiency was 4.5%, but this quickly improved to 6%. Solar cells started to be commercialized the next year. In 1958, a satellite was equipped with cells that operated for nearly 7 years [5]. Since the end of the 20th century, solar cell efficiency and output power has continued to improve. Today, these cells are found on rooftops and in vehicles and the number of projects to incorporate them into daily-living objects is rising steadily (*e.g.* Total's recent project to build a solar highway). Several programs have also been developed since the 90s to connect high-scale PV production modules to the electric network. Last, solar cells are still used in spatial applications: the latest Martian rover Spirit is equipped with III-V semiconductor MJ cells.

1.1.3 Photovoltaic industry

Since its emergence, the PV market has been dominated by Si-based solar cells. Despite the variety of technological innovations in the PV field, Si cells still make up 93% of the total production [6]. The most recently reported record efficiency for these cells was 26.7% [7]. In reality, their performance has not significantly improved over the last 25 years and is not likely to do so as it is approaching the theoretical maximum of 29% calculated by Shockley and Queisser in 1961 [8]. Nevertheless, the boom in Si technology has led to substantial cost reduction, as illustrated in Figure 1.2. The price drop is estimated to be about 10% a year, with current modules around $ 0.25 per watt-peak ($/W_p$) [9].

In 2017, PV energy production cost (0.055 $/kWh$, [10]) dropped below the nuclear energy production cost (0.060 $/kWh$, [11]) in France for the first time. Despite this revolution, the PV industry still lags behind other traditional sources of energy and more mature renewable energies like wind [12]. The installation prices are still considered pro-

EU spot market module prices by technology

Crystalline modules (mono-/poly-Si) average net prices (€/Wp)

High efficiency: Crystalline modules 290 Wp and above with Cello, PERC, HIT-, n-type – or back-contact cells or combinations thereof

Mainstream: Modules with usually 60 cells, standard aluminum frames, white backing and 260 Wp to 285 Wp – the majority of modules on the market

* Data up to March 10, 2019

All black: Module types with black backsheets, black frames and rated outputs of between 200 Wp and 320 Wp

Low cost: Reduced-capacity modules, factory seconds, insolvency goods, used modules (crystalline), products with limited or no guarantee

More information: www.pvXchange.com

Figure 1.2: Evolution in the price of a PV module [9].

hibitive by individual users and hinder the wide adoption of the technology. The creation of areas dedicated to the panels, other than agricultural and natural, is also problematic. As a consequence, PV energy only covered 1.9% of France's global electricity consumption in 2017 [13]. Research avenues to rectify the drawbacks include the development of high-efficiency solar cells of reduced size and cost. Not only would such cells enhance the competitiveness of the terrestrial PV industry, but it would also make an ideal source of energy for spacecraft, especially nano-satellites.

4

1.2 Development of III-V multi-junction solar cells

In the quest for high-efficiency solar cells, MJ solar cells have attracted the most attention. They are based on optimizing the exploitation of the solar spectrum by combining multiple subcells into a single solar device. Coupled to a light-concentration optical system, this type of cell can achieve high power conversion while using a reduced area.

1.2.1 The solar spectrum

Before tackling the topic of MJ solar cells, some preliminary concepts should be presented. In particular, the term solar spectrum should be clarified. This is the flux of photons received from the Sun at a certain location. In the context of PV research and depending on the application of the system, multiple solar spectra can be considered. They are determined by their air mass (AM), which evaluates the light power reduction in function of the optical path length of light through the atmosphere. By definition, air mass 0 (AM0) is the light received outside of Earth's atmosphere. It is the standard spectrum to consider for spatial applications. Other AM can be determined by:

$$AM = \frac{1}{\cos \theta} \tag{1.1}$$

where θ is the angle of the Sun from the vertical (zenith) angle. The convention for terrestrial applications, air mass 1.5 (AM1.5), is the radiation received on Earth at an angle of $\theta = 48°$. Here again, two AM1.5 should be distinguished: AM1.5D taking into account direct radiation only and AM1.5G including both direct and diffuse radiation (G stands for global). AM1.5G amounts to 1000 W/m^2. This spectrum is predominantly used in the remainder of this document.

The above-mentioned standard spectra are represented in Figure 1.3.
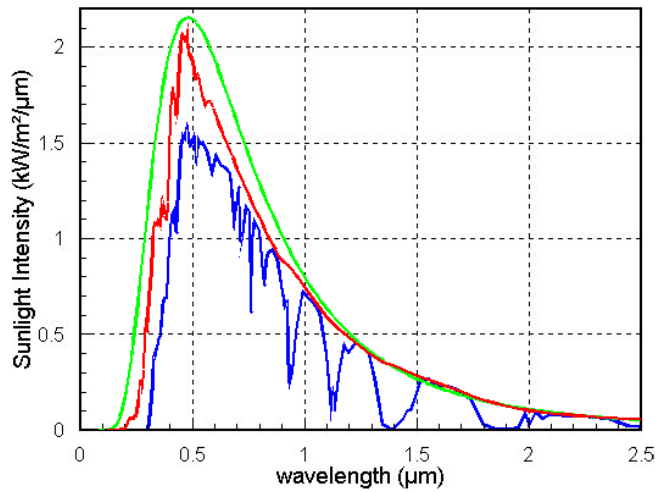
Figure 1.3: Solar spectrum outside (red) and inside (blue) Earth's atmosphere, compared to the blackbody emission (green). Source: pveducation.org

1.2.2 Overcoming the Shockley-Queisser limit

Single-junction (SJ) solar cells are not the optimal structure to achieve full-spectrum energy harvesting: a significant part of the energy is lost in these cells via carrier thermalization and photon transmission. The former refers to photons with energy that is too high with respect to the cell's bandgap that dissipate their excess energy through phonons. Conversely, the latter refers to photons with energy lower than the bandgap to which the cell's material is transparent. Taking into account these two loss mechanisms, Shockley and Queisser established a theoretical limit for SJ solar cells [8]. This limit is displayed in Figure 1.4 along with the maximum efficiency reached by various SJ cells.

MJ solar cells are based on the division of the solar spectrum into equally spanned bands to allow better exploitation of the photon flux. Each subcell has a specific bandgap energy and targets photons of the corresponding wavelength range. The subcell with the highest bandgap is placed on top of the system. When impinging the cell, photons of energy higher than the bandgap are absorbed by the top subcell, while the others go through to reach the underlying subcells. Since the top subcell filtered the very high energy photons, thermalization losses are minimized for the subsequent subcells. Once
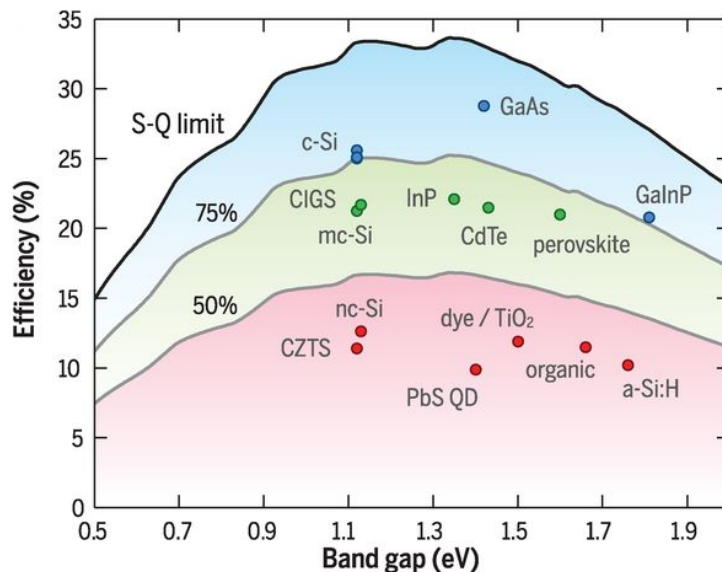
Figure 1.4: Maximum theoretical efficiencies for SJ solar cells as a function of the bandgap, also known as the Shockley-Queisser limit. The gray lines represent 75% and 50% of the limit. The best experimental efficiencies are also represented. From [14].

again, the second subcell absorbs photons with energy higher than its bandgap and is transparent to the lower energy photons. In the ideal case of an infinite number of subcells, all wavelengths are exploited and transmission losses are cut down. In reality, on top of the added design and fabrication complexity (not to mention the price) for an elevated number of junctions, other types of losses arise, especially at the interfaces. Systems with up to five junctions have been realized, for which such parasitic losses have not proven to be dominant [15]. Systems with six junctions have also shown promising preliminary results [16]. A comparison between standard Si SJ cells and high-efficiency MJ cells is drawn in Figure 1.5.

By distributing the incoming photon flux between the different closely spaced bandgaps, MJ solar cells hence minimize both thermalization and transmission losses. Different ways of connecting the subcells are possible and will be presented in the following section. It should be mentioned, however, that in the case of series-connected junctions, care should be given to current matching between the subcells. In this configuration, the net current
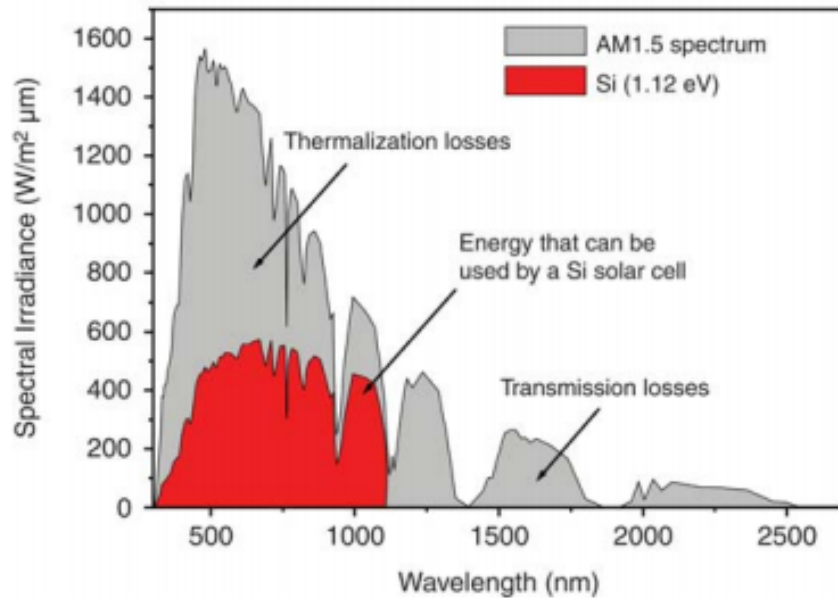
(a)
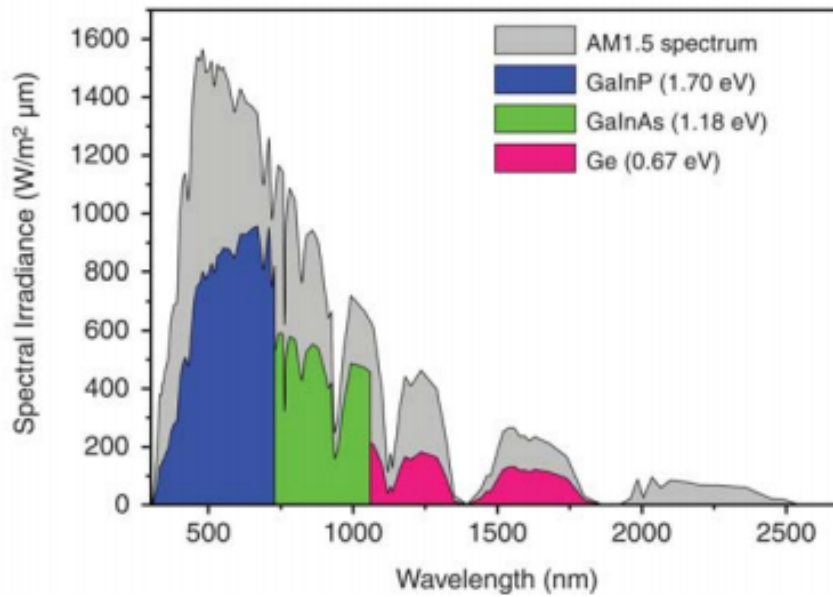
(b)

Figure 1.5: AM1.5G spectrum and the parts of it potentially converted by (a) Si solar cells and (b) $Ga_{0.35}In_{0.65}P/Ga_{0.83}In_{0.17}As/Ge$ solar cells. Taken from [17].

of the system will be bottlenecked by the minimum current flowing through the subcells. The current photogenerated in each subcell must therefore closely match the current photogenerated in the others.

1.2.3 Light concentration

Another direction to enhance cell efficiency is to concentrate the incoming sunlight onto a small area with the help of an optical system. This allows the use of smaller devices, hence it generates cost reduction. However one has to be careful about possible losses introduced by the optical system. Requirements for these systems include excellent irradiance uniformity, wide acceptance angle and high performance. Equipped with highly accurate and reliable tracking systems, concentrated systems demonstrate higher and more homogeneous energy production than traditional systems [18]. For now, such systems are not practical to install on rooftops[1] but could be of interest in the land and spatial area. Concentrated photovoltaic (CPV) systems are still a fairly new technology, without much history of production and standardization but are nevertheless a promising avenue of research for III-V solar cells.

1.2.4 Literature review

The idea of combining multiple bandgaps within a single device to optimize solar spectrum exploitation was first developed by Jackson in 1955 [19]. Early models were then developed in parallel by James and Moon [20] (Varian Research Institute), Fraas and Knechtli [21] (Hughes Research Laboratories), Bedair *et al.* [22] (Research Triangle Institute) and Cacheux [23] (Centre National d'Etudes Spatiales) in the late 70s. The first experimental demonstrations followed in 1981 and 1988, at the Research Triangle Institute [24] and the Varian Research Center [1] when an *AlGaAs* junction was stacked or grown on top of a *GaAs* junction, forming a dual-junction device.

The MJ cell developed at Varian demonstrated a record 1-sun efficiency of 23.9% under AM1.5G measured in a three-terminal configuration [1]. This was the first time that an MJ

---

[1]Possibly in the future: https://actu.epfl.ch/news/an-epfl-startup-makes-residential-solar-panels-twi/

device demonstrated a higher 1-sun efficiency than an SJ device (previous record 23.7% for AM1.5 by Spire with a single $GaAs$ junction [25]). It was grown by metal organic vapor phase epitaxy (MOVPE) and comprised an $Al_{0.35}Ga_{0.65}As$ top cell of bandgap 1.93 eV and a $GaAs$ bottom cell of bandgap 1.42 eV. The structure, shown in Figure 1.6, allows for a two- or three-terminal configuration: the metallization of the top cell bottom contact makes ohmic contact with this cell but is also shorted to the bottom cell top contact ohmic metal, bypassing the junction between the interconnect layers. The metallization extends to a busbar which allows access to this middle contact. If this middle contact is not used, the cells are simply connected in series. If the middle contact is used, on the other hand, the cells can be operated independently and no matching current condition applies.

A few years later, concurrent $GaInP/GaAs$ dual-junction cells outperformed and supplanted the $AlGaAs/GaAs$ cells in the spatial CPV industry. $GaInP$ presents the advantage of having a direct bandgap up to energies higher than $AlGaAs$, while still being closely lattice-matched to $GaAs$. Spectrolab and NREL, in particular, developed $Ga_{0.5}In_{0.5}P/GaAs$ dual cells grown on Ge substrates, which eventually turned into triple-junction $Ga_{0.5}In_{0.5}P/GaAs/Ge$ cells, achieving world record efficiency of 32.3% (AM1.5D, 440 suns) in 2000 [26]. The increased efficiency, along with the replacement of $GaAs$ substrates by low-cost, high-strength Ge substrates, made the cells compatible with large-scale manufacturing approaching the megawatt level, contributing to Spectrolab's success. Along with other technological improvements, including wide bandgap tunnel junctions (TJs) and passivating windows, the use of Ge as active layers of the solar cell further enhanced the device's efficiency. Not only did it improve the solar spectrum division between the subcells, but it also led to a better radiation hardness by reducing the relative importance of the $GaAs$ subcell. These developments contributed to a revolution in space power systems: satellites with smaller volume, hence weight, could benefit from high power sources leading to launches at lower cost. Given that cells for terrestrial applications share designs and manufacturing operations similar to those of space cells, Spectrolab demonstrated the attractiveness of MJ technology for cost-effective terrestrial CPV systems.

The following decade was marked by ever-increasing efficiencies for concentrated MJ cells, as illustrated in Figure 1.7, exceeding the 40% milestone in 2007 [27].
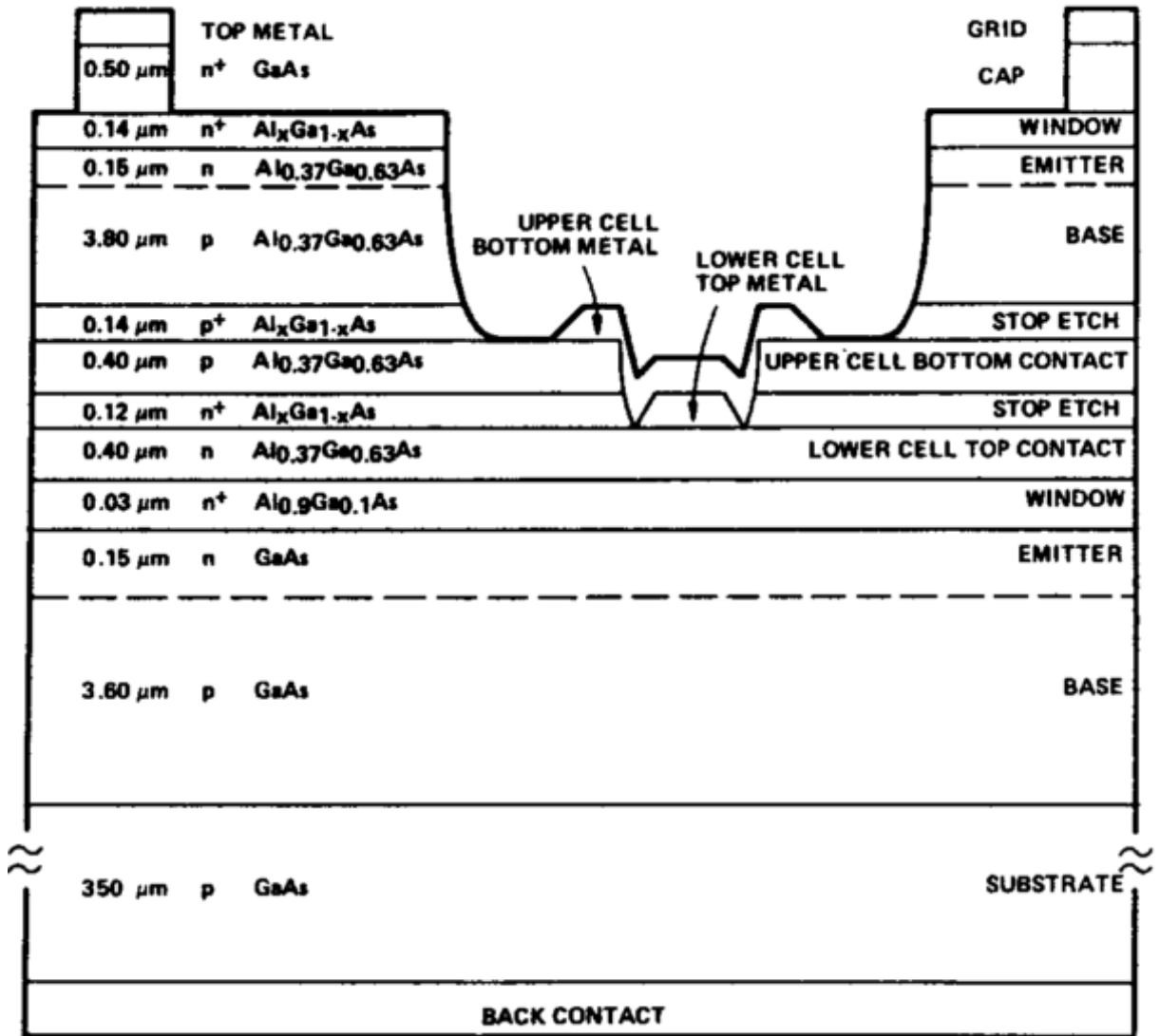
Figure 1.6: Structure of the first 1-sun record efficiency tandem solar cell [1].
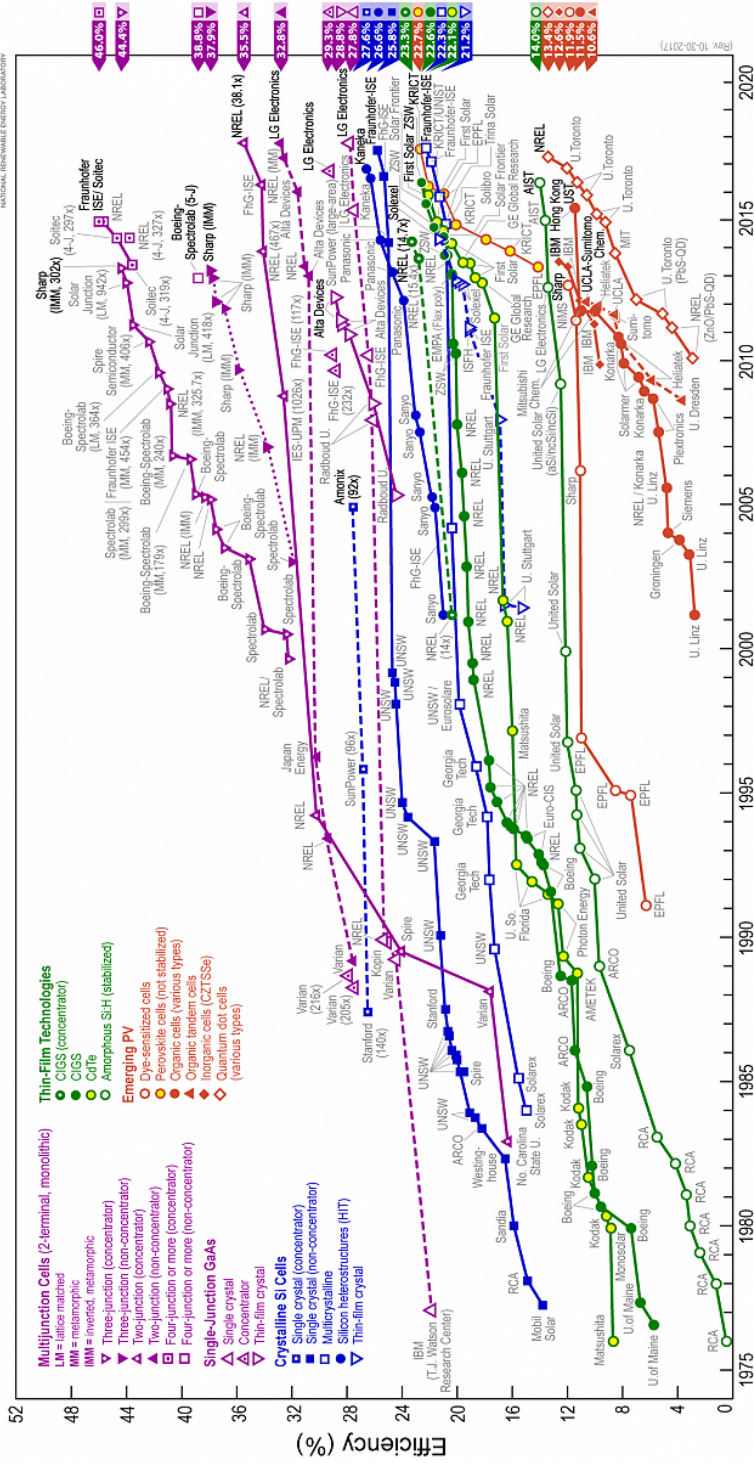
Figure 1.7: Best research cells efficiencies (source: NREL).

The current record of efficiency for a cell is held by Soitec, CEA-Leti and Fraunhofer ISE [28]. Their MJ cell converts 46.1% of solar light into electricity at a concentration of 508 suns. It is a four-junction cell made of $GaInP/GaAs$ wafer-bonded to $GaInAsP/GaInAs$.

1.3 Approaches to high-efficiency solar cells

The filtering effect of Earth's atmosphere is such that 99% of the AM1.5D reference spectrum lies between 300 and 2500 nm, covering the visible, near-infrared and mid-infrared wavelengths. Fabricating an efficient solar cell therefore requires selecting and combining materials addressing this entire spectral range. Part of the attractiveness of MJ solar cells resides in their straightforward design and optimization. Ideal bandgap energies for individual subcells can indeed be calculated to maximize the system's efficiency. In practice, however, a number of practical constraints should be borne in mind. Most suitable bandgaps often have different lattice parameters. A compromise thus needs to be found when designing a MJ device between the crystalline quality of the materials, the achievable bandgap energies and the optical losses at the interfaces. A variety of techniques, delineated below, can combine subcells into an MJ PV device. Techniques bringing together subcells originating from different substrates, known as heterogeneous integration, are presented first. The alternative is monolithic integration, where subcells are grown on top of each other on the same substrate. The ideal case is the all lattice-matched configuration, detailed in the following section. The metamorphic approach, a trade-off between design flexibility and growth-related losses, is then explained. The pros and cons of each technique are summarized.

1.3.1 Heterogeneous integration

Heterogeneous integration refers to the set of techniques by which two cells originating from different growths are assembled one on top of the other. These techniques have in common increased design flexibility as they bypass any lattice matching constraint. They are detailed in the following, each illustrated by its most recent record efficiency.

Wafer bonding

In wafer bonding, two samples are brought into close proximity in order to form atomic bonds at the interface. Such bonding requires a high-quality and smooth crystalline surface (most preferably grown epitaxially). Additional surface preparation is necessary for high-quality bonding. High doping levels should be used at the interface to ensure the low resistance of the junction. The process results in a series-connected stack of cells, which does not eliminate the need for current matching between the cells. The current solar cell efficiency record is held by a $GaInP/GaAs$ cell bonded to a $GaInAsP/GaInAs$ cell, with a total efficiency of 46.1% under 508 suns [28].

Mechanical stacking

Mechanical stacking uses an adhesive interface layer, such as epoxy, to bond together cells grown separately. The presence of impurities or inhomogeneities inherent to surface roughness at the interface can hinder the quality of the stack and incur electric losses. Preparation of the surfaces and adhesive layer are therefore crucial. The adhesive layer should be conductive if the cells are to be connected in series. It must also be transparent. The method also offers the possibility of a multi-terminal configuration, which alleviates the need for current matching between the cells. On the other hand, the resulting systems suffer from increased interface reflections and poor heat conduction. The record is held by Essig *et al.* with a $GaInP/GaAs$ dual-cell stacked on a Si cell, reaching 35.9% efficiency in a four-terminal configuration and 30.9% efficiency in a two-terminal configuration [29]. The record for series-connected cells was achieved very recently by Cariou *et al.*, also with a $GaInP/GaAs$ dual-cell stacked on a Si cell (33.3% efficiency) [30].

Transfer printing

Transfer printing uses an epitaxial lift-off to bring the subcells together. The top subcell comprises a sacrificial layer at the bottom of its active layers stack. By etching this sacrificial layer, the micro-subcell can be released (lifted) from its substrate and attached to a polydimethylsiloxane (PDMS) stamp. It is then stamp-transferred to the other subcell

on which the adhesive layer has been cast beforehand. A thin thermally conductive and electrically insulating chalcogenide layer, called a bonding agent, can be cast below the adhesive layer to further reduce losses [31]. The transfer can also be made by direct bonding without any adhesive or bonding layer [32]. Lumb *et al.* successfully used transfer printing to produce a four-terminal, five-junction cell whose mini-module efficiency was estimated at 41.2% under 744 suns (measured outdoors) [15].

Spectrum splitting

Last, another alternative method is worth mentioning: the "Very High Efficiency Solar Cell "project that DARPA has been running since 2009 [33]. The method consists of splitting the incoming light into spectrum-based sections before it reaches the cell. Each section of the spectrum is then sent directly to the most appropriate subcell. This can be done using dichroic mirrors or band-pass filters. The highest efficiency achieved with this type of cell is 39.9% in outdoor conditions, corresponding to AM1.5D, with a four-terminal $GaInP/GaAs/Ge//Si$ cell [34].

1.3.2   All lattice-matched systems

Conversely to heterogeneous integration, monolithic integration aims at growing the different subcells of a MJ on a single substrate (from the Ancient Greek *mónos*, "single" and *líthos*, "stone"). The main benefit of this technique is the augmented quality of the layers stack and its interfaces. An all lattice-matched configuration would ideally prevent the generation of misfit dislocations, point defects and resulting electric losses. To achieve this, III-V alloying offers relative flexibility for bandgap tailoring. Quaternary alloys, in particular, enable the independent setting of the bandgap energy and the lattice parameter. Such alloys, however, are subject to thermodynamic instability and decomposition. All lattice-matched systems thus face limitations related to the accessibility of the optimal range of bandgap energies. This notwithstanding, recent work has shown that they can be compensated by an appropriate choice of thicknesses to optimize the current matching between the cells [35].

High efficiencies (27.3%) were achieved as early as 1990 with lattice-matched $GaInP/GaAs$ tandem cells [36]. Such cells have recently been engineered as flexible thin-film cells and achieved an efficiency of 30.8% [37], close to the record efficiency of 31.1% obtained by Steiner *et al.* [38]. In terms of three-junction cells, Spectrolab supplanted the 1-sun record efficiency for a solar cell with a lattice-matched $GaInP/GaInAs/Ge$ triple-junction cell of 32.0% efficiency (35.2% under 66 suns) [39]. Refinements to the device processing have led to a more recent record efficiency of 41.6% under 364 suns [40]. Dilute nitrides are a promising avenue to further increase the efficiency. Solar Junction broke the world record for solar cell efficiency in 2012 with a 44.0% (942 suns) efficient three-junction made of $GaInP/GaAs/GaInNAs(Sb)$ grown on an inactive $GaAs$ substrate [41]. The two latter cells [40] [41] are in fact commercially available. Although the lattice-matched constraint, considered too demanding, has been dropped by the Fraunhofer Institute [42], dilute nitrides are still under study for the development of four- [43] and five-junction cells [44]. Last, there is growing interest in systems lattice-matched to InP. Current work still involves modeling [45], epitaxy [46] and processing [47] studies and no successful MJ has yet been experimentally demonstrated.

1.3.3 Metamorphic cells

Metamorphic solar cells draw on the compromise between maintaining a single lattice parameter over the whole structure and using the optimal bandgap energies for an MJ design. On the one hand, this type of cell makes it possible to reach better-suited bandgap energies. On the other hand, because these cells tolerate a small difference in lattice parameter, they are likely to incorporate dislocations that could hinder device performance. Careful structure design and excellent growth quality are therefore necessary for the absorption gain to overbalance the recombination losses.

Typical subcells are a few micrometers thick. At such thicknesses, the layers are fully relaxed and the strain incurred by lattice-mismatch, even slight, is released via the creation and glide of dislocations. These could be threading dislocations, propagating along the growth direction through the different layers, or misfit dislocations, elongating at the

interface. Dislocations are detrimental since they act as recombination centers for minority carriers, reducing their diffusion length and hindering the cell performance. The controlled formation of strain-relieving dislocations in a buffer layer, prior to the growth of the photoactive region, is therefore necessary. The last layer of the buffer should ideally be strain-free so that the recombination losses are minimized in the subcell. In practice, Yamaguchi *et al.* showed that a dislocation density below $3 \times 10^5 \ cm^{-2}$ was necessary to drastically limit non-radiative recombination losses in metamorphic solar cells [48]. At this dislocations density, the spacing between dislocations becomes larger than the minority carrier diffusion length, which significantly reduces the recombination losses.

The controlled formation and reduction of strain-relieving dislocations is possible using a few techniques, such as compositionally graded buffers. These buffers consist of a stack of layers whose lattice parameter progressively varies from the substrate's to the desired one. The aim of this technique is to achieve progressive strain relief by dislocation glide. If the dislocations will not realistically glide to the very edge of the wafer, they might still achieve a sufficient glide length to minimize carrier recombination. They could also encounter other dislocations and be annihilated. Kinetic models of strain relaxation by Dodson [49] and Fitzgerald [50] have shown that dislocation glide is encouraged by the material's glide velocity, a low growth rate, a high growth temperature and a low misfit grading rate (percentage of strain per thickness). It is thus strongly dependent on the choice of buffer material. It is noteworthy that using III-V compounds with an important miscibility gap is a challenging and risky task. Indeed, compositional variations across the compound and occasional phase separation can induce strain field variation in the layer, leading to increased dislocation nucleation and pinning of the existing ones. Surface roughness is another parameter that can influence the dislocation glide. Last, if located between two subcells, the buffer should be highly conductive and transparent. Careful structure design and excellent growth quality are therefore necessary for the absorption gain to overbalance the recombination losses. A more detailed description of metamorphic cell architecture can be found in [51]. The article presents two design options in greater detail: upright metamorphic solar cells and inverted metamorphic solar cells, where the subcells are grown in inverted order and the substrate is later removed. The current

efficiency record for a three-junction cell was achieved with an inverted metamorphic solar cell made of $InGaP$ (1.9 eV), $GaAs$ (1.4 eV) and $InGaAs$ (1.0 eV). It reached an efficiency of 44.4% under 302 suns [52]. For a four-junction cell, the record was once more achieved with an inverted metamorphic design using $InGaP$ (1.8 eV), $GaAs$ (1.4 eV), $InGaAs$ (1.0 eV) and $InGaAs$ (0.7 eV). The efficiency was 45.7% under 234 suns [53].

1.3.4   Comparison

The current overall efficiency record for a MJ solar cell was attained by combining multiple technologies: the cell consisted of a $GaAs$ lattice-matched $AlGaInP$ (1.9 eV) / $GaAs$ (1.4 eV) tandem, wafer-bonded to a lower InP lattice-matched $GaInAsP$ (1.1 eV) / $GaInAs$ (0.7 eV) tandem. The four-junction cell reached an efficiency of 46.1% under 508 suns [28], not far from the best results obtained by the lattice-matched and metamorphic solar cells described above. More generally, performance-wise, the heterogeneous integration methods yield results comparable to monolithic cells [54]. Heterogeneous integration offers enhanced design flexibility as it eliminates the need for lattice-matching in MJ cells. Many of the presented techniques also alleviate the need for current matching between the subcells. This is a serious advantage for terrestrial applications, where changes in illumination (realistic outdoors conditions) can have a significant impact on the efficiency of a series-connected stack. Nonetheless, this comes at the cost of increased complexity, volume and cost. Moreover, when brought under concentration, the heterogeneous interfaces may experience thermo-mechanical stress, which could hinder device performance. Other drawbacks include the potential presence of holes and unsticking parts, an increased risk of contamination compared with heteroepitaxial interfaces, and the need for very high alignment accuracy. Last, the scalability of heterogeneous techniques is limited by the size of the III-V substrate. As a consequence, the most commonly available MJ cells are monolithically grown (Spectrolab, Solar Junction). In the remainder of this thesis, we thus focus on this latter approach. Among monolithic solar cells, although metamorphic MJ cells have the highest efficiencies to date, lattice-matched cells are close behind ([41], [53]). Metamorphic solar cells allow for more flexibility when optimizing the bandgap combination. However, the buffer layer design significantly increases the growth and manufacturing complexity, volume and cost.

Lattice-matched structures are thus preferred for commercial solar cells and in this work.

1.4 Potential of III-Sb solar cells

1.4.1 Ideal bandgaps and materials systems

Detailed balance calculations [8] and augmented models [55] [56] [57] allow the estimation of the ideal bandgap combinations for MJ cells. Such combinations, optimized for AM0 (1 sun), AM1.5G (1 sun) and AM1.5D (500 suns), are represented in Figure 1.8, 1.9 and 1.10 respectively for two, three and four junctions. In the figures, each set of color bands represents the ideal bandgap combination for two, three and four junctions under a certain spectrum. More detailed results for up to six junctions are summarized in Table 1.1, 1.2 and 1.3.
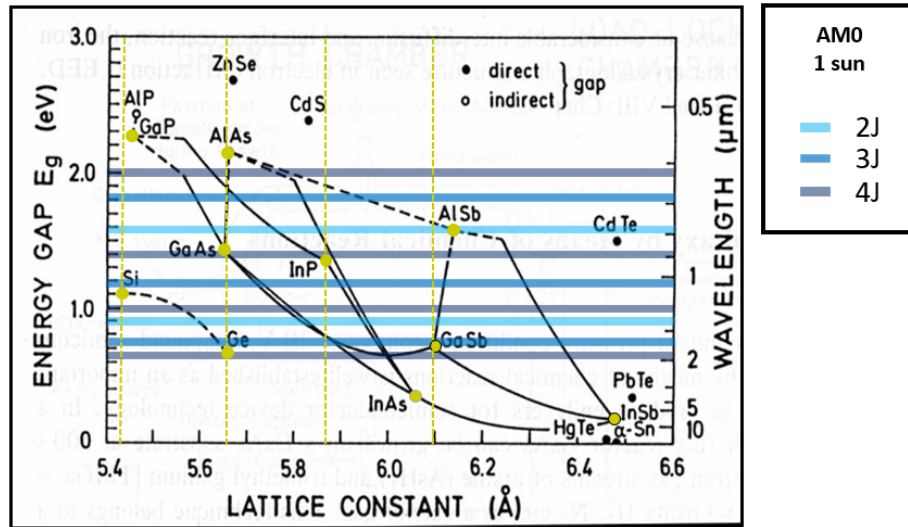
Figure 1.8: Ideal bandgap energy combinations for two-, three- and four- junction solar cells under AM0 (1 sun) as calculated by [58].
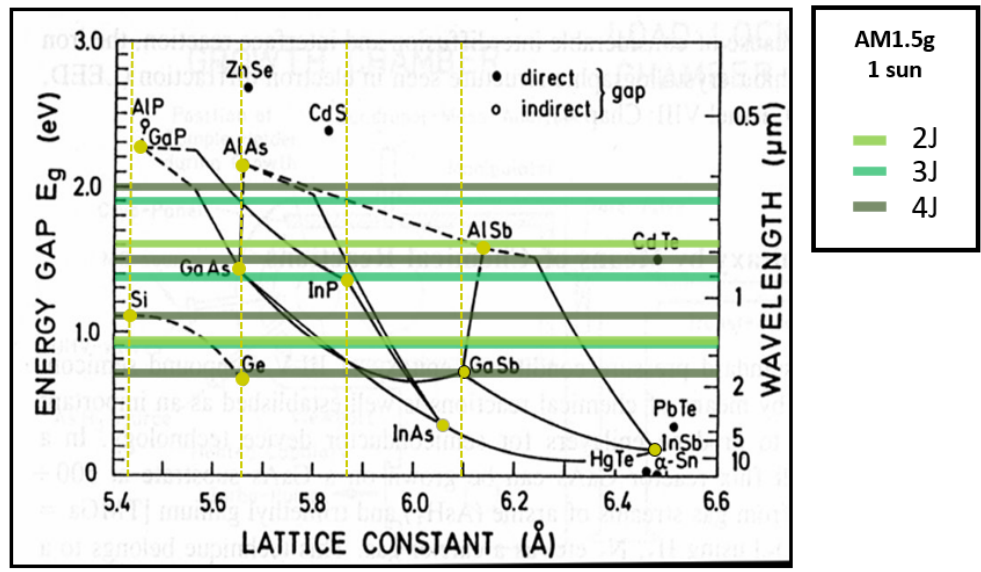
Figure 1.9: Ideal bandgap energy combinations for two-, three- and four- junction solar cells under AM1.5G (1 sun) as calculated by [58].
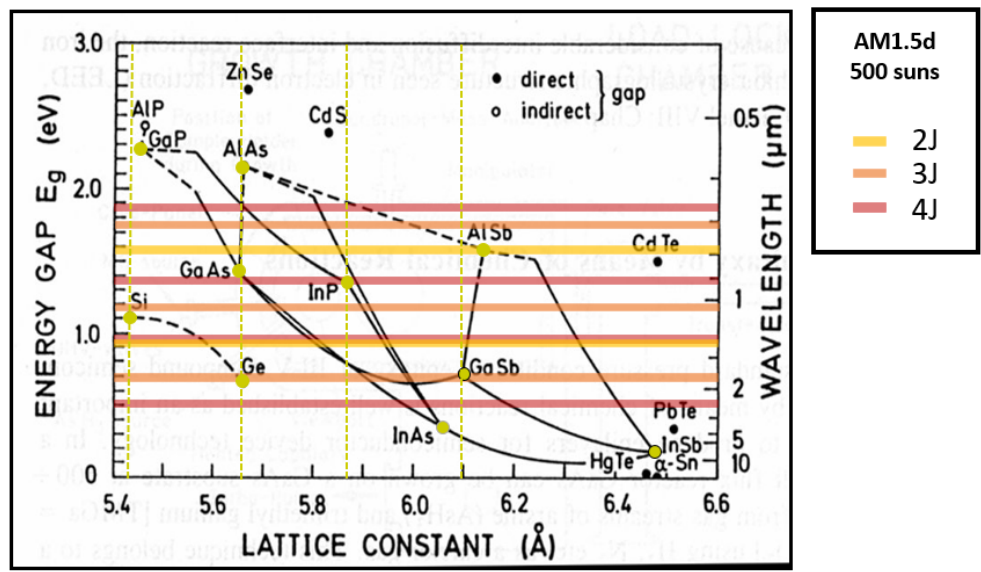
Figure 1.10: Ideal bandgap energy combinations for two-, three- and four- junction solar cells under AM1.5D (500 suns) as calculated by [58].

Table 1.1: Optimal bandgap energy combinations for one- up to six-junction solar cells under the 1-sun AM0 spectrum.

Subcell	One-junction	Two-junction	Three-junction	Four-junction	Five-junction	Six-junction
1	1.24 eV	0.89 eV	0.74 eV	0.65 eV	0.64 eV	0.59 eV
2		1.58 eV	1.18 eV	0.99 eV	0.91 eV	0.83 eV
3			1.82 eV	1.40 eV	1.21 eV	1.07 eV
4				1.99 eV	1.60 eV	1.36 eV
5					2.15 eV	1.73 eV
6						2.26 eV
Efficiency	30.3%	42.2%	48.5%	52.3%	54.8%	56.7%

21

Table 1.2: Optimal bandgap energy combinations for one- up to six-junction solar cells under the 1-sun AM1.5G spectrum.

Subcell	One-junction	Two-junction	Three-junction	Four-junction	Five-junction	Six-junction
1	1.34 eV	0.93 eV	0.93 eV	0.72 eV	0.70 eV	0.51 eV
2		1.60 eV	1.37 eV	1.11 eV	1.01 eV	0.79 eV
3			1.90 eV	1.49 eV	1.33 eV	1.13 eV
4				2.00 eV	1.67 eV	1.41 eV
5					2.14 eV	1.73 eV
6						2.19 eV
Efficiency	33.8%	45.9%	51.8%	55.6%	57.9%	59.2%

Table 1.3: Optimal bandgap energy combinations for one- up to six-junction solar cells under the 500-suns AM1.5D spectrum.

Subcell	One-junction	Two-junction	Three-junction	Four-junction	Five-junction	Six-junction
1	1.12 eV	0.93 eV	0.69 eV	0.51 eV	0.54 eV	0.53 eV
2		1.57 eV	1.17 eV	0.96 eV	0.92 eV	0.79 eV
3			1.74 eV	1.37 eV	1.21 eV	1.11 eV
4				1.88 eV	1.56 eV	1.38 eV
5					2.03 eV	1.69 eV
6						2.13 eV
Efficiency	40.3%	53.8%	61.0%	65.1%	67.5%	69.1%

It appears clearly from these calculations that the materials with the most suitable bandgaps often have different lattice parameters. In practice, the choice of the substrate will considerably confine the range of bandgap possibilities. A popular option is to choose the substrate's material as the bottom cell's material, allowing homoepitaxy of the first subcell of the structure, maximizing its quality and performance. Thereafter, selecting other subcell materials within the substrate's lattice parameter range tremendously enhances the overall efficiency. An all lattice-matched configuration would ideally prevent the generation of misfit dislocations and resulting electric losses. III-V alloys offer incomparable flexibility for bandgap tailoring. Quaternary alloys, in particular, make it possible to independently set the bandgap energy and the lattice parameter. Most alloys, however, are subject to thermodynamic instability and decomposition. Great care should thus be taken while determining their growth conditions.

1.4.2 III-Sb for high-efficiency solar cells

According to the above analysis, the design of an all lattice-matched system starts with the choice of a lattice parameter. Existing III-V material systems and their alloys are presented below.

$GaAs$

Among the available substrates, the $GaAs$ system has riveted most of the III-V PV community's attention. However, the lack of an obtainable alloy between the Ge and the $GaAs$ bandgaps hinders the capacity of such cells to exploit the full solar spectrum. Furthermore, the associated TJs require high doping levels, which remain hard to achieve.

InP

The InP material system has, in turn, been increasingly investigated. The available alloys at this lattice constant, from $GaInAs$ to $AlAsSb$, should enable reaching all ideal bandgap energies [59]. This system has long suffered from the high doping levels required by its

TJs, until recent work demonstrated that low-loss high-voltage $InP/AlInAs$ TJs can be easily achieved by MOVPE [60].

GaSb/InAs

Last, the $GaSb/InAs$ system has not yet been extensively studied within the PV framework. The highest ideal bandgap energies are out of range for alloys at this lattice parameter. Nevertheless, the use of quaternary alloys such as $AlGaAsSb$ and $AlInAsSb$ should allow access to a wide range of bandgap energies, between 0.29 and 1.64 eV [61]. The main advantage of this system is inherent to the natural broken-gap alignment of its $GaSb/InAs$ TJ, which facilitates the tunneling [62].

Comparison

The potential of the three aforementioned material systems for MJ PV is summarized in Table 1.4.

Table 1.4: Main III-V material systems for PV applications.

Material systems	$GaAs$	InP	$GaSb/InAs$
Lattice constant	5.6535 $\mathring{A}$ 5.6579 $\mathring{A}$	5.8688 $\mathring{A}$	6.0954 $\mathring{A}$ 6.0585 $\mathring{A}$
Calculated attainable direct bandgap energies	$1.42 - 1.94\ eV$	$0.74 - 1.87\ eV$	$0.29 - 1.64\ eV$
Substrate's bandgap energy at 300 K	0.66 eV (Ge) 1.42 eV ($GaAs$)	1.34 eV (InP)	0.35 eV ($InAs$) 0.73 eV ($GaSb$)
Bandgap alignment of the available tunnel junctions	Type I	Type I, II	Type III
Record mono-junction efficiency under 1 sun	28.8% [63]	24.2% [64]	5.5% [65]

From this analysis, it appeared relevant to investigate $GaSb$-based solar cells. These cells were very recently studied to serve as the subcells of MJ solar cells [15] [66]. A detailed literature review will be provided in Chapter 3. The following subsection will show another benefit of III-Sb materials for high-efficiency, low-cost solar cells: their potential for monolithic integration onto Si.

1.4.3 Integration onto Si

Motivation

Unlike Si, most III-V materials exhibit a direct bandgap. The development of technologies such as CPV has enabled the reduction in size required for a solar cell, opening new opportunities for these more expensive, yet more efficient, materials. The superior radiation resistance and thermal stability of III-V materials makes them particularly favorable candidates for solar applications in space. Also, they have lower temperature coefficients than Si: III-V-based solar cell efficiency decreases by approximately $0.2\%/^{\circ}C$ against $0.5\%/^{\circ}C$ for Si-based solar cells [67]. However, despite steady increases in their reported record efficiencies [68], III-V solar cells have faced economic difficulties in recent years [69]. The power gain that III-V cells generate does not yet balance the added fabrication costs. Although the use of solar concentrators has reduced the cost of III-V systems down to 0.59 $/W_p$ (whole module), it is still well above the 0.24 $/W_p$ of a standard Si panel [70].

The pros and cons of each material system are summarized in Table 1.5.

Table 1.5: Pros and cons of Si and III-V materials for solar cells.

Material	III-V	Si
Pros	Better radiation hardness Better thermal stability Broad range of energy bandgaps lattice-matched to a variety of substrates	Less expensive Highly available Well-known processing techniques
Cons	Expensive, although partly compensated by concentration	Indirect bandgap, hence part of the photoenergy lost through phonons emission

The option of combining the advantages of both materials is an interesting one, allowing cost reduction and facilitating higher production volumes. The monolithic integration

of III-V cells on Si substrates, in particular, is eagerly awaited. Such integration has mainly been investigated for the $InGaP/GaAs$ material system so far. Their bandgap combination, more favorable than a combination with Ge, should reach efficiencies in excess of 40% [71] [72]. However, this analysis does not take into account losses stemming from the Si indirect bandgap, the TJ or other types of interfaces, or the dislocations within the active regions. III-V-on-Si solar cells nowadays reach efficiencies in the 30% range but keep improving. A detailed description of the state of the art will be presented in Chapter 5.

III-Sb on Si

Unlike arsenides [73] [74] [75] [76] [77] [78] and phosphides [79] [80], antimonides have received only limited attention in the context of PV research. This is mainly due to their complex growth conditions (narrow growth temperature window) and interface chemistry. Moreover, the theoretical ideal single-junction efficiency of $GaSb$ and $InAs$ cells is less advantageous than their $GaAs$ counterpart (*cf* Figure 1.4). The limited attention is particularly true in the case of III-V-on-Si solar cells, yet III-Sb materials have already demonstrated their potential for other integrated opto-electronic devices [81] [82] [83] [84]. Such materials take advantage of the creation of a 90° misfit dislocation array when using an $AlSb$ initiation layer on the Si, as illustrated in Figure 1.11 [85]. This interfacial misfit dislocation array (IMF) efficiently relieves the strain at the interface. IMF have also been studied in other highly mismatched material systems, such as $InAs/GaAs$ [86] and $GaSb/GaAs$ [87].

Akahane *et al.* also highlighted the contribution of the $AlSb$ nucleation layer in terms of surface morphology [88]. Rodriguez *et al.* further enhanced the template material quality, lowering the full width at half maximum (FWHM) value down to 235 $arcsec$ for a 1 μm $GaSb$-on-$AlSb$-on-Si layer, close to the values obtained for similar thicknesses of Ge-on-Si [89] and $GaAs$-on-Si [90]. This is in spite of a significantly larger lattice-mismatch between the III-V compound and the Si ($\approx$ 12% $vs \approx$ 4% for Si). Threading dislocation densitys (TDDs) in the 10^9 cm^{-2} range were evaluated for these thin samples [91]. We thus believe such materials constitute a promising alternative to explore for the monolithic integration of III-V solar cells onto Si.
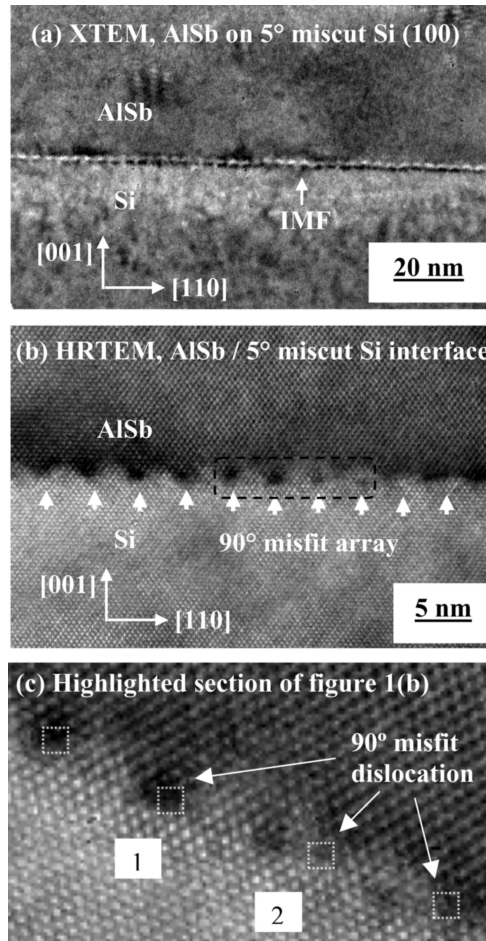
Figure 1.11: Transmission electron microscopy (TEM) images of *AlSb* grown on 5° miscut *Si* (001) substrate under (a) low-resolution and (b) high-resolution conditions. (c) is a close-up of the section highlighted in (b). All three images feature an interfacial misfit array. Taken from [85].

1.5 Objectives and organization of the thesis

1.5.1 Summary

In this chapter, we discuss the advantages of the PV resource as a key element of the energy transition. We show that, in spite of tremendous progress in terms of production costs, the PV industry still lags behind more conventional sources of energy or other mature renewable

energies. Efforts have thus been put into the development of high-efficiency solar cells and their integration on cheaper and more accessible substrates. We present several approaches to these high-efficiency and low-cost solar cells. More specifically, we give an overview of MJ solar cells and their fabrication techniques. We also show that, although heterogeneous integration methods yield slightly higher efficiencies, they add to the complexity and cost of PV systems. This has motivated the choice of an all lattice-matched system for this thesis work. We further discuss the benefits of the $GaSb/InAs$ material system for solar cells. The wide range of achievable bandgaps it provides, combined with its low-loss TJ, make this material system a very strong candidate for an all lattice-matched MJ structure. Moreover, it offers the possibility of combining the high efficiency of III-V materials and the mature Si technology platform. We show the potential of III-Sb integration on Si by direct growth, taking advantage of the formation of an interfacial misfit array to reduce the density of dislocations. We have thus decided to explore this option to make high-efficiency and low-cost solar cells.

1.5.2   Objectives and organization

The aim of this thesis is to evaluate the potential of III-Sb materials for high-efficiency solar cells and their integration onto Si. We aim to propose an all lattice-matched MJ solar cell, directly grown onto Si. The objective is particularly to demonstrate all the building blocks of such a system. Thus, we will first present the elaboration and characterization of a stand-alone $GaSb$ solar cell. Second, we will tackle the topic of III-Sb MJ cells. In particular, we will present the growth and characterization study of the $AlInAsSb$ quaternary alloy, chosen as the base material for higher efficiency cells. Next, we will describe our progress on monolithic integration of such a cell on Si. The final chapter will draw a conclusion on the potential of III-Sb-based materials for III-V-on-Si solar cells.

Chapter 2

Experimental details

2.1 Material growth and characterization

In this section, we introduce the growth and material characterization tools. We provide basic information about their operation, along with a description of the equipment used in this project.

2.1.1 Molecular beam epitaxy

Molecular beam epitaxy (MBE) is a deposition technique where high-purity molecular beams are directed at a substrate under ultra-high vacuum (UHV). The atoms adsorb, diffuse, nucleate on the surface or incorporate at kink sites, forming a high-quality film called epilayer, or re-evaporate. The growth process kinetics can be appreciated through a set of quantitative parameters such as the arrival rate, the thermal accommodation coefficient and the incorporation rate of the deposited atoms to the surface. Many books exist in literature that will satisfy the reader's curiosity for further detail on technical information [92] [93] [94] [95].

The MBE reactor used in this project, the Varian GENII system, is composed of three modules presented in Figure 2.1. Each module is equipped with its own pumping system

and is separated from the others by UHV gate valves.
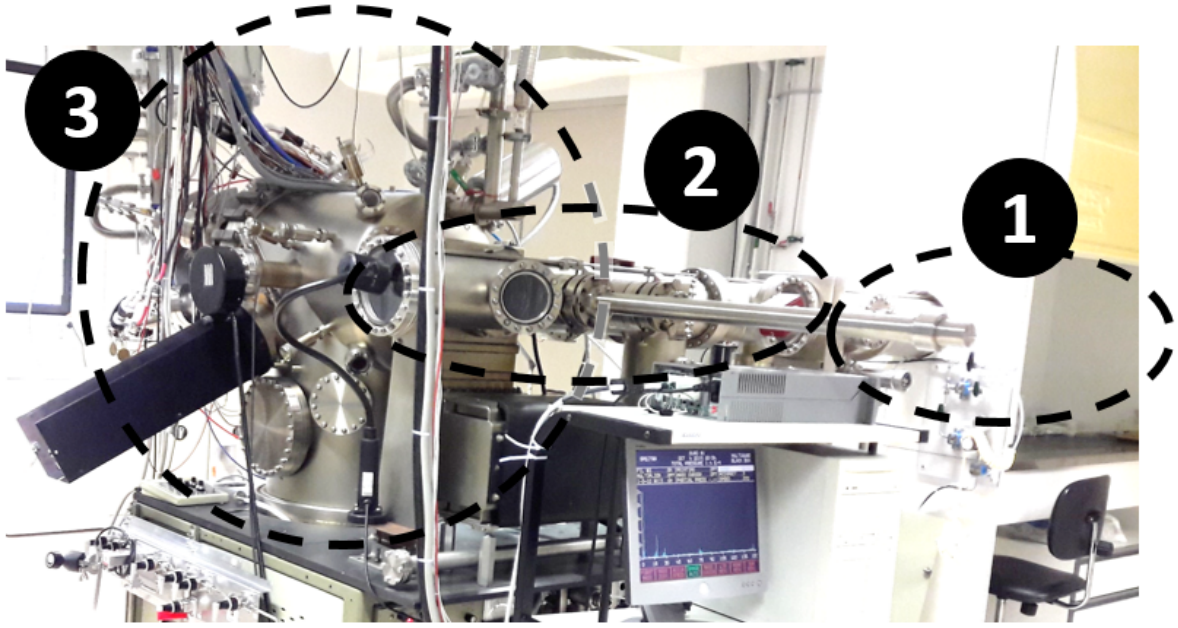
Figure 2.1: Varian GENII MBE system of the University of Montpellier MBE Laboratory. Zone 1 is the load-lock, zone 2 the buffer and zone 3 the growth module.

Group-III beam equivalent pressure (BEP) were cross-calibrated with reflection high-energy electron diffraction (RHEED) oscillations and X-ray diffraction (XRD) measurements from $AlSb/AlAsSb$ and $InAs/InAsSb$ superlattices to provide the growth rate-flux characteristics of the MBE apparatus. The substrate temperature was measured with cross-calibrated thermocouple and pyrometer and confirmed with the $GaSb$ (001)–(2×5) to (1×3) change of reconstruction, as observed with RHEED [96].

2.1.2   Reflection high-energy electron diffraction

RHEED makes it possible to monitor the growth process with accuracy: it can provide information on the growth rate, surface reconstruction, as well as surface roughness. RHEED

uses an electron gun to send high-energy electrons at a grazing incidence to the substrate. For the system used in this project, the electron acceleration voltage can be set in the range $0.5 - 30\ kV$, its intensity $0.01 - 100\ \mu A$, enabling a focus spot on the substrate smaller than $100\ \mu m$ (minimum $50\ \mu m$). In the experiments described here, the voltage was maintained at $30\ kV$ and the intensity at $1.8\ \mu A$. Thanks to their wave character, the electrons are diffracted off the surface and form characteristic diffraction patterns on the phosphorescent screen on the other side of the chamber. For rough surfaces, thanks to the very small angle of incidence (from about $0.5°$ to $5°$), the electrons penetrate volumetric surface features, which produce diffraction typical of TEM, *i.e.* individual diffraction spots characteristic of the $3D$ crystalline structure of the layer. In the case of smooth crystalline surfaces, the surface reconstruction can be inferred from the analysis of the diffraction patterns. The spacing between the streaks on the fluorescent screen is inversely proportional to the size of the unit cell of the reconstructed surface in the direction perpendicular to the beam incidence direction. Furthermore, it has been discovered by J.J. Harris [97] that the intensity of individual spots forms damped oscillations resulting from periodic smoothing and roughening of the surface as individual atomic layers are being deposited. These oscillations give direct measure of the growth rate since their period corresponds to the growth of 1 monolayer (ML). The exact characteristics of these oscillations are still a hot debate but RHEED studies in MBE have underpinned much of a progress in surface science over the past four decades. RHEED oscillations are often used to calibrate the growth rates. In close feedback, they can be used to control the layer thickness to a fraction of atomic layer.

2.1.3   X-ray diffraction

XRD is the technique of choice to study the structural properties of crystals, as described in [98] or [99]. An XRD system is comprised of an X-ray source, a beam conditioner to control the beam wavelength and divergence, a goniometer to manipulate the sample, a detector to measure the intensity of the scattered X-ray beam and a collimator to limit the divergence of the measured beam. When impinging the sample's surface, the incident rays are diffracted by the different crystal planes (rows of atoms). The scattered rays can

interfere with each other. The condition for constructive interferences for a beam scattered by parallel lattice planes is known as Bragg's law and can be written as:

$$2d \sin \theta = n\lambda \qquad (2.1)$$

with n an integer, d the interplanar spacing between adjacent parallel planes, θ the incidence angle on the substrate and λ the ray wavelength. The diffraction pattern of a single crystal thus displays a line at the so-called Bragg reflection angles, satisfying Equation 2.1.

Figure 2.2 presents the rotation axis of a typical XRD system. In particular, the incident angle ω is defined between the X-ray source and the sample surface. The angle 2θ is the angle between the incident beam and the detector axis. ϕ is the rotation angle around the substrate's normal. Different scan modes are possible. The ones used in this project are:

- Coupled scan: plot of scattered beam intensity *vs* 2θ while varying ω so that $\omega = \frac{2\theta}{2}$ at anytime. A coupled scan shows intensity peaks whenever ω fulfills Bragg's law. Each peak can be ascribed to a specific phase by computing the interplanar spacing from the peak position using Bragg's law. The potential shift of a peak from its expected position reflects the layers' strain or tilt with respect to the substrate surface. So-called symmetric scans only reveal planes parallel to the substrate surface. Asymmetric scans, where the sample is tilted compared to the substrate's normal ($\omega = \theta + \chi$), can be used to measure different crystallographic directions.

- Rocking curve: plot of scattered intensity *vs* ω, keeping 2θ constant. In a rocking curve, the detector is parked at a determined Bragg angle and the sample is tilted so as to vary ω. If the material is a perfect single crystal (perfect parallelism of the planes), only one set of parallel planes will generate a Bragg reflection and a very sharp peak will be observed. However, if the substrate is made of multiple crystallites slightly tilted with respect to each other, a broader peak will be observed. Such disruptions in the perfect parallelism of the atomic planes can result from dislocations, mosaicity and curvature.
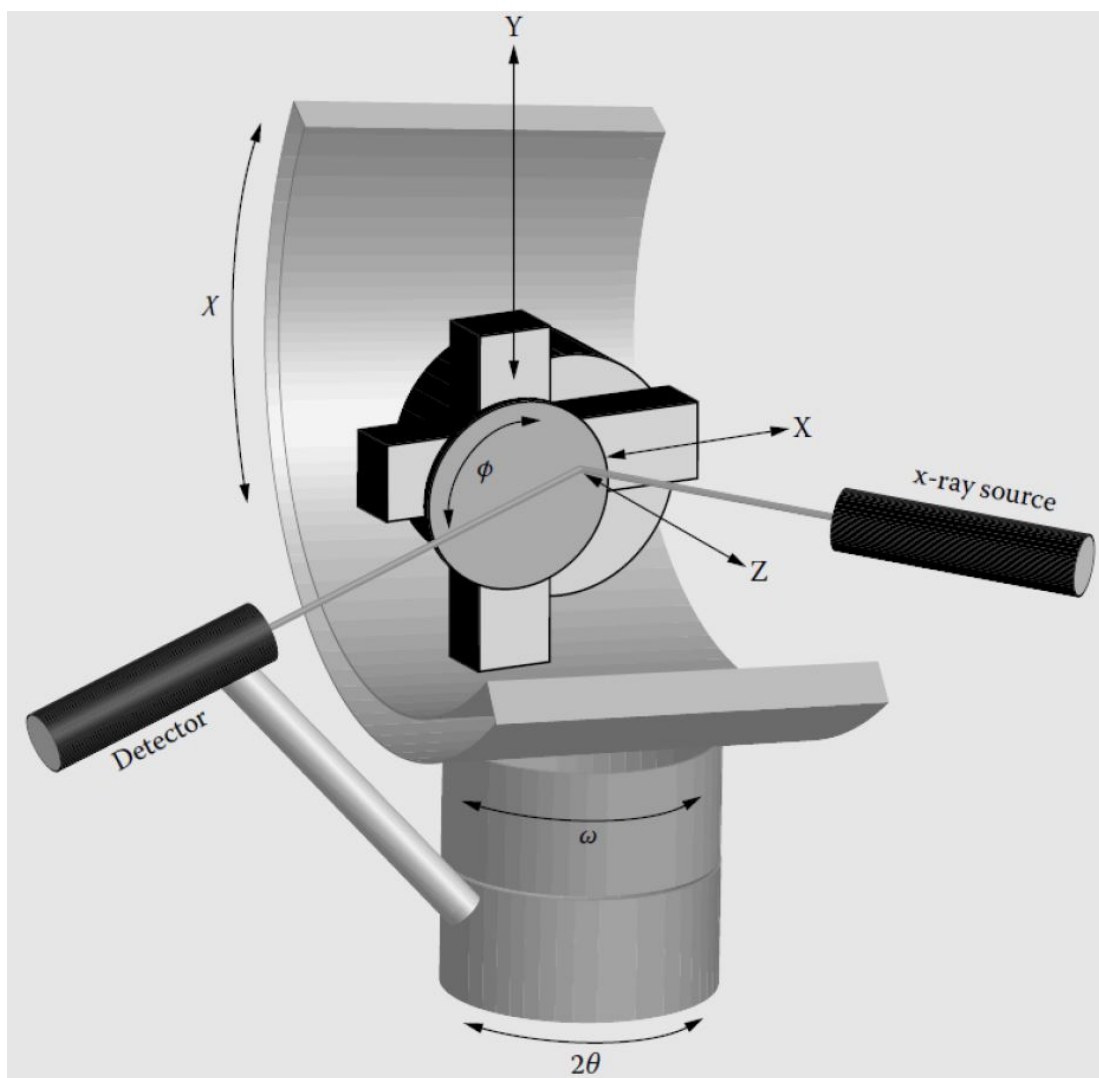
Figure 2.2: XRD apparatus showing the different scan (rotation) axis. Adapted from [98].

The PANalytical X'Pert 3 MRD system and the PANalytical X'Pert Epitaxy software were used to assess the samples in this project.

2.1.4 Photoluminescence spectroscopy

Photoluminescence (PL) is a process by which a semiconductor absorbs and re-emits photons, carrying information about the material's electronic structure. Valence band electrons are excited with a photon flux of energy higher than the bandgap (typically a laser). The excited electrons return to the lower energy state after emission of a phonon, photon or Auger electron. PL spectroscopy studies the re-emitted photons. In this case, the analysis of the emitted signal allows to estimate the bandgap of the material. The experimental setup used in this work is shown in Figure 2.3). The Fourier-transform infrared spectrometer is a Thermo Nicolet Nexus 870. It was used with a 780 nm pump laser-diode, a nitrogen-cooled $InSb$ detector and a KBr beam-splitter. Whenever the samples required low-temperature measurements, they were placed in cryostats under vacuum.
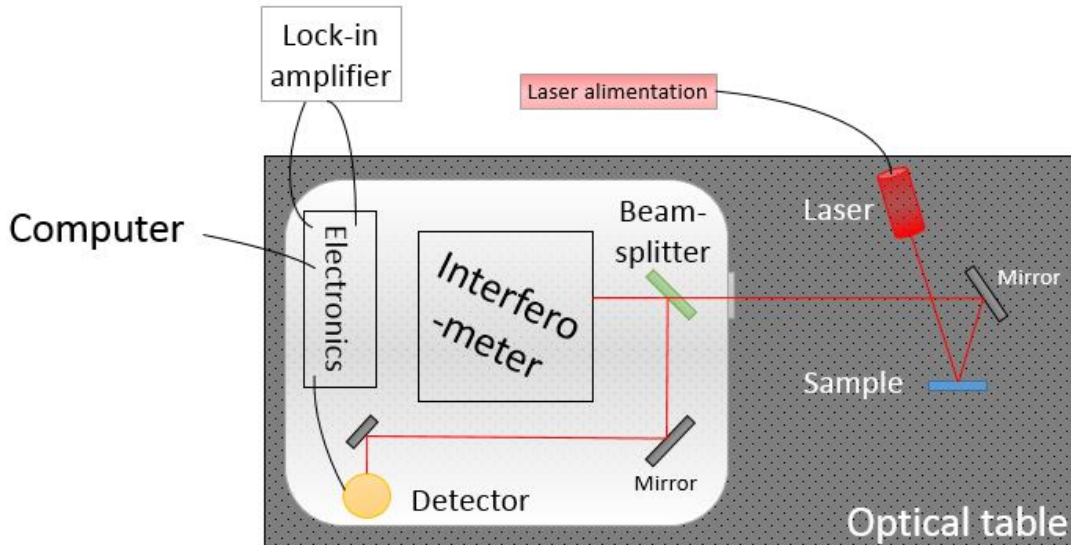
Figure 2.3: PL apparatus used in this project.

The extracted PL spectrum displays peaks corresponding to the different materials penetrated by the laser beam. For direct bandgaps, the material bandgap energy can be estimated from the position of the PL peak maximum with the equation: [100]

$$E_{gap} = E_{peak} - 1/2k_BT \tag{2.2}$$

where E_{gap} is the estimated bandgap energy, E_{peak} is the observed PL peak energy, k_B is the Boltzmann constant and T is the measurement temperature.

2.1.5 Other metrology tools

Other metrology tools used in this project include ion gauges, thermocouples, pyrometry, mass spectrometry for *in-situ* measurements. *ex-situ* measurements consisted of profilometry and optical, atomic force and electron (scanning and transmission) microscopy.

2.2 Clean room micro-fabrication

In this section, we present the photomasks developed for this project, in collaboration with III-V lab. Two mask configurations were used. The first one is the classic front-back configuration where one metallic contact is taken at the top of the solar cell and the other one is covering the whole back side of the wafer (non-illuminated side). The second one has both contacts taken on the front side of the cell: one at the top of the cell and one on parts of the samples where the material has been etched until reaching the substrate. This front-front configuration has been developed specifically for solar cells on Si, in order to avoid the high defect density at the III-V/Si interface. Further information can be found in Chapter 5.

The front-back and front-front configuration process flows are detailed below. Last, the clean room techniques used in this project are briefly introduced.

2.2.1 Grid and photomask set presentation

Samples were typically processed as quarters of 2-inch wafers containing each multiple 0.5 $cm \times$ 0.5 cm solar cells. All masks are designed for 2-inch wafers. They were elaborated on the basis of similar photomasks designed by G. Hamon and S. Soresi at III-V lab.

The contacts' fingers have a width of 10 μm and the contacts' busses have a width of 600 μm. Three different shading factors are studied:

- cells with a fingers spacing of 100 μm (shading factor of 10%)

- cells with a fingers spacing of 200 μm (shading factor of 5%)

- cells with a fingers spacing of 300 μm (shading factor of 3.3%)

The masks also contain quantum efficiency (QE) and transmission line measurement (TLM) cells. Two types of TLM patterns are used:

- big (diameter 400 μm) : patterns of 8, 16, 24, 32, 40, 48, 64, 80, 96, 112 μm

- small (diameter 200 μm) : patterns of 4, 8, 12, 16, 20, 24, 32, 40, 48, 56 μm

The various sets of masks used in this work are presented in the following. Detailed process flows are shown in the appendices.

Front-back configuration

The masks contain:

- 26 solar cells

- 2 (identical) QE measurement units

- 2 (identical) TLM measurement units

There are 3 mask levels: front contacts, mesas and anti-reflective coating (ARC). Figure 2.4 shows a quarter of each mask.

(a) Front contacts mask.   (b) Mesas mask.   (c) ARC opening mask.
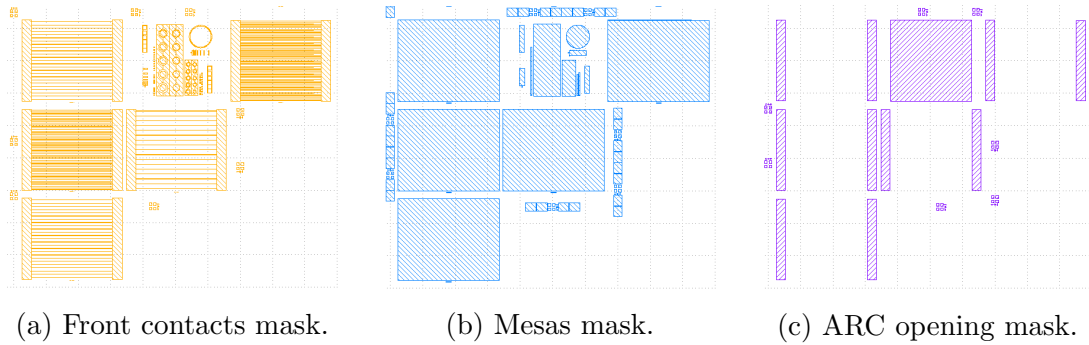
Figure 2.4: Set of masks used in this work for solar cells on $GaSb$ processing (quarter view).

Front-front configuration

The masks contain:

- 24 solar cells

- 2 (identical) QE measurement units

- 2 (identical) TLM measurement units

There are 3 mask levels: mesas, ARC and metallization. Figure 2.5 shows a quarter of each mask.

(a) Mesas mask.   (b) ARC opening mask.   (c) Metallization mask.
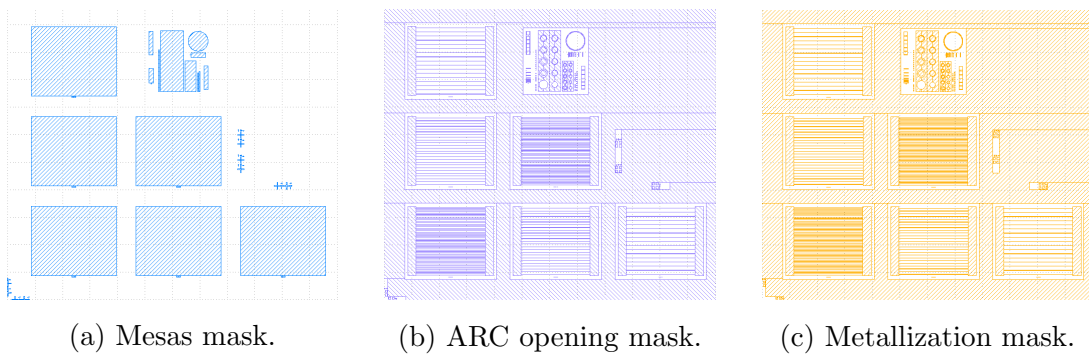
Figure 2.5: Set of masks used in this work for solar cells on Si processing (quarter view).

2.2.2   Used techniques

Standard clean room techniques were employed, that are detailed in this subsection.

Photolithography

Photolithography is the technique by which a geometric pattern is transferred from an optical mask to a thin film or substrate. Using UV light, it imprints the pattern from the mask to a light sensitive photoresist applied to the sample. This new resist mask allows the etching or material deposition according to the geometrical pattern onto the sample. Photolithography was employed at almost every fabrication step, following this procedure:

- The photolithographic mask was cleaned in 4 subsequent ultrasonic baths: 3 min in acetone, 3 min in ethanol, 3 min in isopropanol 3 min in deionized (DI) water. It was then blow dried with nitrogen.

- The sample's surface was cleaned under the solvent hood: it was dipped 90 s in acetone, 90 s in ethanol and 90 s in isopropanol. It was then blow dried with nitrogen.

- The sample was heated for a 5 min dehydration at $110°C$ under the photolithography hood.

- The resist was spin-coated at 4000 rotations per minute (rpm) for 30 s.

- The sample was soft-baked according to the photoresist specifications.

- The sample was aligned on the SUSS MicroTec MJB4 manual mask aligner and exposed to light for the exposure time corresponding to the used resist.

- When necessary, the sample underwent a post-exposure bake (negative photoresist).

- The sample was dipped in AZ 726 developer for the required amount of time and rinsed under DI water flow for 2 min before being blow dried with nitrogen.

- The sample was observed under optical microscope. In the case of resist bilayer, the length of the undercut was noted.

- The resist thickness was assessed by profilometer.

Reactive ion etching

Reactive ion etching (RIE) is the most employed etching technique in micro-electronics. It is a plasma etching technique implying both ion sputtering and chemical reactions. First, a plasma is generated with chemicals prone to react with the sample. These chemicals are transferred from the plasma to the surface of the sample on which they adsorb and react. The volatile byproduct of the reaction further desorbs from the surface and is evacuated by the pumping system of the reactor. In this project, the inductively coupled plasma (ICP) mode of the RIE was employed. This mode uses RF energy to create a high-density plasma of ionized atoms and reactive gas radicals, providing a greater tunability of the etching process (rate, profile). The system was also equipped with a laser interferometer enabling etching depth control. The machine used in this project was an OXFORD Plasmalab system 100. Prior to each dry etch, we used a cleaning plasma to get rid of potential contaminants in the reactor. Then, we conditioned the chamber with the dry etching recipe acting on a dummy Si wafer for a few minutes. Eventually, we installed the sample, whose back was coated with oil to ensure a good thermal conductivity, on a Si holder and loaded it into the vacuum chamber to undergo dry etching. The recipe used in this project involved a mixture of $BCl_3 : Cl_2 : Ar$ on a sample cooled at $10°C$. The etching rate for $GaSb$ was estimated to 370 nm/min.

Plasma enhanced chemical vapor deposition

Plasma-enhanced chemical vapor deposition (PECVD) is a thin film deposition technique involving chemical reactions between gas precursors and the substrate. It uses a plasma to activate the gas decomposition into radicals that are adsorbed on the surface. There, the chemical reaction takes place and the film forms. Eventually, the reaction byproducts desorb from the surface and are evacuated away from the sample. PECVD makes it possible

to use low deposition temperatures (below $300°C$) which are critical in many applications where high temperatures could damage the devices being fabricated. PECVD offers very low levels of impurities and deposition rates in the 10 and 100 $\mathring{A}/s$ range. The equipment used in this work is the CORIAL D 250. It served to deposit dielectric films of SiO_2 and $SiN_x : H$ at 200 and $280°C$. The composition of the $SiN_x : H$ approached Si_3N_4, however this exact stoichiometry has not been confirmed.

Metal deposition

Prior to metal deposition, the oxide was removed from the surface with a 30 s dip in hydrochloric acid (HCl) diluted in DI water ($20 : 5\ mL$), followed by a DI water rinse and nitrogen blow dry. In this work, two metal deposition techniques were employed:

Electron gun evaporation
Evaporation is a physical vapor deposition technique where the material to be deposited is evaporated from a crucible heated at high temperature. The source was heated by an electron beam, offering fast deposition rates (between 1 and 20 $\mathring{A}/s$) and low levels of impurities. Once heated, the source material is transported onto the sample through gas phase and condensed onto the surface. Evaporation uses low-energy atoms in high vacuum, leading to few impurities and a high directionality. This anisotropy makes it good for lift-off but the sample must be tilted and rotated for step coverage. The equipment used in this work is the UNIVEX 350 electron-beam evaporator.

Sputtering
Sputtering is another physical vapor deposition technique where the substrate and the source materials (targets) are placed on two parallel electrodes in a chamber filled with inert gas. High voltages are applied to the electrodes causing a plasma to form in between and energetic particles to impinge on the target and eject material from it onto the substrate. Sputtering uses higher-energy atoms (and ions) than evaporation and should thus lead to a better adhesion of the materials to the sample surface. Sputtering has a smaller directionality than evaporation and offers good step coverage and film uniformity. It does not require high vacuum levels. The deposition rates are in the 100 $\mathring{A}/s$ range for metals. The equipment used in this work is the UNIVEX 450 B.

41

2.2.3 Anti-reflective coating

The ARC layer is a thin dielectric layer deposited on top of the emitter aiming at trapping light inside the cell and suppressing light reflection by the surface. It is typically made of SiN or SiO_2. ARC is engineered so that the reflected rays at the air-ARC and at the ARC-emitter interfaces are out of phase, generating destructive interferences (*i.e.* no reflection). This involves a specific choice of refractive index and thickness for the layer:

• Since the reflectivity at an interface is given by $R = \frac{n_1-n_2}{n_1+n_2}^2$, where n_i is the refractive index of region i, the optimum refractive index for the ARC is given by [101]:

$$n_{ARC} = \sqrt{n_{air/glass}n_{cell}} \qquad (2.3)$$

where $n_{air/glass}$ is the refractive index of either air or glass depending on the type of PV device and n_{cell} is the refractive index of the material the topmost cell is made of.

• In order to obtain destructive interferences between the reflective rays, a special thickness is chosen:

$$t = \frac{\lambda_0}{4n_{ARC}} \qquad (2.4)$$

where λ_0 is the wavelength of incident light. For PV applications, λ_0 is often set to 0.6 μm since it corresponds to the peak intensity of the solar spectrum. Another popular option is a double-layered ARC ($ZnS + MgF_2$ or SiN). However, one has to be careful not to make these layers too thick and generate more optical losses than they should suppress. The possibility to add hydrogen to the SiN layer makes it a strong candidate for a good coating. On top of being an ARC, the layer will indeed passivate the dangling bonds at the interface with hydrogen.

In this project, we used OPAL 2 software to optimize the choice of ARC materials and thicknesses [102]. This software takes into account the variation of the refractive index

with the wavelength. It assumes ideal coatings and total reflection from the rear surface. More information can be found in the provided reference. OPAL 2 uses data libraries taken from the literature (such as the $n - k$ values found by Aspnes and Studna for $GaSb$ [103]) or allows the user to input its own experimental data. It estimated the following optimal ARC thicknesses for a SJ $GaSb$ cell:

- 123 nm for SiO_2

- 86 nm for Si_3N_4

- 94 nm for $SiN_x : H$

2.2.4 Metallic contacts

The metal-semiconductor interface forms a Schottky barrier, which thickness can be reduced by highly doping (favoring electrons tunneling). On the n side, the doping of $GaSb$ is limited to the $1E18\ cm^{-3}$ range [104] [105]. This relatively low doping level limits the contact quality. To overcome this issue, n-type $GaSb$ solar cells where the contact to the n side is made by full-wafer back-side deposition are generally favored. It is the case in this work. Annealing of the contact after metal deposition enables metal diffusion within the semiconductor, creating a highly-doped surface layer which reduces the Schottky barrier at the interface. However, annealing was not done in this work, in order to avoid damage to the heterostructures.

n-type contacts

Best contacts in the literature were obtained by Robinson *et al.* with $Pd/In/Pd/Pt/Au$ and a double anneal: first $1 - 2\ min$ at $125°C$ and then $10\ min$ at $350°C$ [106]. Claimed resistivity was $2.4 \times 10^{-6}\ \Omega\ cm^2$. Ikossi *et al.* also reached a resistivity of $1.4 \times 10^{-6}\ \Omega\ cm^2$ with $Pd/Ge/Pd/In/Pd$ (1 min anneal at $350°C$) and one of $3.8 \times 10^{-6}\ \Omega\ cm^2$ with $Pd/Ge/Pd$ (1 min anneal at $400°C$) [107]. Based on the availability of materials in the clean room, we have used Ti/Au 30/250 nm for this contact.

p-type contacts

For low-doping $GaSb$ ($1E17$ range), best contacts were obtained by Tadayon *et al.* with a Au contact of 25 nm annealed at 200°C for 1 min, reaching a resistivity of $1.4 - 7.8 \times 10^{-8}$ Ω cm^2 [108]. At higher doping levels ($1E20$ range), resistivities of 6.5×10^{-8} Ω cm^2 were obtained by Soldatenkov *et al.* with Pt/Ag contacts annealed at 160 and 185°C for 15 to 60 s [109]. Based on the availability of materials in the clean room, we have used $Pd/AuGeNi$ 5/200 nm for this contact when it was a back contact. When the top-top contact configuration was used, we deposited Ti/Au 30/250 nm for both contacts.

2.3 Device characterization

Solar cell performance is typically characterized both electrically and optically. On the first hand, the study of the current density - voltage (J-V) characteristic allows to determine the cell efficiency and estimate the parasitic resistances. On the other hand, the spectral response of the cell reflects on the exploitation of the incoming light by the cell and the corresponding losses. Both measurements are detailed in the following.

2.3.1 J-V curve

The experimental J-V setup is presented in Figure 2.6. In this work, solar cells were characterized at the University of Montpellier (France) using a Newport ORIEL Sol 3A solar simulator. The lamp was calibrated using a reference Si cell, and equipped with a filter to provide an AM1.5G illumination. A Keithley 2400 Source Meter was used to measure the electrical parameters of the cells. The cells were mounted on a Peltier element to maintain a temperature of 25°C upon illumination. $GaSb$-on-$GaSb$ solar cells were also characterized at the University of Lancaster (United Kingdom) with a LOT ORIEL LS0106 solar simulator.

The study of the intensity-voltage characteristic allows to extract a number of electrical metrics:
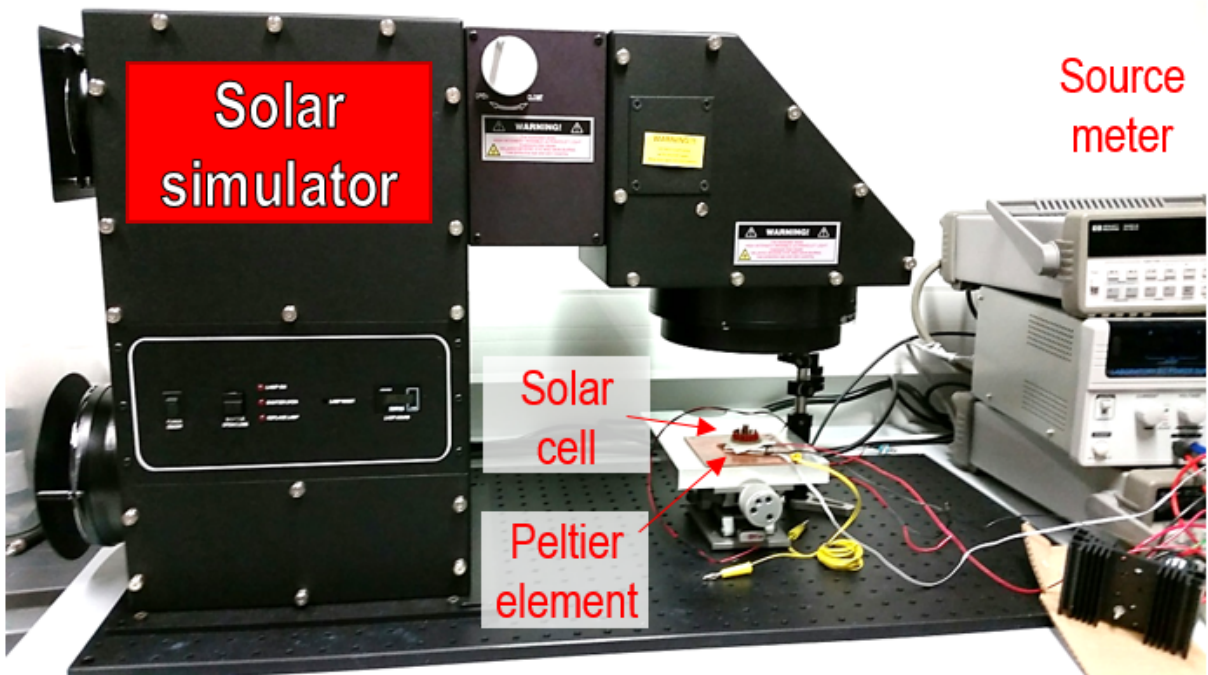
Figure 2.6: Electrical characterization setup at the University of Montpellier.

- The short-circuit current density J_{SC} is the current density through the solar cell when the voltage across the device is zero. It corresponds to the maximum current density which may be drawn from the solar cell. J_{SC} strongly depends on the generation rate and diffusion length of the carriers.

- The open-circuit voltage V_{OC} is the voltage across the device when the net current through the cell is zero. It corresponds to the amount of forward bias on the cell due to bias of the junction under illumination. V_{OC} strongly depends on the saturation current of the device, hence on the amount of recombination.

- The fill factor FF is defined as the ratio of the maximum output power to the product of I_{SC} and V_{OC} : $FF = \frac{V_{MP}I_{MP}}{V_{OC}I_{SC}}$. It is a good measure of the ideality of the solar cell.

- The cell's efficiency η is defined as the ratio of the total energy output over the total energy input. The standard P_{input} used is $1\ kW/m^2$. The efficiency is given by

$$\eta = \frac{V_{OC} \times I_{SC} \times FF}{P_{input}} = \frac{P_{max}}{P_{input}}$$

2.3.2 Diode models

Numerical fits to both the illuminated and dark J-V curves make it possible to estimate additional parameters. The single-diode equation provides a simplified description of the intensity-voltage characteristic of a solar cell:

$$J = J_0(\exp^{\frac{qV}{nk_BT}} - 1) \tag{2.5}$$

with J the net current density flowing through the diode, J_0 the dark saturation current density (leakage current density in the absence of light), n the ideality factor of the diode, V the voltage applied across the junction, q the absolute value of electron charge, k_B the Boltzmann constant and T the temperature. J_0 is a measure of the recombination in the device. It increases with T and decreases as the material quality decreases. n is another important parameter of the device as it indicates how close to an ideal diode it is.

In the single-diode equation model, this parameter is assumed to be constant. In reality, it depends on the voltage V. At high voltage, recombinations at the surfaces and in the bulk predominate and the ideality factor approaches 1. At low voltage, however, the cell operation is dominated by recombination at the junction and the ideality factor is close to 2. A double-diode model can therefore describe the device more accurately by adding a second diode of ideality factor 2, taking into account deviations from the ideal diode operation. The device then follows Equation 2.6 (solar cell in the dark):

$$J = J_{01}(\exp^{\frac{q(V-JR_s)}{k_BT}} - 1) + J_{02}(\exp^{\frac{q(V-JR_s)}{2k_BT}} - 1) + \frac{V - JR_s}{R_{sh}} \tag{2.6}$$

where R_s and R_{sh} are respectively the series and shunt resistances associated with the model.

The corresponding electrical model is shown in Figure 2.7.

In Chapter 3, we use the two-diode lumped model to characterize the solar cells. In Chapter 5, a more complex solver is used, involving as well fitting to the QE curve. This
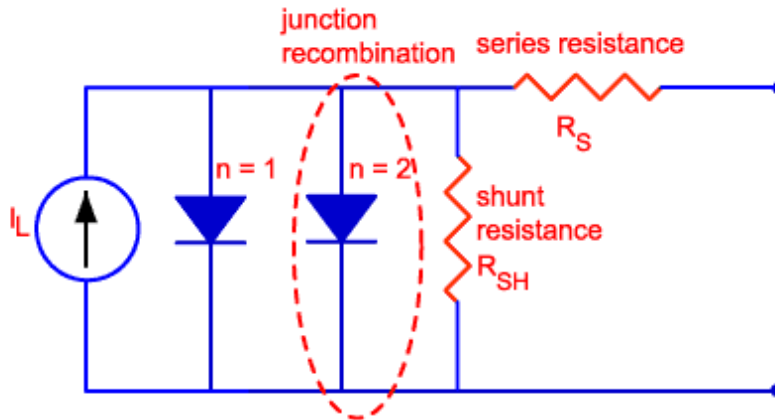
Figure 2.7: Circuit diagram of the double-diode model of the solar cell. Source: pveducation.org

solver was developped by Frédéric Martinez from the M@csee group at the University of Montpellier. Fits to the experimental curves presented in this work were realized by Stéphanie Parola from the same group.

2.3.3   Quantum efficiency

The QE is defined as the ratio of carriers collected by the cell to the total incident photons of a given energy. External and internal QE are both used in optical characterization. External quantum efficiency (EQE) includes the effects of reflection and transmission, whereas internal quantum efficiency (IQE) only takes into account light that reaches the inside of the cell. The IQE can therefore be viewed as the collection probability due to the generation profile of a single wavelength, integrated over the device thickness and normalized to the incident number of photons. It can be calculated from the EQE and transmission/reflectance spectrum of the cell.

Similar to the QE, the spectral response (SR) is also used to characterize a solar cell. It is the ratio of photogenerated current to the incident power for a considered wavelength. The two parameters are related by:

$$SR = \frac{q\lambda}{hc}QE = \frac{QE}{\lambda(nm)} \times 1239.8 \tag{2.7}$$

The spectral response of the cells was acquired at the University of Montpellier with a setup made of a Xenon lamp and an Acton ARC AM-505F spectrometer. The equipment was calibrated with a reference Si photodiode (BN-DSR-100F, Gigahertz-Optik) and a Ge photodiode (FDG03-CAL, Thorlabs) for the infrared wavelengths. The experimental setup is shown in Figure 2.8.
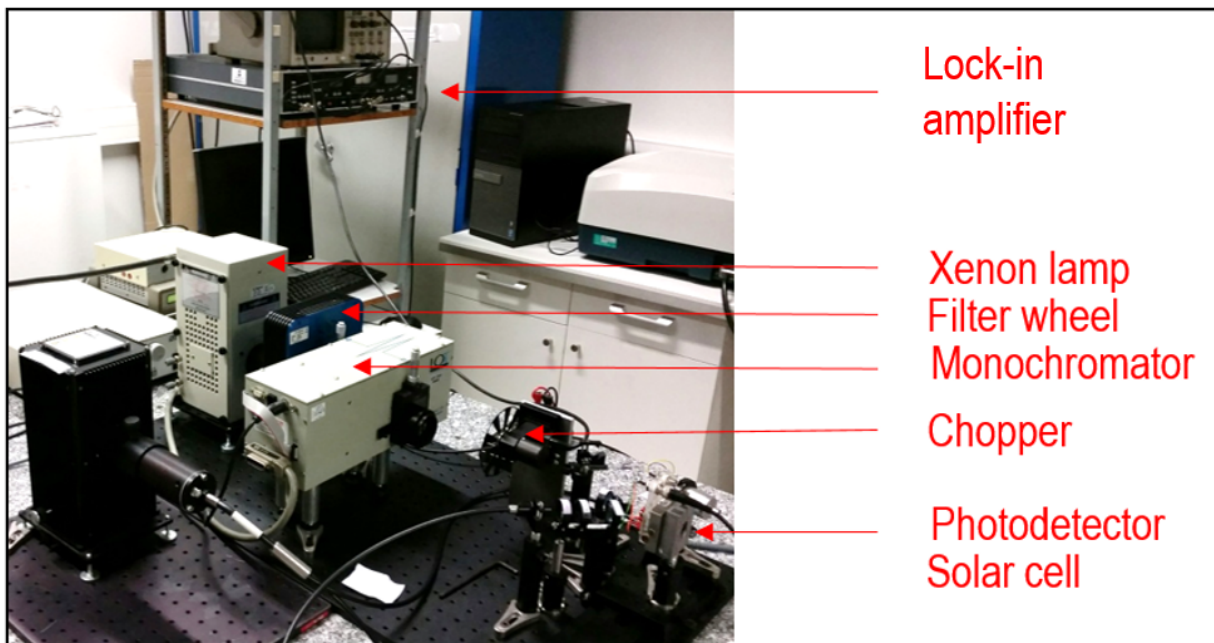
Figure 2.8: Optical characterization setup at the University of Montpellier.

2.4 Summary

In this chapter, we present the growth, processing, and characterization techniques used in this project. For each of them, a rapid description is provided. Detailed process flows can be found in the appendices.

Chapter 3

GaSb-on-GaSb solar cells

The first building block of this project is the elaboration of a state-of-the-art stand-alone *GaSb* solar cell. In this chapter, we first review the literature and investigate the cell design with simulations. Then, we detail the fabrication process. Last, we present the electrical and spectral characterization of the devices.

3.1 GaSb-based solar cells

3.1.1 Literature review

This review focuses on *GaSb*-based solar cells for PV applications only. Such cells have also been extensively studied for thermophotovoltaic applications, which fall beyond the scope of this work. *GaSb* solar cells were investigated as early as 1989 in the context of cascaded tandem cells. *GaSb* "booster" cells, as referred to in [110], were expected to enhance *GaAs* cell performance by 6%. Using a mechanical stack of the two cells, the Boeing High Technology Center achieved a record 32.6% efficiency under 100 suns (AM1.5D). The bottom *GaSb* subcell efficiency was thus 9.3% under AM1.5D at 84 suns. About twenty years later, Andreev *et al.* enriched this *GaAs/GaSb* stack with an upper *GaInP* [111] or *AlGaAs* [112] cell. The module efficiency attained 24.7% under concentration, falling

short of the projected 36%. The discrepancy between theory and experiment can largely be attributed to optical losses, inherent to the spectrum splitting technique used. Mechanical stacks involving $GaInP$ and $GaInAs$ with $GaSb$ have also been investigated. Bett *et al.* were able to attain 33.5% efficiency at 308 suns [113] and Shvarts *et al.* 35% at 50 suns [114]. All of the aforementioned modules used four-or-more- terminal configurations. Although these modules are less sensitive to chromatic aberrations and variations in the solar spectrum, they are also heavier and more cumbersome than two-terminal devices. Other epitaxial approaches, such as inverted metamorphic cells involving thick buffer layers, have also been investigated. Nelson *et al.* recently made progress toward the monolithic integration of the $GaInP/GaAs/GaSb$ triple-junction cell [65]. The homoepitaxial $GaSb$ cell had a 1-sun efficiency of 5.5% (AM1.5G) with an open-circuit voltage (V_{OC}) of 282 mV, a short-circuit current density (J_{SC}) of 33.9 mA/cm^2, and a fill factor (FF) of 59%. Although encouraging, attempts to integrate the cell on a $GaAs$ substrate significantly degraded the efficiency to 1.0%. Similar results were obtained by Mansoori *et al.* with $GaSb$ solar cells grown on $GaAs$ substrates using $AlSb$ dislocation filters [115]. The homoepitaxial $GaSb$ cell had V_{OC} of 230 mV, J_{SC} of 33.5 mA/cm^2, and FF of 50%. Once more, the integration onto $GaAs$ significantly degraded the performance of the cell with V_{OC} of 145 mV, J_{SC} of 21.7 mA/cm^2, and FF of 29%. Last, a lattice-matched double-junction $GaSb/InGaAsSb$ cell was also studied by [15] to be stacked with a $GaAs$-based triple-junction. Under a 1.2 concentration ratio, the $GaSb$ solar cell exhibited 5.3% efficiency, V_{OC} of 315 mV, and FF of 58%. The low fill factors reported in the aforementioned pieces of work probably result from elevated parasitic resistances (due to the low quality of contacts, passivation and unoptimized grid designs). There is therefore room for improvement in these directions.

3.1.2   GaSb stand-alone cell simulation

We propose the $GaSb$ cell structure presented in Figure 3.1. Preliminary simulations were made with SCAPS software to provide an estimate of the performance [116]. It is worth noting that this software assumes pristine crystal quality, independently of the doping level. In reality, elevated doping levels tend to introduce defects into the crystal. The p-type residual doping ($2-5 \times 10^{16} \ cm^{-3}$) is also ignored in the simulation. We used for

the simulation a high series resistance of 2.0 Ω cm^2, in accordance with our measurements on contacts to $GaSb$ samples. This consistently limits the performance of the cell.
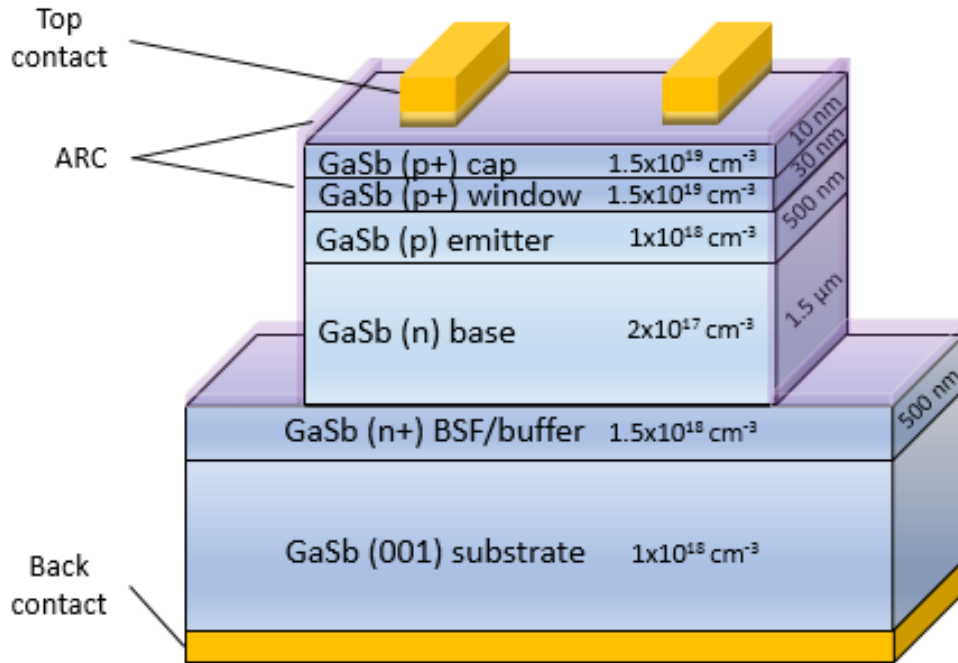
Figure 3.1: Schematic structure of the GaSb-on-GaSb solar cell.

For the structure shown in Figure 3.1, we compute 7.78% efficiency, with V_{OC} of 345 mV, J_{SC} of 41 mA/cm^2, and FF of 55.3% (Figure 3.2). According to the software, changes to the base and emitter thicknesses would only enhance the cell efficiency by a few tenths of a percent. Also, we did not at first consider the use of window layers of higher bandgap. Such layers indeed include high Al contents, making them particularly vulnerable to oxidation. We wanted to ensure good control of the processing steps before incorporating sensitive materials into the structure. Window layers in the proposed design are therefore only made of highly doped $GaSb$.
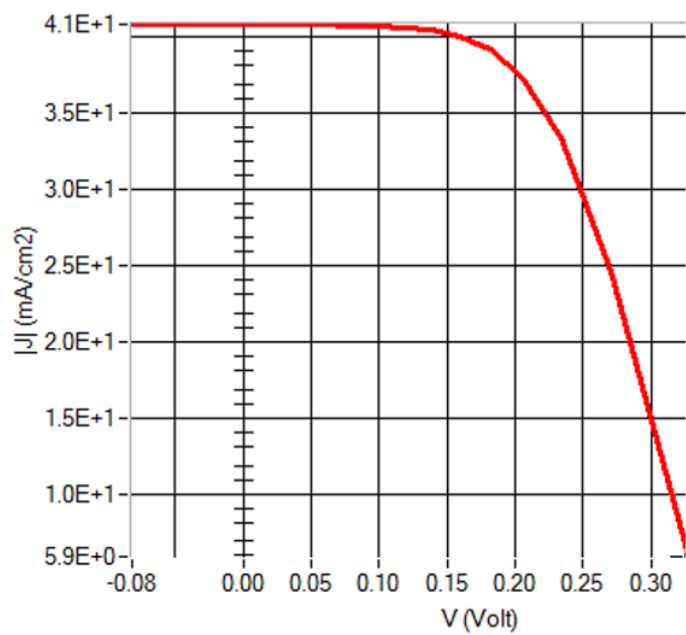
Voc (V)	Jsc (mA/cm2)	FF (%)	eta (%)
0.3445	40.826805	55.29	7.78

Figure 3.2: Simulated J-V curve for a *GaSb*-on-*GaSb* solar cell in SCAPS.

The simulated theoretical performance was higher than what has been observed in the literature thus far [15] [65] [115]. Given that the cell is homoepitaxial and judging by the reduced reported V_{OC} and J_{SC}, improvements to the passivation (assumed ideal in the simulation) to limit surface recombination seem crucial to bridge the gap with theory.

3.2 Solar cell fabrication

3.2.1 Solar cell epitaxy

Lattice-matched $GaSb$ solar cells were grown by MBE in the Varian GENII reactor. Upon loading into the growth reactor, 2-inch epi-ready n-type (001) $GaSb : Te$ substrates were deoxidized under Sb flux at 550 $°C$. After 20 minutes of deoxidation, the temperature was lowered to 500 $°C$ to grow a 200-nm $GaSb$ buffer layer. The solar cell growth was then initiated at the same temperature. The $GaSb$ growth rate, set by the Ga growth rate, was 1 ML/s. The V/III growth rate ratio was kept close to 2. Be and Te were used for p- and n-type doping, respectively. The solar cell structure is shown in Figure 3.1. It is made of a 500-nm back surface field (BSF), a 1500-nm base, a 500-nm emitter and a 30-nm window layer. The structure was eventually capped with a p-doped 10-nm contact layer, which also provided protection to the active region during the subsequent processing steps.

The surface was monitored during growth with RHEED. As expected for homoepitaxial growth, streaky patterns were observed throughout the growth, indicative of a smooth surface. The crystalline quality was subsequently confirmed with XRD, with the ω-2θ scan displaying only a narrow peak. The FWHM was evaluated at 38 $arcsec$, very close to the usual 30 $arcsec$ of a substrate peak.

3.2.2 Solar cell processing

After growth, 0.5-cm × 0.5-cm SJ $GaSb$ solar cells were fabricated in the class 10000 clean room of the University of Montpellier. The procedure comprised four steps represented in Figure 3.3. First, Ti/Au 30/250 nm was deposited by electron beam evaporation for the front contacts. Then, 2-μm deep trenches were opened by ICP RIE to isolate the cells from each other. A 214-nm thick $SiN_x : H$ passivation/ARC layer was later deposited on the top and sides of the active surface. On some samples, a 291-nm thick SiO_2 layer was used instead. The ARC was subsequently etched on top of the bus bars to open access to the metallic contact for electrical wiring. PECVD and ICP RIE were employed for this step. Last, $Pd/AuGeNi$ 5/200-nm layers were deposited by sputtering on the whole

back surface. At the end of processing, the samples were cleaved into individual cells and mounted on $TO-8$ holders with silver paint. The solar cell bus bars and back contacts were connected to the $TO-8$ pins by micro-welding.

CONTROL SOLAR CELL PROCESS FLOW
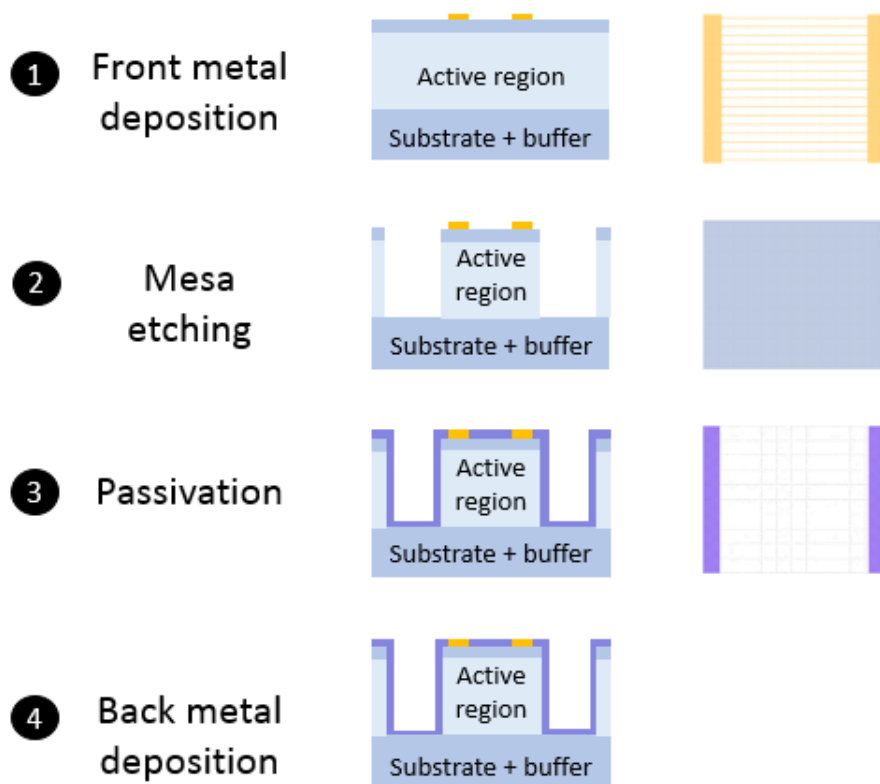
Figure 3.3: Schematic illustration of the processing steps for the fabrication of the $GaSb$-on-$GaSb$ solar cell. For each step, a picture of the corresponding photolithography mask is displayed (right).

The resulting cell is shown in Figure 3.4.
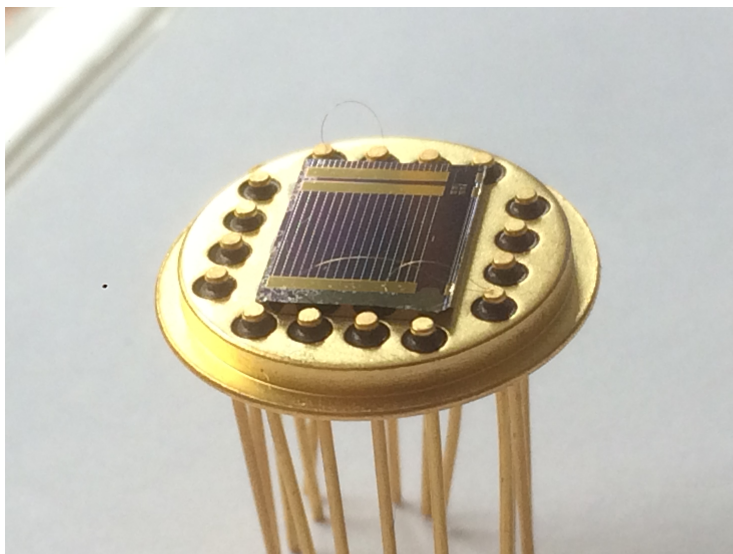
Figure 3.4: Fabricated $GaSb$-on-$GaSb$ solar cell.

3.3 Device characterization

3.3.1 J-V parameters

Initial results

In order to produce a state-of-the-art $GaSb$ stand-alone cell, we conducted an extensive study of the device to ensure the stability of the cells over time and the impact of the passivation/ARC. All of the cells mentioned below originated from the same epitaxial sample and were processed at the same time. Three types of cells were fabricated: SC012 cells with a $SiN_x : H$ passivation, SC015 cells with a SiO_2 passivation, and SC013 cells with no passivation. Table 3.1 shows a comparison of the results obtained at both measurement sites. The best control solar cell demonstrated a 1-sun efficiency (η) of 5.90%, indicating reasonably high material quality [65]. The cell had V_{OC} of 280 mV, J_{SC} of 36 mA/cm^2, and FF of 58.9%. The same cell exhibited similar characteristics when measured in Lancaster, four months later, with an efficiency of 5.84%, V_{OC} of 286 mV, J_{SC} of 37 mA/cm^2, and FF of 55.1%. The shading factor of this particular cell was 5%. The repeated measurements

56

were consistent for all types of cells, demonstrating the stability of the devices and the reliability of the measurement setups. While this was expected for the passivated cells, it is interesting to note that there was not much degradation between the parameters measured in July and November for the unpassivated SC013 cell. This indicates that any oxidation process occurring at the surface of the cell is almost complete from the very beginning and does not worsen significantly over time. Still, we observed that the passivation layer reduced the dispersion of the J-V curves (current density-voltage, observed over 8 samples), making cell characteristics more reproducible.

Influence of passivation

Results concerning the influence of the passivation layer are shown in Table 3.2, corresponding to cells with a shading factor of 5%. The associated J-V curves, shown in Figure 3.5, provide additional data concerning the impact of passivation.

It appears that the $SiNx : H$ passivation/ARC yields higher efficiencies. The dark J-V data were fitted to the two-diode lumped model for an abrupt pn junction [117]. Ideality-of-one dark current J_{01}, ideality-of-two dark current J_{02}, and an estimate of the shunt resistance R_{sh} were extracted. The passivated cells exhibited higher shunt resistance (R_{sh} of 1.7×10^3 Ω cm^2 and 1.3×10^3 Ω cm^2 for SC012a and SC015b, respectively, vs 5.3×10^2 Ω cm^2 for SC013b), indicating reduced leakage currents on the surface and edges of the mesas. Particularly, in forward bias, the generation-recombination current was lower on the passivated samples (J_{02} of 1.3×10^{-5} A/cm^2 and 1.6×10^{-5} A/cm^2 for SC012a and SC015b, respectively) than on the unpassivated one (J_{02} of 3.10×10^{-5} A/cm^2 for SC013b), indicating a longer carrier lifetime. The two types of passivation achieved very similar results and could not really be distinguished. The added benefit of the $SiN_x : H$ on the 1-sun curve(s) can therefore be attributed to its anti-reflective action. As dark J-V curves were similar for SC012a and SC015b in the forward regime, the better performance of the SC012a cell under illumination was due only to the increased generated photocurrent. This was expected from the better transmission pattern of the 214 nm $SiN_x : H$ coating (shape similar to that of the 291-nm SiO_2 coating, with higher intensity), as indicated by in-house ellipsometry measurements.

57

Table 3.1: Correlation between the distinct sites measurements. 1-sun efficiency (η), fill factor (FF), short-circuit current density (J_{SC}) and open-circuit voltage (V_{OC}) measured for control cells in Montpellier (July 2017) and Lancaster (November 2017).

Cell	Measurement site	η (%)	FF	J_{SC} (mA/cm^2)	V_{OC} (mV)
SC012a	Montpellier	5.90	0.59	36	280
	Lancaster	5.84	0.55	37	286
SC015a	Montpellier	4.86	0.51	34	280
	Lancaster	4.75	0.48	35	280
SC013a	Montpellier	4.21	0.54	28	280
	Lancaster	4.31	0.52	31	270

Table 3.2: J-V parameters measured for 5% shading $GaSb$-on-$GaSb$ solar cells. 1-sun efficiency (η), fill factor (FF), short-circuit current density (J_{SC}), and open-circuit voltage (V_{OC}) measured for all types of cells: with $SiN_x : H$ passivation (SC012), with SiO_2 passivation (SC015), and with no passivation (SC013). These measurements were made at the University of Lancaster.

Cell type	η (%)	FF	J_{SC} (mA/cm^2)	V_{OC} (mV)
SC012a ($SiN_x : H$)	5.84	0.55	37	286
SC015b (SiO_2)	4.47	0.47	34	280
SC013b ($\oslash$)	4.40	0.52	32	270
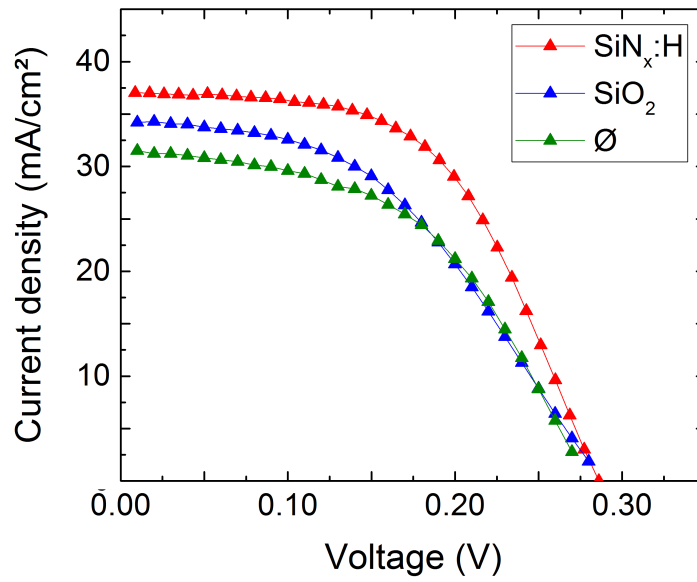
(a)
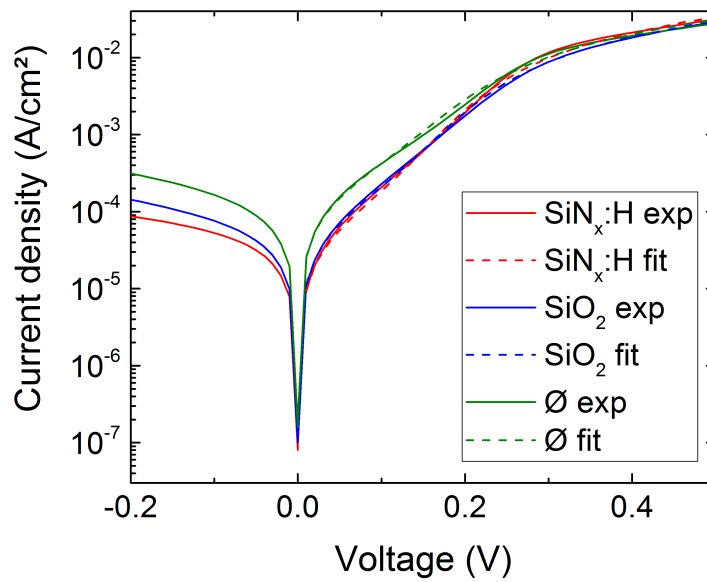
(b)

Figure 3.5: Measured (a) 1-sun and (b) dark J-V curves for all types of control solar cells: with $SiN_x : H$ passivation (red), with SiO_2 passivation (blue), and with no passivation (green).

Influence of the shading factor

In terms of shading factor, no clear tendency could be discerned from the results. The compromise between the higher J_{SC} (lower shading factor) and the lower V_{OC} (lower shading factor) was too fine and the pool of samples too small to provide any conclusion. The maximum relative change in efficiency with shading factor was around 10%, corresponding to a 0.4% absolute change. Detailed results are listed in Table 3.3. We expect a more significant impact on measurements under concentration, but these measurements are out of the scope of this exploratory work.

Table 3.3: J-V parameters measured for $GaSb$-on-$GaSb$ solar cells. 1-sun efficiency (η), fill factor (FF), short-circuit current density (J_{SC}) and open-circuit voltage (V_{OC}), depending on the shading factor, measured for all types of cells: with $SiN_x : H$ passivation (SC012), with SiO_2 passivation (SC015), and with no passivation (SC013). These measurements were made at the University of Lancaster.

$*$The cell was damaged upon cleaving.

Cell type	Shading factor (%)	η (%)	FF	J_{SC} (mA/cm^2)	V_{OC} (mV)
	3.3	$NA*$	$NA*$	$NA*$	$NA*$
SC012 ($SiN_x : H$)	5	5.84	0.55	37	286
	10	5.24	0.54	33	290
	3.3	4.75	0.48	35	280
SC015 (SiO_2)	5	4.47	0.47	34	280
	10	4.32	0.47	32	290
	3.3	3.95	0.45	33	270
SC013 ($\oslash$)	5	4.40	0.52	32	270
	10	4.31	0.52	31	270

3.3.2 Quantum efficiency

Figure 3.6 shows the experimental EQE curve of the highest efficiency $GaSb$-on-$GaSb$ cell. The EQE values exceeded 70% over the $1150 - 1540$-nm wavelength range. The resulting

maximum IQE, shown in Figure 3.6, was computed to be 81.6% at 1150 nm, indicating an efficient carrier collection in the base. Both EQE and IQE values reflect the device suitable material quality. However, the values at short wavelengths reveal important losses, pointing to poor carrier collection on the front surface. High bandgap materials such as $AlGaAsSb$ or $AlInAsSb$ alloys, lattice-matched to $GaSb$, could provide a well-suited window layer. Optimization of the emitter thickness could also improve high-energy collection, as we used a thick emitter compared with the standard values for PV applications ([15] [65]). The difference between the EQE and IQE curves further shows that the ARC layer thickness can be improved.
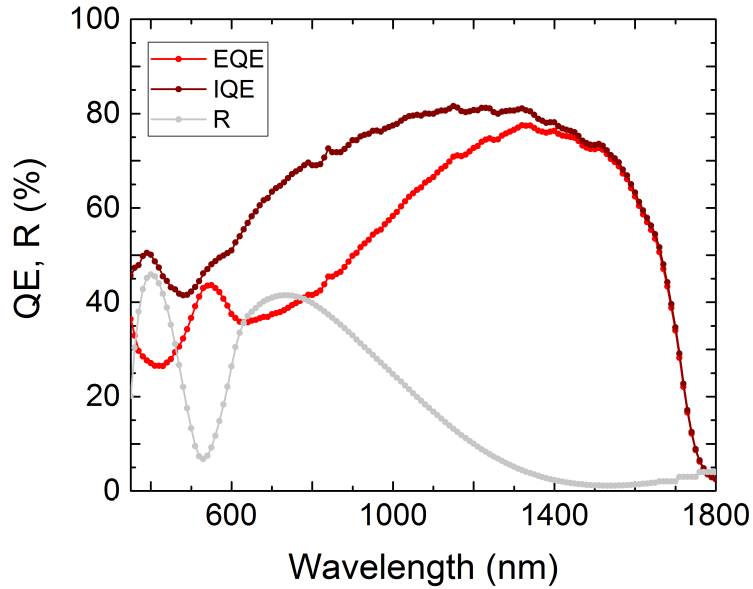
Figure 3.6: Measured EQE for the highest efficiency $GaSb$-on-$GaSb$ solar cell (bright red). The reflectivity (R) is shown in gray. The resulting IQE is shown in dark red.

3.4 Summary and proposition of an improved structure

In this chapter, we present our results on the development of a state-of-the-art $GaSb$ stand-alone solar cell. Efficiencies close to the best reported in the literature [15] [65] [115] were achieved and confirmed through measurements at two sites. Fitting the curves to the two-diode lumped model enabled us to highlight the benefits of $SiN_x : H$ passivation and extract resistance values that will serve as a comparison baseline in the following chapters. The cell performance, however, is still below theoretical expectations, as shown in Table 3.4.

Table 3.4: Performance of experimental ([15] [65] [115] and this work) and theoretical (SCAPS simulations) $GaSb$-on-$GaSb$ solar cells. All reported parameters are for the AM1.5G spectrum, except those of [15].

Cell	η (%)	FF	J_{SC} (mA/cm^2)	V_{OC} (mV)
[15] (1.2 suns)	5.3	0.58	not specified	315
[65]	5.5	0.59	34	282
[115]	3.9	0.50	34	230
This work	5.9	0.59	36	280
Initial design simulation	7.8	0.55	41	345
Improved design simulation	9.3	0.60	39	395

Given that the homoepitaxial material was of pristine quality, the discrepancy between theory and experiment seems to indicate that passivation needs to be improved to decrease surface recombination (and increase the V_{OC}). Small changes to the cap layer thickness also had an impact on the cell efficiency in the simulations. The optimal cap thickness remains to be found that can withstand all fabrication steps without absorbing too much of the incoming photon flux. The analysis of the spectral response of our cell indicated further improvement pathways, such as a change in window layer and the optimization of the ARC thickness. Preliminary simulations in SCAPS showed that using 1 eV $AlGaAsSb$ window layers would achieve 8.81% efficiency (compared with 7.78% for the previous simulation),

with V_{OC} of 393 mV, J_{SC} of 37 mA/cm^2, and FF of 60.7%. Further change in the ARC could achieve 9.30% efficiency with V_{OC} of 395 mV, J_{SC} of 39 mA/cm^2, and FF of 60.0% (Figure 3.8). Further improvement to the FF could be achieved by a detailed contact study, which is out of scope for this work. At the time of writing this manuscript, the improved cell displayed in Figure 3.7 was being fabricated and tested.
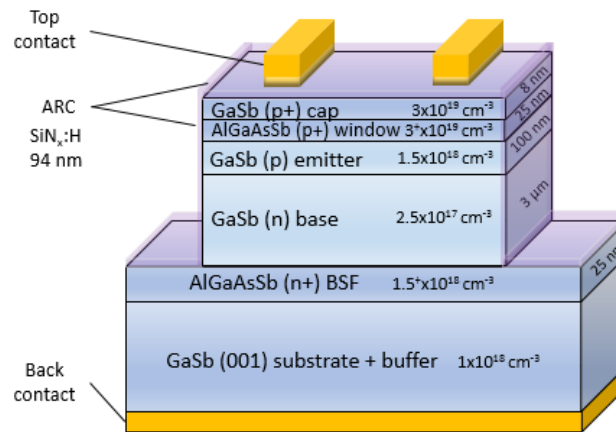
Figure 3.7: Schematic structure of the improved $GaSb$-on-$GaSb$ solar cell.
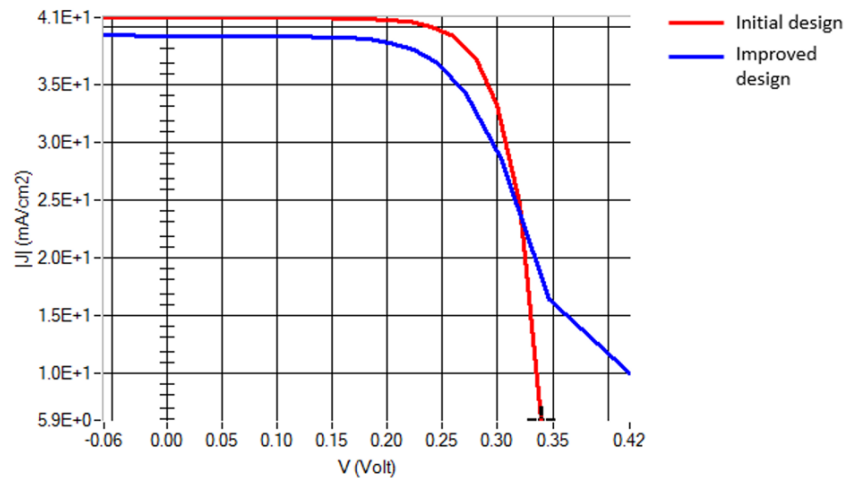
Figure 3.8: Simulated J-V curve for the improved $GaSb$-on-$GaSb$ solar cell in SCAPS.

Chapter 4

III-Sb multi-junction cells

The second building block of this project is the investigation of high-efficiency lattice-matched MJ structures on $GaSb$. First, we investigate a tandem cell design and identify the materials needed for this structure. We then present our epitaxial study of the $AlInAsSb$ alloy, which is essential to this project. Last, we detail our attempt (processing and characterization) at a $GaSb$-based tandem cell and conclude on the potential of III-Sb alloys for high-efficiency MJ cells.

4.1   Structure design

In this section, we present the initial steps of the conception of a III-Sb MJ solar cell: estimation of the required bandgaps, selection of adequate materials and structure of the TJs. We focus here on a tandem cell design as a proof of concept of high-efficiency III-Sb solar cells, which could later evolve into a three- or four-junction cell.

4.1.1 GaSb-based quaternary alloys and required bandgaps

Preliminary calculations

We performed a preliminary analysis of a *GaSb*-based tandem solar cell design in order to identify the required bandgap range. Given a tandem cell with a top cell E_g^{top} bandgap and a bottom cell E_g^{bottom} bandgap, the photocurrent density of each subcell is given by:

$$J_{ph}^{bottom} = \int_{E_g^{bottom}}^{E_g^{top}} q\Phi dE \tag{4.1}$$

$$J_{ph}^{top} = \int_{E_g^{top}}^{E_g^{\infty}} q\Phi dE \tag{4.2}$$

where q is the electron charge and Φ the incident spectral photon flux.

The photocurrent density of the tandem cell is given by the minimum of these two values (current-matching condition for series-connected cells):

$$J_{ph} = min(J_{ph}^{bottom}, J_{ph}^{top}) \tag{4.3}$$

For each subcell, the open-circuit voltage V_{OC} is computed from [118]:

$$V_{OC}^{subcell} = \frac{E_g^{subcell}}{q} - \frac{kT}{q} \times \ln\left(\frac{qwBN_CN_V}{J_{ph}^{subcell}}\right) \tag{4.4}$$

with w the thickness of the solar cell base, B the radiative recombination coefficient, N_C the effective density of states in the conduction band, and N_V the effective density of states in the valence band.

The total V_{OC} is the summation of the V_{OC} of the subcells:

$$V_{OC} = V_{OC}^{bottom} + V_{OC}^{top} \tag{4.5}$$

The power per unit area can be estimated by:

$$P_{tandem} = J_{ph} \times V_{OC} \times FF \tag{4.6}$$

For simulation purposes, a realistic FF of 85% is used.

The efficiency η of the cell is then given by:

$$\eta = \frac{P_{tandem}}{P_{sun}} \tag{4.7}$$

where P_{sun} is the incident solar power.

Setting the bottom cell's bandgap to that of $GaSb$, the optimal top cell bandgap appears to be 1.45 eV. This bandgap, combined with the parameters listed in Table 4.1, should allow the tandem cell to reach a 1-sun efficiency of 38% and a 1000-sun efficiency of 47%.

Table 4.1: Parameters used in the simulation of the $GaSb$-based tandem cell under 1 sun. The base of both subcells is assumed to be 1-μm thick.

Parameter	Bottom cell	Top cell
E_g	0.73 eV	1.45 eV
J_{ph}	27.2 $mA\ cm^{-2}$	26.9 $mA\ cm^{-2}$
B	$8.5 \times 10^{-11}\ cm^3\ s^{-1}$	$7.2 \times 10^{-10}\ cm^3\ s^{-1}$
N_C	$2.1 \times 10^{17}\ cm^{-3}$	$4.5 \times 10^{17}\ cm^{-3}$
N_V	$1.8 \times 10^{19}\ cm^{-3}$	$9.5 \times 10^{18}\ cm^{-3}$
V_{OC}	422 mV	1090 mV

This preliminary calculation provides good insight into the bandgap we should target for the top subcell. We thus suggest the design presented in Figure 4.1 for the tandem cell.
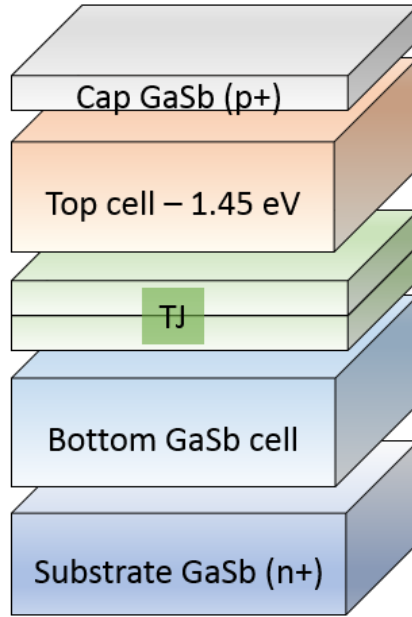
Figure 4.1: Structure proposed for a III-Sb tandem cell based on preliminary calculations. The III-Sb top cell should target a bandgap of 1.45 eV.

Choice of the quaternary alloy

As mentioned in Chapter 1, quaternary alloys offer numerous bandgap engineering opportunities. The (III,III-V,V) alloys, in particular, offer the independent tunability of the bandgap energy and the lattice parameter by the selection of an appropriate combination of III and V elements. In the case of lattice matching to $GaSb$, $AlGaAsSb$, $GaInAsSb$, and $AlInAsSb$, all enable an extended range of bandgaps. $AlGaAsSb$ and $GaInAsSb$, however, can only access bandgaps respectively higher or lower than that of $GaSb$. $AlInAsSb$ is the only alloy that provides access to both ranges while staying lattice-matched to $GaSb$, which makes it an interesting candidate for optimized MJ designs. Moreover, it seems that this alloy presents direct bandgap energies higher than those of $AlGaAsSb$ [61].

Early theoretical models of the influence of $Al_xIn_{1-x}As_ySb_{1-y}$ [1] composition on the bandgap and lattice parameter were made in the 80s by Glisson *et al.* and are shown

---

[1]In the following, $Al_xIn_{1-x}As_ySb_{1-y}$ and $AlInAsSb$ can be used interchangeably.

in Figure 4.2 [119]. The calculations were based on rare available experimental data and interpolation from binary and ternary compound bandgaps and lattice parameters. The results were computed according to Moon's procedure with known bowing parameters and extrapolations from experimental data for the others [120]. These estimations were re-evaluated by Adachi in 2009 [61]. The author used an interpolation matrix to compute the band parameters of $AlInAsSb$ from the known constituent ternary and binary compound parameters. He calculated the band diagrams of $AlInAsSb$, $AlGaAsSb$ and $GaInAsSb$ lattice-matched to $GaSb$ shown in Figure 4.3.
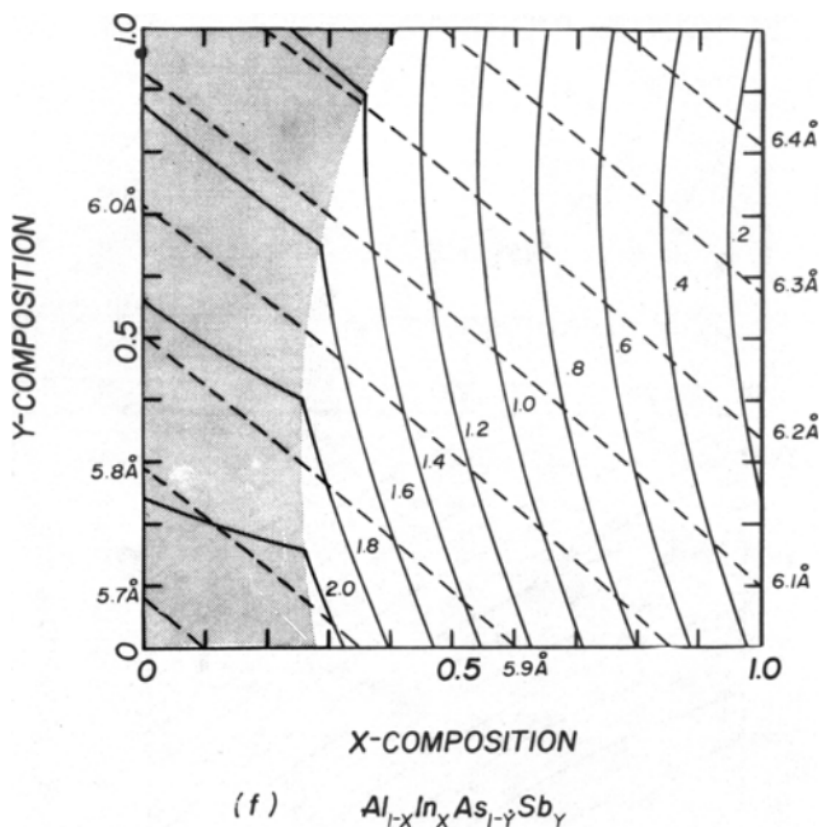
Figure 4.2: Bandgap energies (plain curves) and lattice parameters (dashed lines) of $Al_xIn_{1-x}As_ySb_{1-y}$ depending on the composition of III and V elements. Adapted from [119].
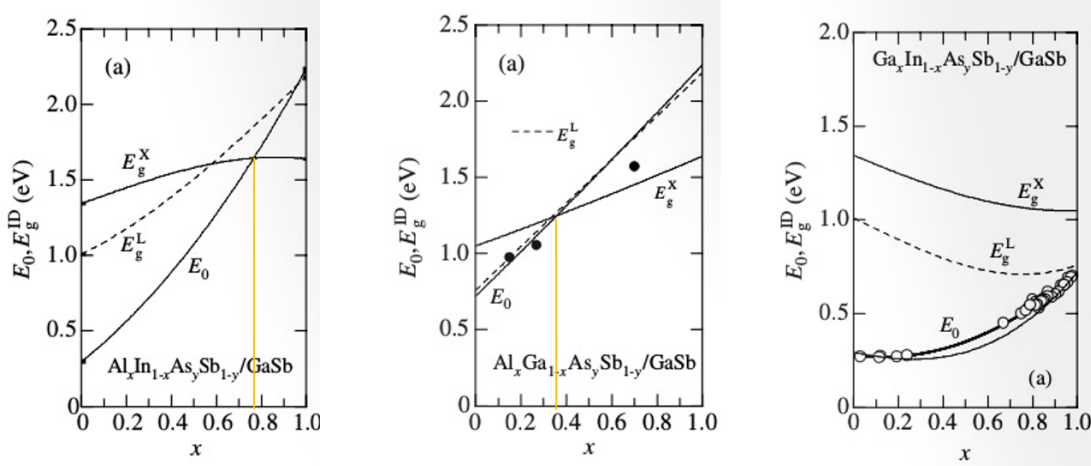
Figure 4.3: Energies of the lowest direct E_0 and indirect gaps E_g^{ID} vs x for $Al_xIn_{1-x}As_ySb_{1-y}/GaSb$, $Al_xGa_{1-x}As_ySb_{1-y}/GaSb$ and $Ga_xIn_{1-x}As_ySb_{1-y}/GaSb$ (left to right). Adapted from [61].

It is clear from these simulations that $AlInAsSb$ is the most promising material to achieve high-energy direct bandgaps. According to the results, the direct-indirect cross-over should occur around an Al composition of $x_{Al} = 0.77$ for $AlInAsSb$, corresponding to a bandgap energy of 1.64 eV, much higher than for $AlGaAsSb$ or $GaInAsSb$. For these reasons, we have set our focus on the $AlInAsSb$ alloy.

4.1.2   AlInAsSb in the literature

$AlInAsSb$, which can be lattice-matched to InP, $InAs$ or $GaSb$ substrates, is an interesting candidate for Sb-based epi-structures. It has recently been proposed for micro- and opto-electronic applications including high-frequency field effect transistors [121], mid-infrared (MIR) multi-quantum well lasers [122], heterojunction bipolar transistors [123], PV systems [124], mid to long wavelength infrared (LWIR) detectors [125] and staircase avalanche photodiodes [126]. However, it has not yet aroused much enthusiasm in the literature. This is likely due to a very large and robust thermodynamic miscibility gap: for layers that are lattice-matched to $GaSb$, it covers the whole $x_{Al} \in [0.05; 0.96]$ composition range at 400°C, and still extends from $x_{Al} = 0.14$ to $x_{Al} = 0.87$ at 1000°C [127]. This

difficulty can be partially overcome by using of non-equilibrium techniques such as MBE, which allows the growth in metastable and unstable regions [128].

We only focus in this section on the epitaxy of $AlInAsSb$ on $GaSb$ substrates, including some results on InP. Other works concerning $InAs$-matched alloys ([129] [130] [131]) and 6.2 $\mathring{A}$ alloys ([123] [132]) are not considered. The epitaxy of $AlInAsSb$ on $GaSb$ was first reported by Washington-Stokes *et al.* [133]. Quaternary compounds were grown lattice-matched to $GaSb$, with various compositions having $x_{Al} \in [0.37; 0.73]$. RHEED, XRD and X-ray photoelectron spectroscopy (XPS) all demonstrated that high-quality structures with smooth interfaces could be grown within the predicted miscibility gap at low growth temperature ($T_{sub} = 355°C$), although sizeable composition variations occurred for substrate temperature variations of $\pm 5°C$. The PL properties of the samples were not investigated.

The digital alloy epitaxy technique was also investigated by Vaughn *et al.* in 2005 in the search for type I mid-infrared multi-quantum well structures using $AlInAsSb$ barriers and $InAsSb$ wells [134]. Digital alloys were preferred over random alloys since, below $400 - 430°C$, unpredictable atomic ordering is known to occur in $InAsSb$ layers [135]. Digital alloys were grown as a sequence of binary compounds, nominally $AlSb$, $InSb$ and $InAs$. Binaries with only one group-V element were chosen in order to avoid competition between the group-V elements, which is hard to control. This was expected to make the layers more reproducible and uniform. The composition and lattice matching to the substrate was determined by the ratio of the binary thicknesses. Layers stable both through time and annealing were obtained in this fashion. Following on [134], Fu [136] and Maddox *et al.* [137] recently reported an in-depth study of $AlInAsSb$ digital alloys. They complemented the structural analysis with PL observations for x_{Al} ranging from 0 to 0.8. Samples were grown following a procedure similar to Vaughn's at a temperature of $480°C$. PL was observed at room temperature for x_{Al} up to 0.75 with bandgap energies ranging from 0.25 eV to 1.24 eV. A significant discrepancy between these observations and the theoretical models ([119] [61]) was noted and attributed to self-ordering effects in digital alloys. However, similar observations were also recently made on random $AlInAsSb$ alloys grown on InP substrates. In 2015, Hirst *et al.* obtained good-quality bulk $AlInAsSb$ layers lattice-matched to InP, grown at $325°C$ and $450°C$ [46]. PL observations revealed that the bandgap energies were lower than expected. Careful examination of the peak

70

shape and position showed that this may have been due to carrier localization stemming from composition fluctuations within the material [138]. The PL spectra exhibited a sub-bandgap tail indicating that the photo-emission would be dominated by long-wavelength states. This in turn would induce a decrease in the open circuit voltage, hence the efficiency. Post-growth thermal treatment proved to enhance the quality of the layer [139] [140]. This came with a blue-shift of the PL emission, translating the observed bandgap energies closer to their expected values. No change in the lattice constant was observed. Furthermore it was noted that the sub-bandgap tail of the spectrum significantly decreased for rapid thermal annealing (RTA) above $500°C$, indicating that the material's quality improved. The presence of atom-scale composition fluctuations has been confirmed by atom probe tomography studies since then [141]. The amplitude of the fluctuations was later shown to depend on the growth temperature [142].

Before ending this literature review, we should also mention the recent work of Lyu *et al.*, which consisted of a comparative study of digital *vs* random alloys of $AlInAsSb$ [143]. The digital alloys used were close to the ones used in [134]. The use of migration-enhanced epitaxy (MEE) at the $InSb$-type interfaces proved to reduce the digital alloy surface roughness more than thirty times. An improved root mean square (RMS) roughness of 0.197 nm was estimated for 400 nm of $Al_{0.7}In_{0.3}AsSb$ digital alloy. A similar structure using a random alloy of the same composition achieved an RMS roughness of 0.112 nm. However, scanning transmission electron microscopy (STEM) revealed the presence of periodical structures in the random alloys with a period of 4.06 nm for $Al_{0.4}In_{0.6}AsSb$ and 4.32 nm for $Al_{0.7}In_{0.3}AsSb$. The authors suggested that the phase decomposition of the alloys was not complete since only two satellite peaks appeared in XRD and the STEM lattice pattern was faint to the naked eye. These observations were repeated on multiple samples, ruling out growth or measurement artifacts. Unfortunately, no PL measurements were made.

According to the literature, only digital-alloy $AlInAsSb$ layers lattice-matched to $GaSb$ have demonstrated PL. The discrepancy between the observed and theoretical values of the energy bandgaps was attributed to the digital alloying technique, but no comparison to random alloys has yet been reported.

4.1.3 InAs/GaSb tunnel junctions

TJs are the linking elements between the subcells of an MJ solar cell. Without TJs, the interface between the n-doped top region of the bottom subcell and the p-doped bottom region of the top subcell would make a PN junction opposite to those of the subcells, acting as a parasitic diode and generating photocurrent losses. TJs minimize losses by using a broken-gap (type III) band alignment through which carriers can tunnel. TJs typically require high levels of doping to achieve the appropriate band alignment. However, such levels are sometimes difficult to achieve and can also incorporate defects in the device.

The $GaSb/InAs(Sb)$ system naturally has a broken-gap alignment (illustrated in Figure 4.4), allowing the electrons to tunnel easily at the interface without requiring extremely high doping levels and leading to low resistivities [144] [62]. Moreover, $GaSb$ and $InAs$ have low effective masses, which enhances the tunneling probability [145]. Using a $GaSb/InAs$ TJ, Vizbaras et $al.$ achieved a resistivity of 2.8×10^{-7} Ωcm^2, which is ten times better than an InP-based TJs [145]. The structure of the junction was 20 nm of Si-doped n^--$InAs$ (1×10^{19} cm^{-3}) followed by 20 nm of Si-doped p^+- $GaSb$ (1×10^{19} cm^{-3}). $InAs$ was used rather than $InAsSb$ in order to avoid segregation in the layer. The interface shutter sequence was the following:

- Growth of the $InAs : Si$ layer

- Stopping both In and As (and Si): the surface is slightly In-rich

- Letting Sb flow to create an $InSb - GaSb$ interface

- Opening Ga (and Si), to grow the $GaSb : Si$ layer

The only disadvantage of the $GaSb/InAs$ TJ for solar cells is that the bandgap of $InAs$ is smaller than that of $GaSb$, leading to a small absorption by the junction. To address this issue, Lumb et al recently proposed a broken-gap quantum-well tunnel junction (BG-QWTJ), including an 8-nm $InAs$ quantum well (QW) within a $GaSb$ homojunction [146]. Because the QW is very thin, the $InAs$ absorption is therefore minimized while facilitating the tunneling between the n- and p-type sides of the TJ.
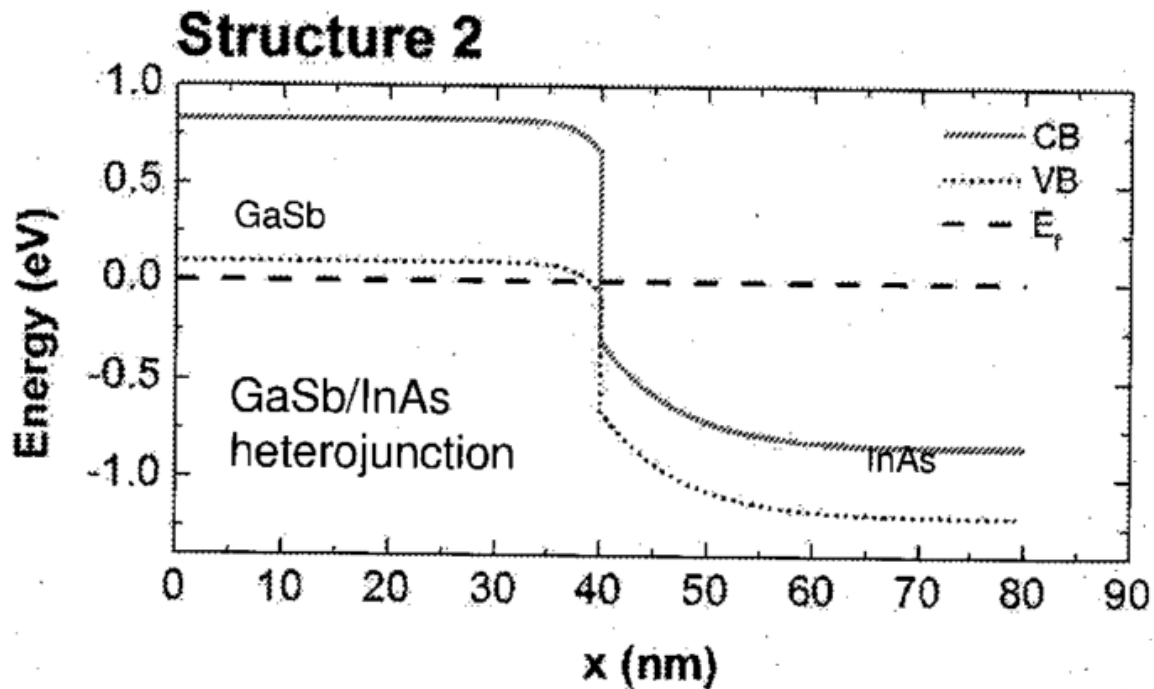
Figure 4.4: Band alignment of a *GaSb/InAs* heterojunction simulated with the NRL MULTI-BANDS modeling software. Adapted from [146].

4.1.4   Summary

As a proof of concept of an all lattice-matched III-*Sb* MJ cell, we intend to fabricate a tandem cell on *GaSb*. According to preliminary calculations, a bandgap of 1.45 *eV* is required for the top cell. To achieve this target, we selected the *AlInAsSb* quaternary compound, whose growth still remains challenging and electronic properties unsure. We selected an *InAs/GaSb* TJ which presents a natural broken-gap alignment. The suggested structure is shown in Figure 4.5
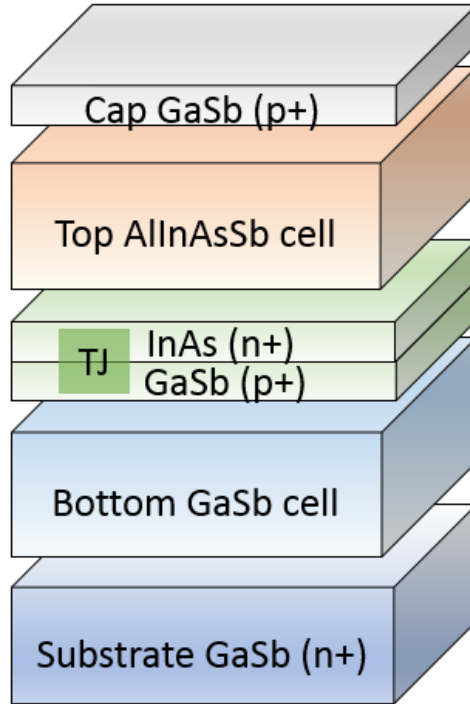
Figure 4.5: Structure proposed for a III-Sb tandem cell showing the selected materials.

4.2 AlInAsSb epitaxy study

Before tackling the tandem cell growth, we studied the growth of the $AlInAsSb$ quaternary alloy and its electronic properties.

4.2.1 Growth conditions

All samples were grown by MBE on $GaSb$ substrates. After deoxidation and the growth of a $GaSb$ buffer, $AlInAsSb$ layers with thicknesses ranging from 50 nm to 100 nm were grown at various temperatures. Thin 20-nm $AlSb$ barrier layers were grown directly below and above the quaternary material in order to block carrier diffusion toward the $GaSb$ buffer layer and surface and enable the observation of PL emission. For all experiments, the growth rate of the quaternary compound was 1 ML/s, obtained by summing up the

group-III growth rates. The As-valve opening was kept constant while the Sb-valve opening was varied in order to adjust the composition. The V/III BEP ratio was kept between 6 and 9. All structures were capped with 50-nm $GaSb$ to prevent oxidation.

In a first set of samples, we studied the effect of growth temperature on composition and structural properties for fixed element fluxes. Then, we grew a second set of samples with different element fluxes, at a fixed growth temperature of $400°C$.

Effect of temperature

First, we grew a series of samples at $400°C$ and $430°C$ while keeping the BEPs constant for all elements. Given that group-III incorporation is not affected by temperature between $400°C$ and $430°C$, the group-III BEPs corresponded to $x_{Al} = 0.53$. $Al_x In_{1-x} As_y Sb_{1-y}$ lattice-matching to $GaSb$, estimated with Vegard's law, occurs for $y = \frac{0.3835 - 0.3439x}{0.4211 + 0.0530x}$. We show in Figure 4.6 the XRD curves taken from two samples, together with the best fits that could be achieved. The compositions derived from the fits were $Al_{0.53} In_{0.47} As_{0.43} Sb_{0.57}$ and $Al_{0.53} In_{0.47} As_{0.48} Sb_{0.52}$ for layers grown at $430°C$ and $400°C$, respectively. Clear Pendellösung fringes indicated high quality and sharp interfaces. Wide-angle scans ($20°$ range) did not show any extra peak above noise level, suggesting that the grown layer was a single phase. Figure 4.6 thus confirms that the growth temperature affects group-V incorporation.

The RHEED behavior was identical for nucleation at $400°C$ and $430°C$. After an initial weakening of the RHEED streaks, their intensity started to be gently modulated. However, while they eventually smoothed out in the case of the samples grown at $400°C$, the modulated streaks of the $430°C$ samples gradually turned into spots, indicating surface roughening. Atomic force microscopy (AFM) (Figure 4.7) indicated only a slightly higher RMS of the sample grown at $430°C$ ($RMS = 0.5$ nm), as compared to the sample grown at $400°C$ ($RMS = 0.2$ nm). However, it is clear from the scans that the morphologies were different, with a factor 10 between the two vertical scales. This confirms the RHEED observations, showing a much rougher surface for the growth at $430°C$.
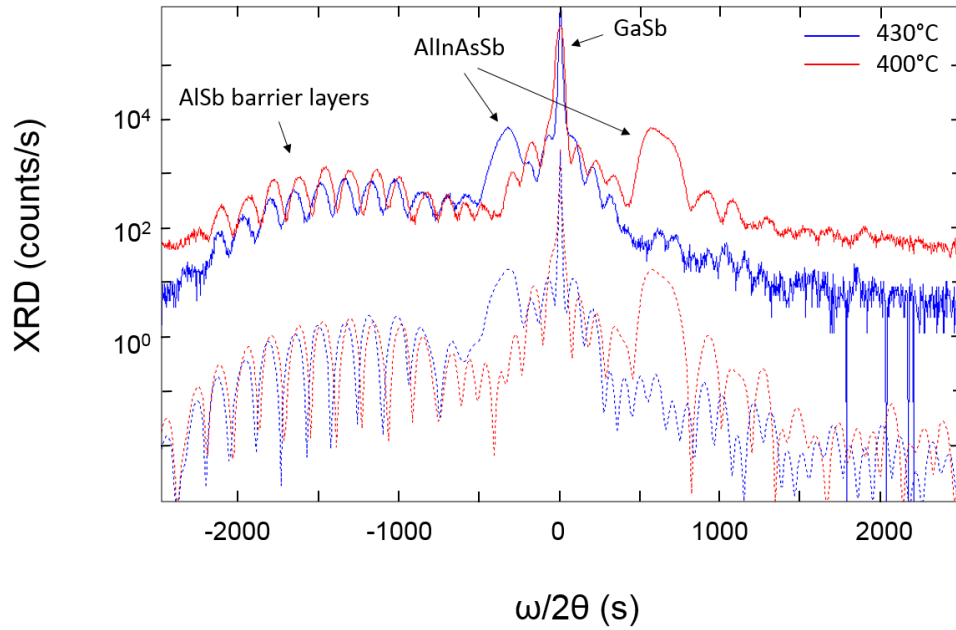
Figure 4.6: XRD symmetric $\omega - 2\theta$ coupled scans of 100-nm thick $Al_{0.53}In_{0.47}As_{1-y}Sb_y$ layers grown on $GaSb$ at $430°C$ (solid blue) and $400°C$ (solid red). Best fits (shifted for clarity) are shown by dashed lines.
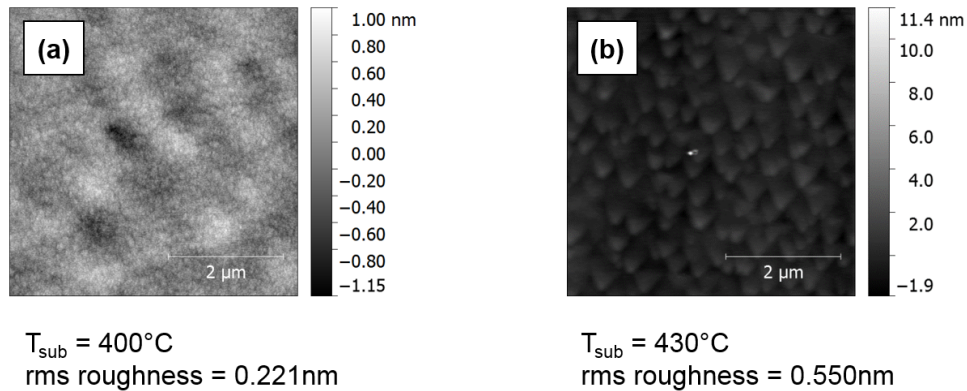
Figure 4.7: 5×5 μm AFM scans of samples containing 100-nm thick $Al_{0.53}In_{0.47}As_{1-y}Sb_y$ layers grown on $GaSb$ at $430°C$ (a) and $400°C$ (b).

Last, the samples grown at $430°C$ did not demonstrate any PL at 300 K, in contrast to those grown at $400°C$. These results indicate that the use of a low growth temperature, around $400°C$, leads to a higher quality of the material. We therefore pursued our study with samples grown at this temperature.

Growth of multiple compositions

We then grew a second set of $Al_xIn_{1-x}As_ySb_{1-y}$ layers lattice-matched to $GaSb$ with $x_{Al} \in [0.25; 0.75]$ at $T_{sub} = 400°C$. The strategy for each composition calibration was:

- using group-III element growth rates (as calibrated with RHEED oscillations) to set the group-III element composition

- inferring the group-V element composition from XRD

- adjusting group-V element fluxes (valves opening) accordingly

- extrapolating to other compositions

The evolution of the Sb content $1 - y$ with the ratio q of the Sb BEP to group-V BEP is shown in Figure 4.8. The experimental data can be well fitted by the following polynomial law: $1 - y = -2.89q^2 + 2.58q + 0.13$.

This allows setting the conditions for the growth of any lattice-matched composition in the $x_{Al} \in [0.25; 0.75]$ range.

4.2.2 Electronic properties

As-grown layers were further characterized by PL spectroscopy. PL was observed at 300 K for Al compositions up to 60%. For higher Al content (compositions of 70% and 75%), PL was only observed at low temperature (70 K and 10 K, respectively). The observed spectra are shown in Figure 4.9. The curves were normalized to the $GaSb$ peak intensity. Although no trend in the peak linewidth (FWHM) was observed, their intensity decreased
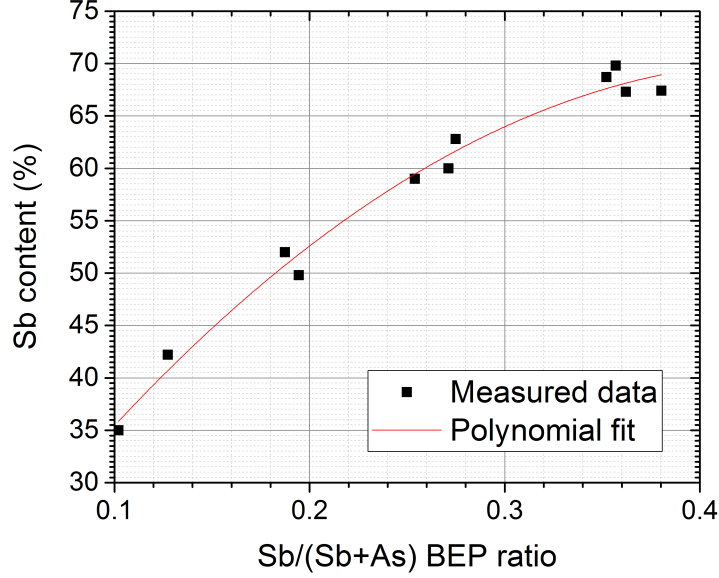
Figure 4.8: *Sb* content in the *AlInAsSb* layers grown lattice-matched to *GaSb* at 400°*C* as a function of the ratio of *Sb* BEP to total group-V BEP. The compositions were estimated by fitting the XRD curves.

with increasing *Al* content, especially for $x > 0.53$. All *AlInAsSb* PL peaks were rather broad at 300 K: their FWHM was in the 83–94 meV range, whereas the substrate PL-line FWHM was around 57 meV. At 70 K, the *AlInAsSb* PL peak FWHM was in the 50–82 meV range. This suggested composition fluctuations in the samples.

We estimated the material bandgap energy from the position of the PL-peak maxima using the equation:

$$E_{gap} = E_{peak} - 1/2k_B T \qquad (4.8)$$

where E_{gap} is the estimated bandgap energy, E_{peak} is the observed PL peak energy, k_B is the Boltzmann constant, and T is the measurement temperature. The results are summarized in Table 4.2.
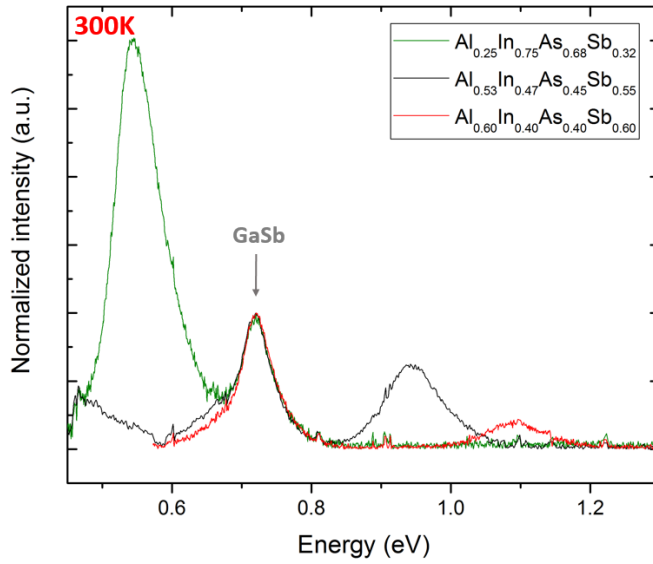
(a)
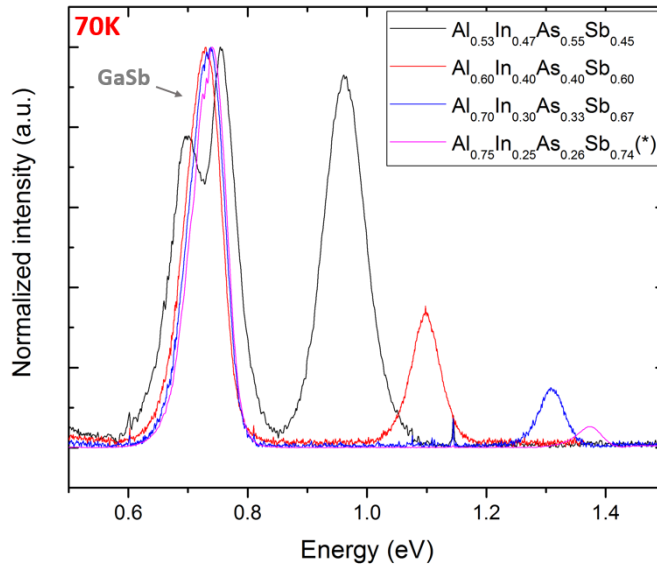
(b)

Figure 4.9: Observed PL spectra at 300 K (a) and 70 K (b) for various compositions of $AlInAsSb$ layers lattice-matched to $GaSb$. The curve noted with a (*) on (b) was actually collected at 10 K. All curves were normalized to the $GaSb$ peak.

79

Table 4.2: Effect of a 1 hr anneal at $T_{sub} = 470 - 475°C$ on PL peak position.

Sample	Composition	Initial PL peak position	PL peak position after anneal
V2452	$Al_{0.53}In_{0.47}AsSb$	0.93 eV	1.00 eV
V2465	$Al_{0.60}In_{0.40}AsSb$	1.09 eV	1.17 eV
V2463	$Al_{0.75}In_{0.25}AsSb$	1.37 eV	1.47 eV

Although random and digital alloys are grown in different ways, the E_{gap} values derived above for random alloys are fully consistent with the values reported by Fu [136] and Maddox *et al.* [137] for digital alloys, especially for low Al concentrations ($x_{Al} < 0.60$). Once again, the observed bandgap energies proved to be well below the bandgap energies predicted in the literature.

The following interpolation matrix is generally used to compute the band parameters of $Al_xIn_{1-x}As_ySb_{1-y}$ from the known constituent ternary (C) and binary (B) compound parameters:

$$Q(x,y) = \begin{pmatrix} y & y(1-y) & 1-y \end{pmatrix} \begin{pmatrix} B_{InAs} & C_{AlInAs} & B_{AlAs} \\ C_{InAsSb} & D_{AlInAsSb} & C_{AlAsSb} \\ B_{InSb} & C_{AlInSb} & B_{AlSb} \end{pmatrix} \begin{pmatrix} 1-x \\ x(1-x) \\ x \end{pmatrix} \qquad (4.9)$$

There is very little information in the literature on estimating the quaternary bowing parameter $D_{AlInAsSb}$. A summary of the existing reports is presented in Table 4.3.

Table 4.3: Values found for $D_{AlInAsSb}$ in the literature.

Value	Reference
0	[61]
-1.2	[122]
-2.5 ± 1.1 eV	[147]

There was a significant discrepancy between the experimental bandgap energies and those computed considering a null quaternary bowing parameter, as shown by Figure 4.10. In fact, much better agreement was achieved when the quaternary bandgap was calculated
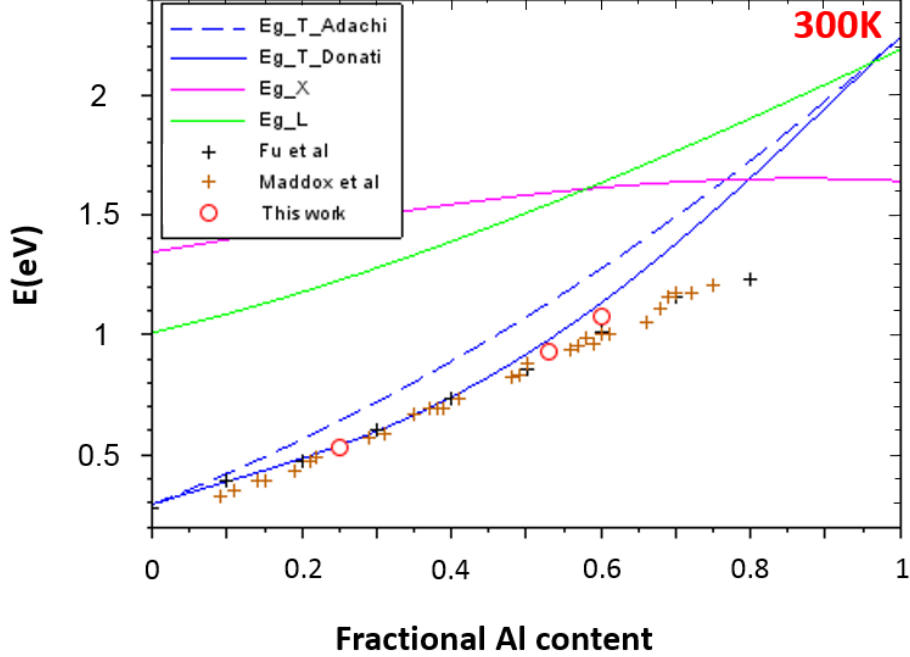
Figure 4.10: Direct and indirect bandgap energies calculated at 300 K for $AlInAsSb$ alloys lattice-matched to $GaSb$ for different values of the quaternary bowing parameter (for the Γ-valley only, the others being set to 0): $D_{AlInAsSb} = 0$ eV (dashed blue curve) [61] and $D_{AlInAsSb} = -2.5$ eV (solid blue curve) [147]. Experimentally observed values by Fu [136] and Maddox et $al.$ and this work are indicated on both models.

using the non-zero quaternary bowing parameter $D_{AlInAsSb} = -2.5eV$ proposed by Donati et $al.$ [147] (Figure 4.10).

Maddox et $al.$ observed room temperature PL from $AlInAsSb$ digital alloys for compositions up to $x_{Al} = 0.75$ [137]. Further, they identified a transition from direct to indirect bandgap at $x_{Al} = 0.72$ (corresponding to a bandgap of 1.18 eV), based on the drop in the PL intensity. It is notable, however, that theoretical calculations estimate a direct-to-indirect cross-over near $x_{Al} = 0.8$, with or without a quaternary bowing parameter (Figure 4.10).

4.2.3 Impact of annealing

Annealing procedure

The samples were then annealed in order to test their thermal stability. Selected samples were cleaved with one part kept as-grown and the other one annealed in the MBE reactor for 1 hr at $475°C$ under a Sb flux. XRD investigations did not show any peak splitting or degradation (peak intensity diminution or FWHM increase), in contrast to what would be expected for phase decomposition.

Measurements

Contrary to the XRD data, the PL peaks demonstrated significant shifts toward higher energies. The results obtained at 70 K are summarized in Figure 4.11 and displayed in Table 4.2. This shift could be explained by a smoothing-out of local composition fluctuations and/or a relaxation of stressed bond configurations arising from the low growth temperature, as previously seen with other material systems [141] [140]. It is notable that PL could be observed up to 70 K with the annealed $Al_{0.75}In_{0.25}As_{0.26}Sb_{0.74}$ layer, which revealed a significant material improvement.

Last, we grew a 1-μm thick $Al_{0.75}In_{0.25}As_{0.26}Sb_{0.74}$ layer following the procedure described previously. The bandgap energy derived from the PL measurement of this sample at 70 K is displayed in Figure 4.11. It should be noted that this bandgap is close to the value of the annealed 100-nm thick layer of the same composition. Indeed, when a thick layer is grown, the early deposited material gets annealed until the end of the growth.

4.2.4 Electron microscopy observations

The samples were then sent to the University of Cadiz for electron microscopy analysis. The measurements and analysis were made by the INNANOMAT team, under the supervision of Professor Sergio Molina. The samples were characterized by (S)TEM techniques. The images were acquired under either high-resolution transmission electron microscopy
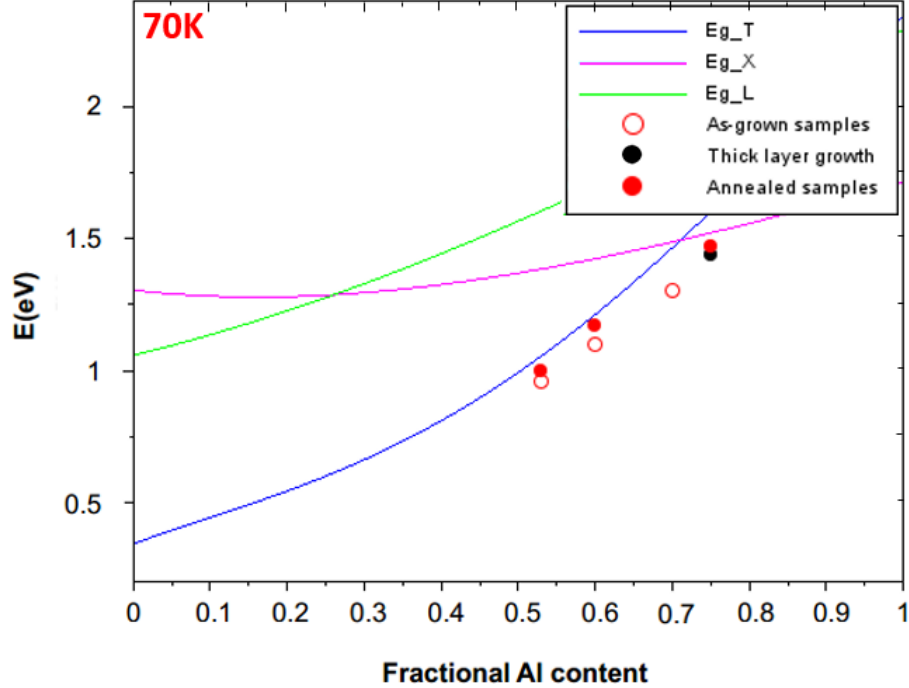
Figure 4.11: Direct and indirect bandgap energies calculated at 70 K for $AlInAsSb$ lattice-matched to $GaSb$ using $D_{AlInAsSb} = -2.5$ eV and experimental values derived from PL measurements at 70 K.

(HRTEM) or aberration-corrected high-angle annular dark-field (HAADF) imaging conditions. Additional spectroscopic techniques, *i.e.*, electron energy loss spectroscopy (EELS) and energy-dispersive X-ray spectroscopy (EDX), were used to establish chemical maps of the distribution of constituents. The compound shown in Figures 4.12 and 4.13 corresponds to a composition of $Al_{0.60}In_{0.40}As_{0.39}Sb_{0.61}$. The quaternary was studied as-grown and annealed (1 hr at 475°C, as described previously).The as-grown sample did not show any particular pattern under the microscope, whereas phase segregation clearly appeared for the annealed sample (Figure 4.12).
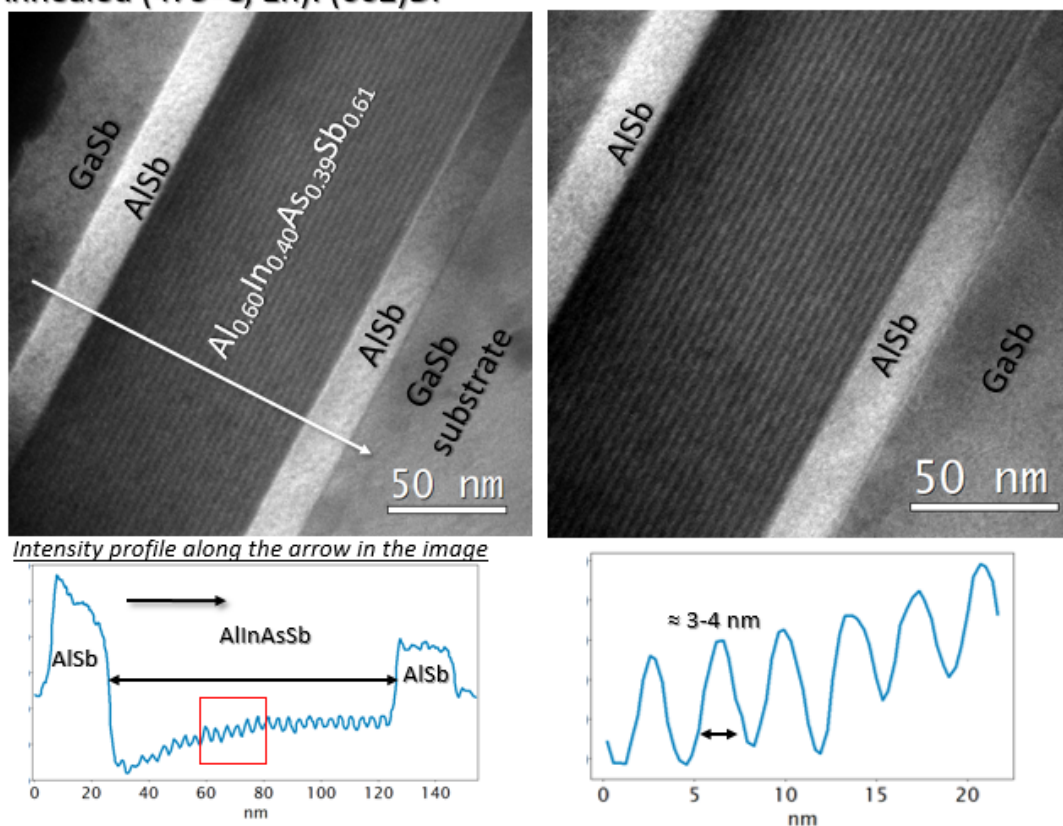
Figure 4.12: Dark-field HRTEM image of the annealed $Al_{0.60}In_{0.40}As_{0.39}Sb_{0.61}$ sample showing phase decomposition. The intensity profile along the white arrow of the TEM images is shown below. Courtesy of M. de la Mata, A.A. Khan and S.I. Molina (University of Cadiz).
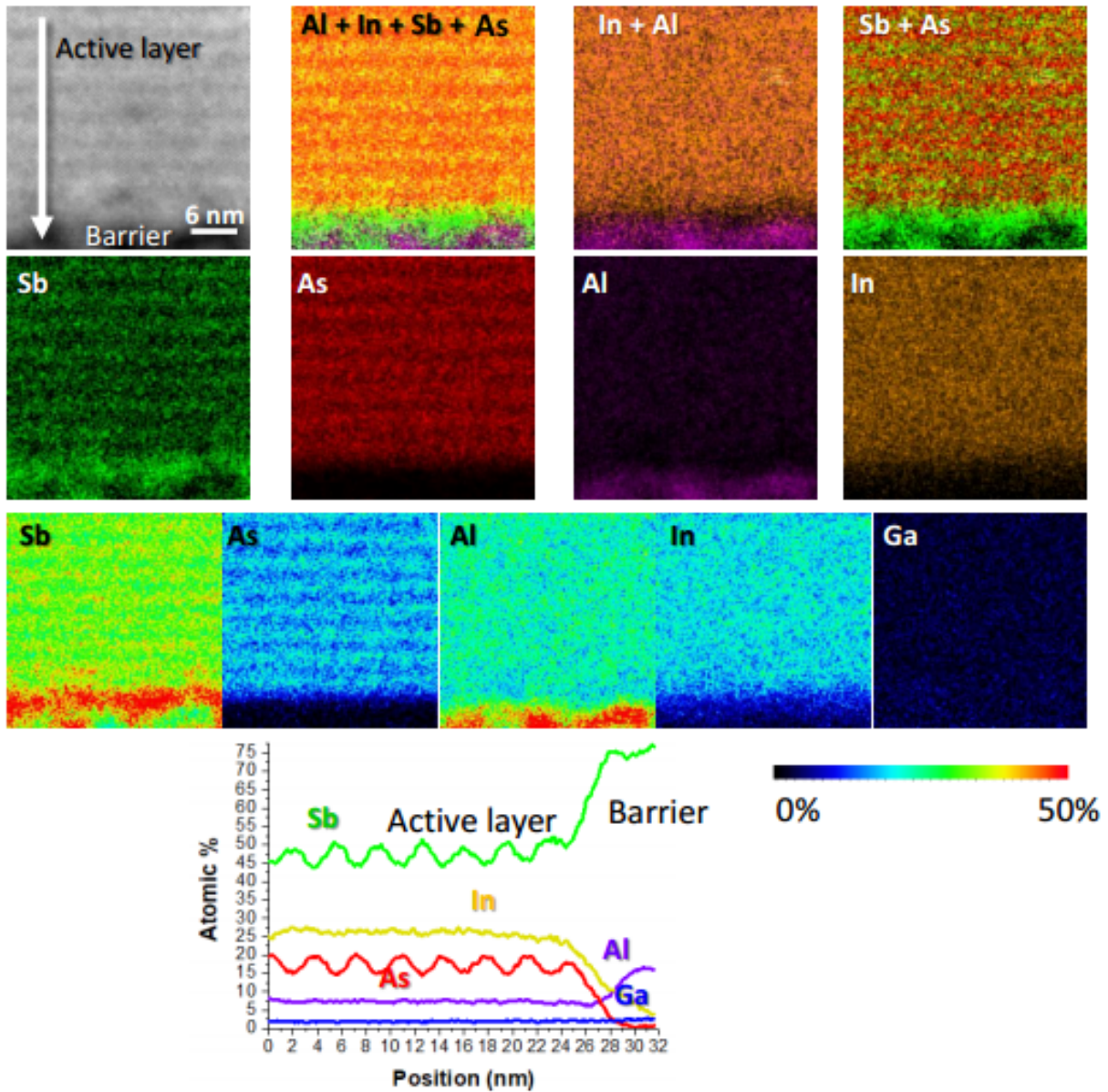
Figure 4.13: EDX analysis of an annealed $Al_{0.60}In_{0.40}As_{0.39}Sb_{0.61}$ sample, illustrating the phase segregation of the alloy. The upper panel collects intensity maps of the constituents (green, red, purple and brown for Sb, As, Al and In, respectively) and some of their RGB combinations, and the bottom row displays the atomic percentage of each element. Courtesy of M. de la Mata, A.A. Khan and S.I. Molina (University of Cadiz).

85

Clear composition fluctuations are visible in the images. The period of the resulting superlattice was estimated at 3.8 nm (approximately 13 ML). This thickness unfortunately corresponds to the rotational peaks in the XRD scans (peaks due to the rotation of the sample during the growth); hence, it went unnoticed in our XRD analysis. The EDX analysis (Figure 4.13) established the presence of alternating As- and Sb-rich regions (about 5% change in composition). The reader might recall that similar observations were made by Lyu *et al.* in [143] (Figure 4.14).

(a) $Al_{0.4}In_{0.6}AsSb$ random alloy

(b) $Al_{0.7}In_{0.3}AsSb$ random alloy
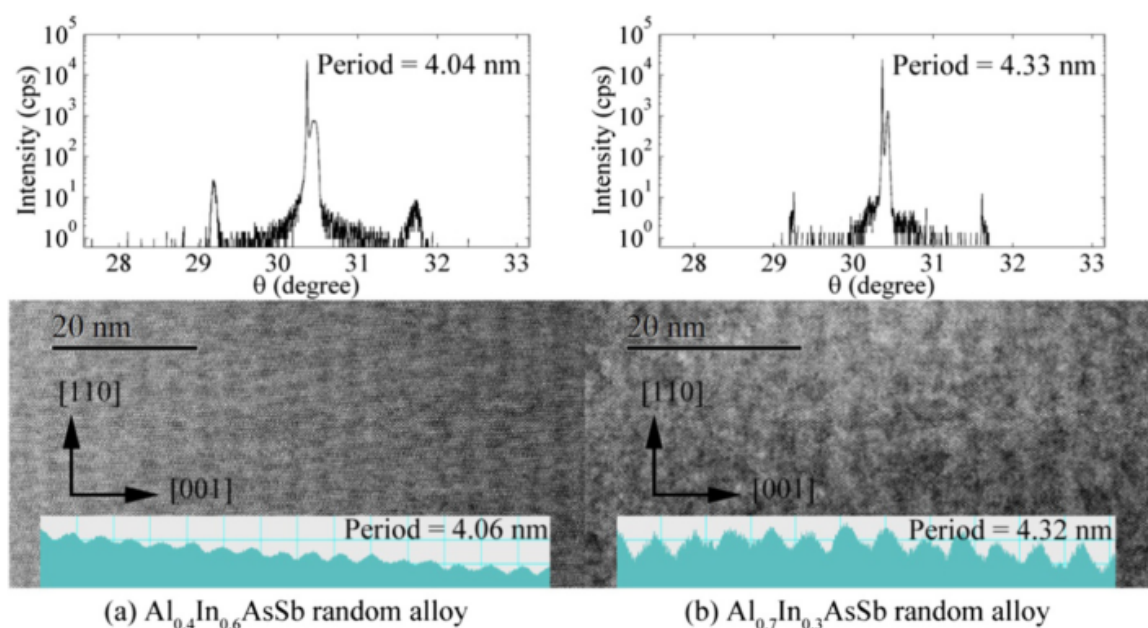
Figure 4.14: XRD and STEM of *AlInAsSb* random alloys with different *Al* fractions confirm their superlattice configuration due to phase segregation. Average line profiles of STEM images are shown in the inset. Fitting periods from XRD peaks are given, which are in accordance with the results of STEM. Adapted from [143].

Although we did not observe these patterns on the as-grown samples, we believe that they also present phase segregation. Higher-resolution techniques such as atom probe tomography might be required to bring it to light. By facilitating diffusion, annealing

probably increases the compositional fluctuations, making them visible to the naked eye (on the TEM pictures). Such observations are also consistent with the results reported for $AlInAsSb$ layers grown on InP [141] [142].

4.2.5   Reproducibility and digital alloy technique

Due to mechanical issues with the Varian GENII As-valve opening system, we attempted the random alloy growth in a Riber Compact 21 reactor. Although the grown samples exhibited mirror-like surfaces and satisfactory RHEED patterns, the XRD scans displayed broad alloy peaks. Scans taken at distinct points of the same sample further indicated a non-uniformity of the $AlInAsSb$ composition through the wafer. This might have been due to the extreme sensitivity of the alloy to the growth temperature and a few degrees of difference between the center and the edge of the wafer. The growth of thick layers resulted in even broader alloy peaks, possibly due to the rising As background, impacting the incorporation of group-V elements. This hypothesis was verified by the growth of $AlInAsSb$ digital alloys.

Because we were unable to reproduce good-quality random alloy growth in a different reactor, we decided to investigate the digital alloy technique. Targeting the $Al_{0.75}In_{0.25}As_{0.26}Sb_{0.74}$ composition, we used the following growth sequence: 6 ML of $AlSb$, 3 s of As soak and 2 ML of $InAs$. The growth rate was $O.5\ ML/s$ and the growth temperature $430°C$. We observed that the longer the growth, the higher the As incorporation in the layers. We attributed this to the As not being evacuated as efficiently as the other components and building a non-negligible background throughout the growth. To counterbalance this effect, we systematically opened the As valve prior to growth and let the As level stabilize. The XRD scan of a 1.6-μm $AlInAsSb$ layer grown on $GaSb$ and sandwiched by 25-nm $AlSb$ layers is shown in Figure 4.15. A thin, high-intensity $AlInAsSb$ peak is clearly visible, although not exactly lattice-matched to the substrate. The satellite peaks correspond to a lattice period of 2.36 nm vs 2.44 nm expected (8 ML). Taking into account the 10% accuracy of the XRD apparatus, the alloy is close to lattice-matching.

At the time this thesis was being written, this sample was under morphological and electronic characterization. Tandem cells incorporating digitally grown $AlInAsSb$ were also
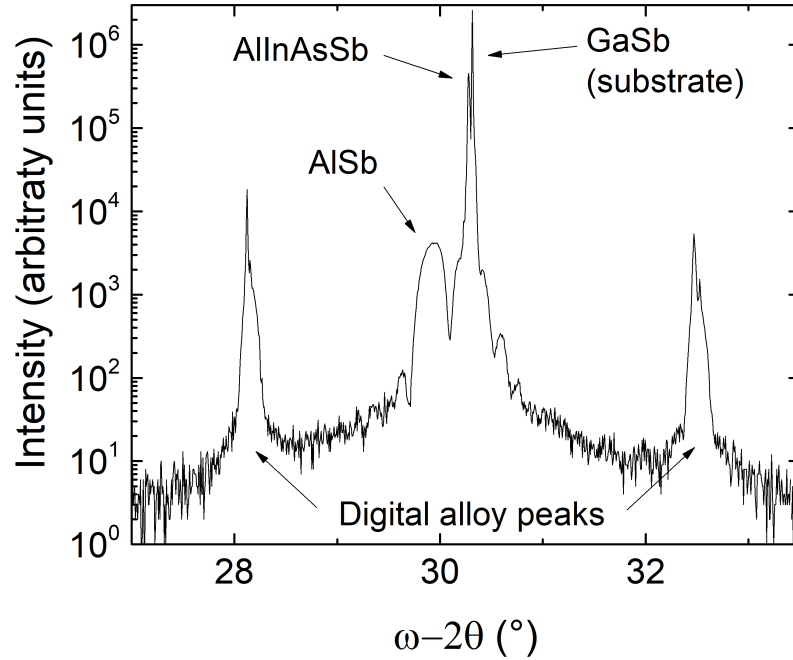
Figure 4.15: XRD $\omega - 2\theta$ scan of an $AlInAsSb$ digital alloy.

being grown and processed for comparison with the cell that is presented in the remainder of this chapter.

4.3   Device fabrication and characterization

4.3.1   Solar cell epitaxy

$AlInAsSb/GaSb$ cells were grown by MBE in the Riber Compact 21 reactor. Upon loading into the growth reactor, 2-inch epi-ready n-type (001) $GaSb : Te$ substrates were deoxidized under Sb flux at 550°C. After 20 minutes of deoxidation, the temperature was lowered to 500 °C to grow a 200-nm $GaSb$ buffer layer. The solar cell growth was then initiated at the same temperature. Be and Te were used for p- and n-type doping, respectively. The solar
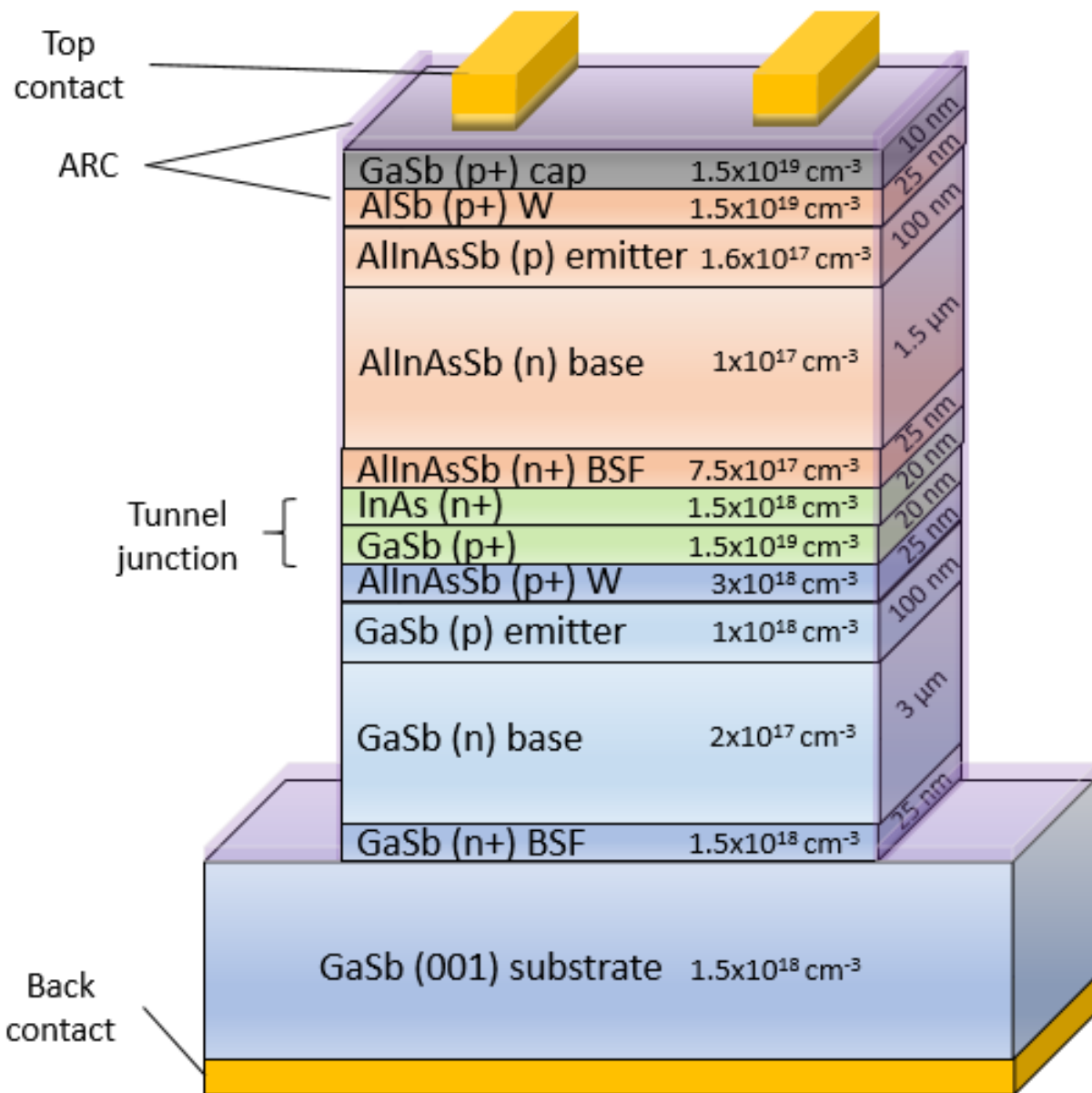
Figure 4.16: Schematic structure of the $AlInAsSb/GaSb$ tandem solar cell. "'W"' stands for window.

cell structure is shown in Figure 4.16. The bottom subcell was made of a 25-nm $GaSb$ BSF, a 3000-nm $GaSb$ base, a 100-nm $GaSb$ emitter, and a 25-nm $AlInAsSb$ window layer. The growth temperature was lowered to 400°C for the window layer and remained at that value until the end of growth. A 20/20-nm $GaSb/InAs$ TJ served to connect the subcells. The second subcell was made of a 25-nm $AlInAsSb$ BSF, a 1500-nm $AlInAsSb$ base, a 100-nm $AlInAsSb$ emitter, and a 25-nm $AlSb$ window layer. The composition used in the whole structure was $Al_{0.75}In_{0.25}As_{0.26}Sb_{0.74}$. The structure was eventually capped with a p-doped 10-nm $GaSb$ contact layer, which also provided protection to the active region during the subsequent processing steps.

The $\omega - 2\theta$ XRD scan of the tandem cell is shown in Figure 4.17. A scan of the top subcell structure (grown on a $GaSb$ substrate in similar conditions) is also shown. The broadness of the quaternary peak in the tandem scan suggested a gradient in composition throughout growth. The quaternary alloy was not lattice-matched and simulation of the top subcell scan estimated its composition at $Al_{0.75}In_{0.25}As_{0.29}Sb_{0.71}$. Still, the RHEED pattern was streaky and the surface appeared smooth (mirror-like with some defects). We thus decided to proceed to cell fabrication.

4.3.2   Cell processing

The procedure for tandem $AlInAsSb/GaSb$ solar cells was similar to the one used in Chapter 3 for homoepitaxial $GaSb$ cells. The process comprised four steps: front contact metallization, mesa etching, surface and side passivation, and back contact metallization. For the front contact, Ti/Au 30/250-nm was deposited by electron beam evaporation. The cells were then isolated from each other via 5-μm high trenches for MJ cells. These were realized by ICP RIE using a $BCl_3 : Cl_2 : Ar$ gas mixture. Once the cells were isolated, a $SiN_x : H$ film was deposited by PECVD at 200 °C on the full sample. An ARC thickness of 106 nm was targeted. The ARC was subsequently etched on top of the bus bars to open access to the metallic contact for electrical wiring. For this step, ICP RIE was again employed. Last, $Pd/AuGeNi$ 5/200-nm layers were deposited by sputtering on the whole back surface. At the end of the processing, the samples were cleaved into individual cells and mounted on TO-8 holders with silver paint.
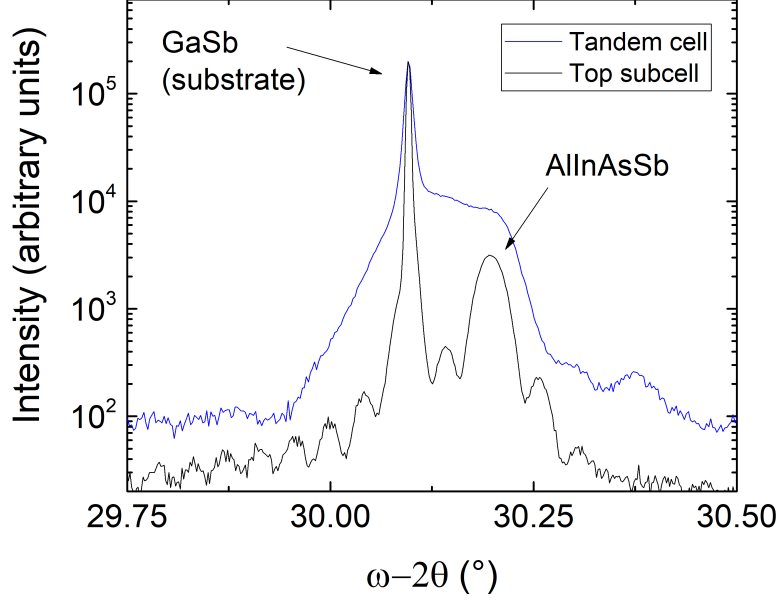
Figure 4.17: XRD $\omega - 2\theta$ scan of the $AlInAsSb/GaSb$ tandem cell (blue) and the $AlInAsSb$ top subcell (black) grown in the Riber Compact 21 reactor.

4.3.3 Device characterization

Electrical characterization

Table 4.4: Measured J-V parameters for the double-junction $AlInAsSb/GaSb$ cell: 1-sun efficiency (η), fill factor (FF), short-circuit current density (J_{SC}) and open-circuit voltage (V_{OC}). Parameters for the stand-alone $GaSb$ cell are also recalled.

Cell type	η (%)	FF	J_{SC} (mA/cm^2)	V_{OC} (mV)
$GaSb$	5.9	0.59	36	280
$AlInAsSb/GaSb$	5.2	0.48	12	900

The cell's electrical parameters are summarized in Table 4.4 and the resulting curve is shown in Figure 4.18. Under AM1.5G, the tandem cell was 5.2% efficient, with V_{OC} of 900

91
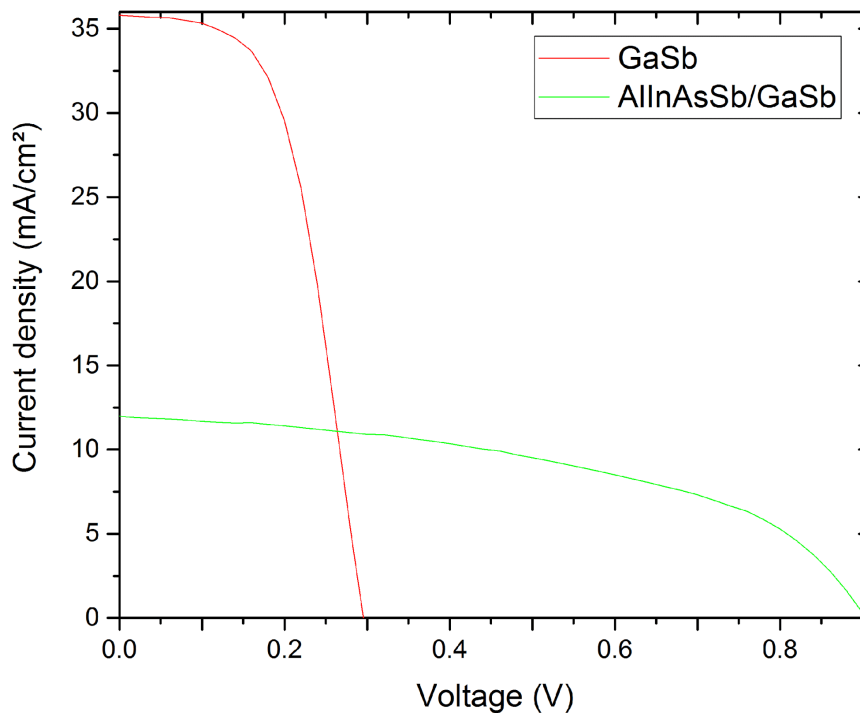
Figure 4.18: Measured J-V curves for mono-junction *GaSb* cell and double-junction *AlInAsSb/GaSb* cell.

mV, J_{SC} of 12 mA/cm^2, and FF of 48%. This performance was poorer than expected, despite a significant increase in V_{OC}. As a reminder, the *GaSb* cell studied in Chapter 3 had an efficiency of 5.9% with J_{SC} of 36 mA/cm^2. The efficiencies of the single- and double-junction were of the same order of magnitude, indicating that the addition of the top subcell did not degrade the tandem device. It is premature at this point to state that the top subcell is limiting, although we suspect it. It takes additional optical character-ization, presented below, to confirm this hypothesis. Last, we should mention that the 10-nm *GaSb* cap layer was not thick enough to withstand all fabrication steps. This led to partial oxidation of the high-Al-content alloys, as displayed in Figure 4.19, possibly adding

to current losses.
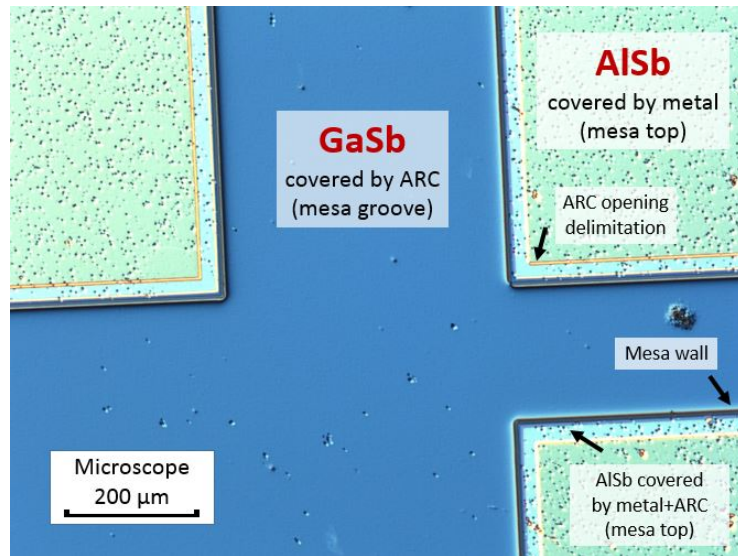
Figure 4.19: Optical microscope picture showing the oxidation of the processed $AlInAsSb$ surface (mesa top).

Optical characterization

The optical characterization of the device was delicate since it is impossible to isolate the subcells. If blue light is shone on the cell, for example, it will be absorbed by the top subcell, leaving the bottom subcell non-illuminated. The bottom subcell will not produce any current and will limit the combined cell output, resulting in a reduced QE. Optical and voltage biases are necessary to provide a better estimation of the tandem cell measurement. Added to the monochromatic probe, blue-light bias is used to obtain the bottom subcell QE and red-light bias to obtain the top subcell QE. A voltage bias approximately equal to half the tandem V_{OC} under biased illumination also ensures that the limiting cell is at short circuit and prevents over-estimation of the QE. For further detail, the reader can refer to [148] and [149]. For the measurements presented in Figure 4.20, a halogen lamp

with a high-pass filter at 1000 nm was used to measure the top subcell and a green laser (540 nm) to measure the bottom subcell. The green laser wavelength seemed to correspond to the high-QE region of the top subcell.
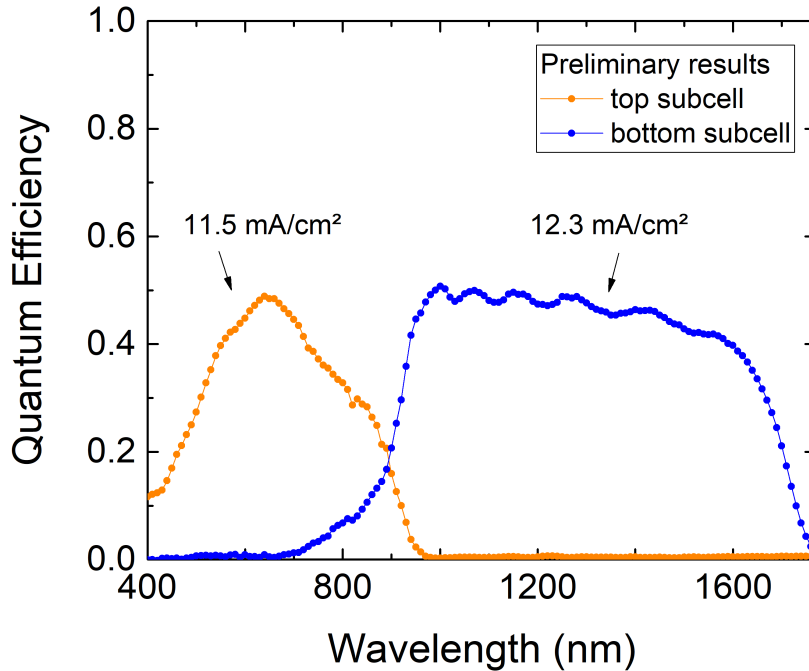
Figure 4.20: Preliminary QE measurements for the tandem cell.

The measurements showed a limiting top subcell with an approximate J_{SC} of 11.5 mA/cm^2, close to what was observed in the J-V characterization. However, the measurements on multiple cells originating from the same epitaxial sample were not consistent, indicating that the optical biases were insufficient to isolate the subcells entirely. The bottom subcell QE intensity was also much lower than the QE of the stand-alone $GaSb$ cell studied in Chapter 3, suggesting some experimental limitation. Still, interesting information could be drawn from these preliminary measurements. The QE estimated for the top subcell increased until 640 nm and then decreased. For the wavelengths shorter than 640

nm, the QE losses were likely due to the unoptimized ARC along with absorption losses in the cap (if it still exists) and window layers. For wavelengths longer than 640 nm, the decrease in QE could be due to a low carrier diffusion length or to a small base thickness. Measurements made on cells with similar bottom subcells and with top subcells of close atomic composition all showed a limiting top subcell with a maximum QE between 1.88 and 1.97 eV and signal extinction between 1.28 and 1.33 eV. We present these points in Figure 4.21.
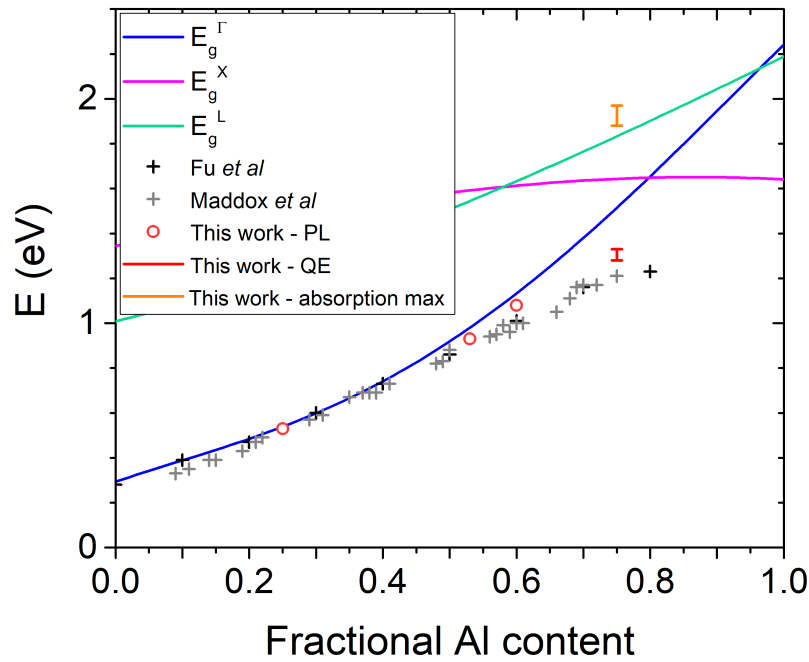
Figure 4.21: Summary of bandgap reports for *AlInAsSb*.

These data points are, once again, coherent with the observations reported in the literature, with an inferred bandgap energy lower than predicted. The lower bandgap value would induce an unbalanced distribution of the photogenerated current, making the bottom subcell limiting and reducing the total current of the series-connected device. Thus far, however, this has not been a concern since the design and/or quality of the top

subcell seems still insufficient to provide enough photocurrent. Improving the top subcell is therefore primordial before adapting the tandem cell design to the reported electronic properties.

4.4 Summary

In this chapter, we investigate a $GaSb$-based MJ structure. First, we estimated the bandgap required to optimize a tandem cell design. Then, taking into account recent progress in the literature, we selected the appropriate materials. The top cell, in particular, should be made with $AlInAsSb$. This quaternary presents a considerable miscibility gap and there is a discrepancy between theory and experimental observations of its electronic properties. We conducted our own growth and PL study of $AlInAsSb$, achieving good-quality layers. We also report the first PL demonstration from random alloys. The results are consistent with the observations in the literature([143] [141] [142]): the alloy seems to exhibit phase decomposition, forming a natural superlattice of As- and Sb-rich regions. The resulting solar cell achieves a performance lower than expected. This likely stems from a low carrier diffusion length and/or a small base thickness in the top subcell. Nevertheless, this work is a first step toward the development of $GaSb$ all lattice-matched MJ solar cells. We show that high bandgaps are achievable and low-loss tunnel junctions available at this lattice parameter. Fabrication and characterization of stand-alone $AlInAsSb$ subcells is currently in progress to improve the top subcell.

Chapter 5

GaSb-on-Si solar cells

The third building block of this project is the integration of the SJ $GaSb$ cell onto a Si substrate, in order to lower the cell's fabrication costs. The challenges of this approach were briefly introduced in Chapter 1. In the first part of this chapter, we explore in details the growth aspects of III-Sb onto Si. We also provide an in-depth review of the integration of III-V solar cells onto Si. Then, we present the adapted fabrication (epitaxy and processing) procedure for the hybrid solar cell and, last, we assess the cell's performance and compare it to that of the stand-alone $GaSb$ cell.

5.1 III-V solar cells on Si

5.1.1 Challenges

Heteroepitaxy corresponds to the growth of a sequence of layers of different materials, all in at least partial registry with each other. Assuming similar crystal structures (*e.g.*, face-centered cubic), a simple assessment of the potential geometric matching is the direct comparison of the lattice constants of the two materials. The lattice mismatch parameter $\frac{\Delta a}{a}$ is defined in percentage as:

$$\frac{\Delta a}{a} = \frac{a_{epi} - a_{sub}}{a_{sub}} \tag{5.1}$$

where a_{epi} is the lattice constant of the grown material and a_{sub} is the lattice constant of the substrate. The lattice mismatch parameters between the materials used in this work are summarized in Table 5.1.

Table 5.1: Material parameters. Source: [150].

III-Sb compound	Lattice parameter $(\mathring{A})$	Mismatch with Si $(\%)$	Thermal expansion $(\mathring{A}/K)$
Si	5.4310	0	1.41×10^{-5}
$GaSb$	6.09593	12.24	4.72×10^{-5}
$AlSb$	6.1355	12.98	2.60×10^{-5}
$InSb$	6.47937	19.30	3.48×10^{-5}
$GaAs$	5.65330	4.09	3.88×10^{-5}
$AlAs$	5.66139	4.22	2.90×10^{-5}
$InAs$	6.0583	11.54	2.74×10^{-5}

When a good arrangement cannot be achieved while bringing the two surfaces into contact (by rotation of a lattice for example), the bonds at the interface are highly perturbed and have to relax in some way. This is the case for common binary III-V compounds on Si. If the mismatch is not too high, it can be contained up to a certain so-called critical thickness where the layers are strained. Above the critical thickness, however, the stress is relaxed through the formation of dislocations so that the crystal can lower its energy. Depending on the level of strain, Stranski-Krastanov growth could occur, where the stress is elastically relaxed through the formation of islands, before generation of dislocations. Islands formation and coalescence also occur in the Volmer-Weber growth mode, driven by surface energy, possibly leading to the creation of defects such as micro-twins[1] as well as dislocations. For III-V materials, there is also a significant thermal mismatch with Si which can lead to cracks and wafer bowing under high changes in temperature (to be

---

[1]Crystallites sharing lattice points and growing in distinct symmetrical orientations.

considered in CPV applications) [151]. Typical heteroepitaxial defects are summarized in Figure 5.1. The majority of these defects are responsible for the increased broadness of the epitaxied material XRD peak. The FWHM of the rocking curve is thus a good indicator of the crystalline quality. In the case of solar cells, dislocations are particularly detrimental for device performance. If the threading dislocations propagate into the active region of the solar cell, they can act as non-radiative recombination centers, reducing the minority carrier lifetime. The TDD is therefore an important criterion to estimate the grade of III-V layers on Si.

(a) mismatch

(b) misorientation

(c) dislocation content

(d) mosaic spread

(e) curvature

(f) relaxation

(g) inhomogeneity
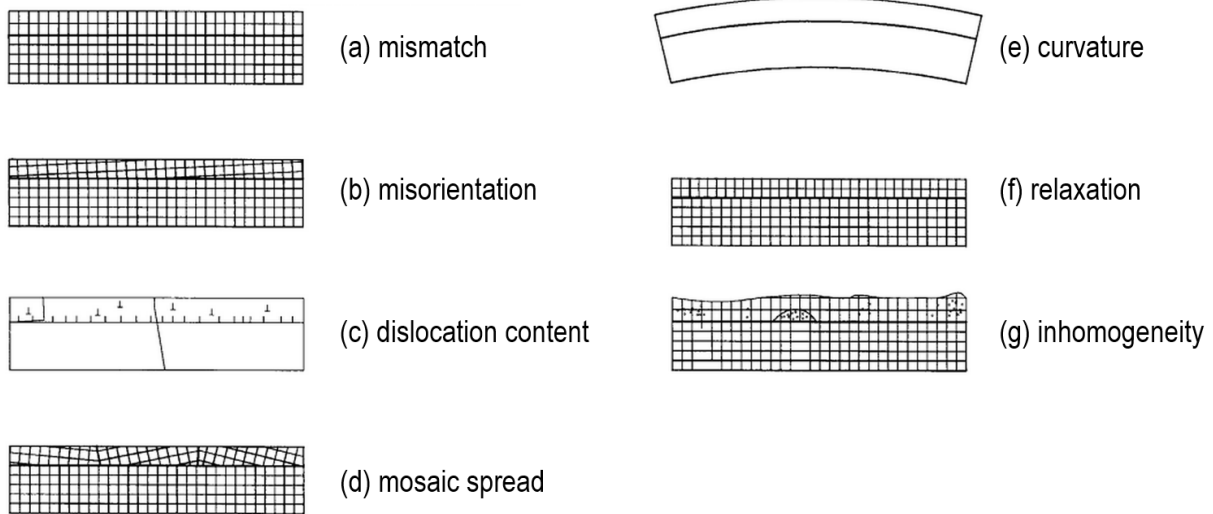
Figure 5.1: Defects created to relieve strained layers in heteroepitaxy. Adapted from [152].

In addition to these geometric considerations, the distinct crystallographic structures of III-V alloys and Si raise the issue of the growth of a polar material on a non-polar material, inducing the creation of anti-phase domains (APDs) at the boundaries of which non-radiative recombination can also occur [153]. The emergence of APDs can be prevented by the use of miscut substrates that create a double-stepped starting surface [154] [155].

5.1.2 Heteroepitaxy techniques for III-Sb on Si

The first attempts at integrating III-V on Si date back to the 80s. The epitaxy of $GaAs$ on Si was then widely studied [156] [157] [158] [159]. In contrast, very few groups have studied the growth of $GaSb$ on Si. The first report was presented by Malik *et al.* in 1986 [160], drawing on previous findings on the growth of $GaSb$ on $GaAs$ [161] [162] [163]. The authors used a 600-nm thick $AlSb$ buffer layer and multilayers of $AlSb$ and $GaSb$. Optical devices were grown on top of the structure and proved to be operational. Since then, multiple growth techniques have been developed to produce strain free III-V layers on Si with low TDDs. In the following, we present a selection of methods and their main achievements, focusing on the epitaxy of III-Sb on Si. This review deals with standard MBE growth only, not including recent advancements in MOVPE or selective area epitaxy.

$AlSb$ nucleation layer

Following the work of Malik *et al.* [160], Akahane *et al.* suggested that $AlSb$ islands could block the diffusion of Ga atoms on the Si surface, enabling subsequent $2D$ growth of $GaSb$ and limiting the generation and propagation of dislocations [164] [88]. The optimum parameters for the nucleation layer were found to be: $T_{sub} = 500°C$ and $t_{AlSb} = 5 \ nm$. FWHM below 550 $arcsec$ (rocking curve) were observed for 500-nm thick $GaSb$ layers grown with an $AlSb$ nucleation layer, *vs* 707 $arcsec$ for a 500-nm thick $GaSb$ layer directly grown on Si. Below 450°C, the surface migration was suppressed and, above 560°C, Sb desorbed. The authors also highlighted the contribution of the $AlSb$ nucleation layer in terms of surface morphology: the AFM study estimated the RMS roughness of $GaSb$-on-Si buffers above 100 nm, *vs* 2 nm only for $GaSb$-on-$AlSb$ on Si buffers (1-μm thickness).

Kim *et al.* [165] [166] and Huang *et al.* [85] further evidenced the formation of a 90° misfit dislocation array at the $AlSb/Si$ interface, efficiently relieving the strain. Following the example of other authors, we refer to this array as the IMF. The growth mechanisms of $AlSb$ on Si were studied in detail by Balakrishnan *et al.* [167] [168] and Vajargah *et al.* [169], confirming that $AlSb$ is a suitable template for the growth of III-Sb on Si. Very recently, Rodriguez *et al.* proposed optimal nucleation conditions of 4 ML of $AlSb$ at

$450°C$ prior to the growth of $GaSb$ [170]. Post-growth annealing further enhanced the material quality, lowering the FWHM value down to 235 $arcsec$ (rocking curve) for a 1-μm thick $GaSb$ layer. TDDs in the 10^9 cm^{-2} range were evaluated for these thin samples [91].

Buffer layers

Buffer layers are commonly used to obtain high-quality material. In heteroepitaxy, their first purpose is to accommodate the mismatch between the active zone and the substrate by letting the dislocations propagate and annihilate through the buffer thickness. For example, Vernon *et al.* presented a study of the evolution of the TDD in a $GaAs$ solar cell grown on Si as a function of the buffer thickness in [73]. For $GaSb$ on Si more specifically, Rodriguez *et al.* showed a significant reduction in the FWHM ($GaSb$ rocking curve) with increasing buffer thickness [170]. Another merit of buffer layers is that they incorporate and bury contaminants potentially present at the substrate surface or in the growth reactor, leaving a clean environment for the growth of subsequent layers.

Thick (≥ 2 μm) buffer layers are generally employed to reduce the TDD in the active zone of III-V devices grown on Si [73] [76]. The resulting TDDs are estimated in the $10^6 - 10^8$ cm^{-2} range. However, such thick layers can also induce higher electrical (carrier collection) and absorption losses in solar cells, especially in MJ cells. Obviously, if Si is to be used as an inactive substrate only, the thickness of the buffer is less of an issue. Last, thick buffer layers are time (and money)-consuming and sometimes require additional polishing steps. A compromise thus has to be found between adding up losses and/or complexity and reducing the TDD with increasing buffer thickness.

We mentioned the compositionally graded buffer approach in Chapter 1. Making use of the flexibility of III-V alloying, graded buffers consist of superimposed layers of increasing (or decreasing) lattice parameters, or of a layer whose lattice parameter varies continuously. The resulting composition gradient induces increasing strain, creating and propagating dislocations until they annihilate by encountering others. This technique is widely used in metamorphic solar cells. However, in the specific case of $GaSb$ on Si, the significant mismatch ($\sim$ 12%) implies highly complex buffer structures. As a comparison point, to accommodate the 4% mismatch between $GaAs$ and Si, Dimroth *et al.* used a 1-μm

thick graded $GaAs_yP_{1-y}$ buffer made of seven steps [171]. The authors estimated that the resulting TDD at the top of the buffer was still superior to 10^8 cm^{-2}. To achieve an improved TDD of 5.25×10^6 cm^{-2}, Yaung $et\ al.$ used a 40-nm GaP nucleation layer, followed by a 550-nm GaP buffer and a 3.6-μm graded $GaAs_yP_{1-y}$ buffer made of 28 steps [79]. The graded buffer approach therefore seems barely scalable to the mismatch between III-Sb and Si.

Thermal cycle growth and annealing

Thermal cycle growth (TCG) and thermal cycle annealing (TCA) can be used to further encourage the dislocation glide and annihilation. TCA has been used in studies of the heteroepitaxy of $GaAs$ on Si [172] [73] [74] [173] [174][175]. They consist of multiple post-growth anneals at high temperature to reduce the dislocation density. With the rapid changes in temperature, the grown films undergo multiple compression and tension forces, forcing the dislocations to move in several directions and increasing their chance to meet other dislocations. On top of the added growth complexity, two major drawbacks should be noted for this technique: first, in highly mismatched systems, the difference in thermal properties can generate more dislocations or even cracks in the material; and second, the high temperatures can induce interdiffusion between the substrate and the epilayer, adding contaminants hence potential non-radiative recombination centers. In the specific case of $GaSb$ on Si layers, post-growth annealing proved to enhance the crystalline quality, although no cycling was employed [170].

Two-step growth

Simpler than the TCG and TCA techniques, the two-step growth technique is widely employed for III-V growth on Si [156] [90]. The first step is only a few nm thick and made at low temperature. The use of a low temperature makes it possible to hinder the mobility of the deposited atoms and makes the coverage more uniform, reducing the likelihood of island formation. Even though a layer grown at low temperature contains more defects, these punctual defects are easier to eliminate than planar defects and the

dislocations generated by the coalescence of islands. Subsequent annealing improves the quality of the nucleation layer. The rest of the growth proceeds at high temperature. For the first step, techniques such as alternating layer MBE[3] ([176] [177]) and solid-phase epitaxy[4] ([178] [179]) have been employed. In the case of III-Sb growth on Si, Rodriguez *et al.* made an extensive study of the impact of the nucleation layer growth temperature on the structure's crystalline quality [170]. The authors showed that the optimal growth temperature depended on the nucleation layer thickness. The best results were given by nucleation in the $450 - 500°C$ range.

Advanced dislocation filtering layers

The influence of a constraint like a heterogeneous interface on a threading dislocation is characterized by its Peach-Koelher force [180]. When the force is null or insufficient, the dislocation pursues its propagation across the material. When the force becomes higher than a critical value, it bends the dislocation, forcing it to propagate transversally until it meets another dislocation, potentially annihilating or merging into a single propagating dislocation. The dislocation can also bend back toward the substrate. Hetero-interfaces are also helpful in eliminating segregating contaminants. By offering many heterogeneous interfaces, superlattices are an efficient filter for dislocations. They were first used as such by Matthews *et al.* in 1974 [181]. In the context of III-V growth on Si, $GaAsP/GaAs$ strained-layer superlattices (SLSs) [182] and quantum dots (QDs) filtering [183] have been used with success. These techniques have also been applied to the growth of $GaSb$ on $GaAs$, presenting similar characteristics to the growth of $GaSb$ on Si (large lattice mismatch and formation of an IMF). $GaSb/AlSb$ SLSs in particular have proven to reduce the TDD from the 10^9 cm^{-2} range down to the 10^7 cm^{-2} range, acting more efficiently than thick $GaSb$ buffer layers [184]. Similar TDDs have been achieved recently by Mansoori *et al.* with plain $AlSb$ blocking layers [115]. For the case of III-Sb on Si, multiple pieces of work have combined $AlSb$ blocking layers, $GaSb/AlSb$ SLSs and/or $InSb$ QD layers to produce

---

[3]Alternative deposition of group III and V monolayers. This technique helps to ensure a better control of the III-V/Si interface composition.

[4]Use of an amorphous nucleation layer further annealed and recrystallized.

metamorphic buffers [185] [186] [187]. For example, Sasaki *et al.* recently achieved a TDD just below 10^8 cm^{-2}, still four times higher than in similar structures grown on $GaAs$ [188].

Summary

The reader might recall that a TDD below 3×10^5 cm^{-2} is needed to drastically limit non-radiative recombination losses in metamorphic solar cells [48]. Despite the cornucopia of innovations, this target is barely achievable in practice. Recently, Yaung *et al.* achieved an impressive TDD of 5.25×10^6 cm^{-2} with a 40-*nm* GaP nucleation layer, followed by a 550-*nm* GaP buffer and a 3.6-μm graded $GaAs_y P_{1-y}$ buffer made of 28 steps [79]. Concerning III-Sb growth on Si more specifically, research groups are still struggling to fall below the 10^8 cm^{-2} TDD range, even with the help of complex dislocation filtering structures [188]. Simpler methods employing two-step growth and an $AlSb$ nucleation layer exhibit TDDs in the 10^9 cm^{-2} range.

5.1.3 III-V-on-Si solar cells: state of the art

Interest in III-V-on-Si solar cells initially arose four decades ago. Research efforts were unfortunately quickly discouraged by the poor outputs, due to the complex mismatched growth. Recent developments in metamorphic buffer epitaxy, as well as in stacking and bonding techniques, have revived interest in these hybrid systems. Promising results have been achieved over the past years, which are summarized in this section, excluding research on dilute nitrides. Solar cells where Si is used as a bottom cell, and solar cells where it is only used as an inactive substrate, are both considered. Whenever the measurement conditions are not mentioned, the considered spectrum is AM1.5G. Otherwise, the spectrum is specified. This review is based on the works by [189] and [190].

Epitaxial approaches

We have detailed above the three main challenges of the heteroepitaxial integration of III-V compounds on Si: the lattice mismatch generating numerous threading dislocations,

the growth of a polar material on a non-polar material inducing the creation of APDs and anti-phase boundarys (APBs), and the discrepancy in thermal properties leading to cracks and film bending. Thus far, efforts have mainly focused on reducing the TDD.

SJ cells with Si as an inactive substrate

Early attempts at growing $GaAs$ SJ cells on Si employed complex TCG procedures such as the one used in [73]. The resulting solar cell efficiency culminated at 17.6% under 1 sun and 21.3% under 200 suns [74]. Even more sophisticated growth sequences, involving $InGaAs$ and $AlGaAs$ SLSs, reached similar results with 20% efficiency cells [75]. The aforementioned works still hold the record for SJ III-V-on-Si solar cells but were abandoned due to their growth complexity. Since then, researchers have aspired to reproduce these results with simpler structures. In 2005, Andre *et al.* used Si_xGe_{1-x} graded buffers to accommodate the mismatch between Si and $GaAs$, and chemical-mechanical polishing to smooth the surface [76]. The $GaAs$-on-Si cell achieved 18.1% efficiency and the TDD at the top of the buffer was estimated at 1×10^6 cm^{-2}. The total thickness of the buffer layers was not mentioned but similar works have used 10- to 12-μm thick buffers [77]. In 2017, Wang *et al.* used a much thinner (2 μm) Ge buffer layer to accommodate the lattice mismatch and reduce the TDD below 5×10^6 cm^{-2} [78]. The buffer layer was first grown at low temperature (400°C) to ensure smooth nucleation and this was followed at high temperature (650°C). The sample then underwent TCA prior to the III-V cell growth. The SJ $GaAs$ cell resulted in 11.9% efficiency, which could be further improved, given that it had no ARC. All of the works mentioned thus far have employed MOVPE. In 2017, Vaisman *et al.* demonstrated a 15.3% efficiency $GaAsP$ SJ cell grown on Si by MBE [80]. The authors used a 40-nm GaP nucleation layer, followed by a 0.55-μm GaP buffer and a 3.6-μm graded $GaAsP$ buffer made of 28 steps. The step-graded buffer had been optimized by the group over the years to achieve a 5.25×10^6 cm^{-2} TDD [79]. This result is still below the record efficiency $GaAs$ SJ cells on Si ([73] [74] [75]) but presents the advantage of using a simplified growth procedure to achieve a similar TDD.

Two-junction cells with Si as an inactive substrate

Pioneer work was achieved by Lueck *et al.* in 2006 with $GaInP/GaAs$ dual-junction solar cells grown onto Si with Si_xGe_{1-x} buffer layers [191]. A 10-μm graded $SiGe$ buffer was

deposited by UHV chemical vapor deposition on a Si wafer. The resulting TDD was estimated at $1.8 \times 10^6 \ cm^{-2}$. The final device exhibited 16.8% efficiency. The rest of the layers were grown by MBE. In a comparative study between direct growth and wafer bonding for the fabrication of III-V tandem cells on Si, Dimroth *et al.* demonstrated a similar 16.4% efficiency $GaInP/GaAs$ dual-junction cell grown on Si [171]. In this work, a 60-nm GaP nucleation layer was first grown on the Si substrate by MOVPE, followed by a seven-step graded $GaAs_xP_{1-x}$ buffer layer to accommodate the mismatch between Si and $GaAs$. The total buffer thickness amounted to a few microns. Several analysis methods estimated the resulting TDD to the order of $10^8 \ cm^{-2}$. Other works have investigated the growth of $GaAsP/SiGe$ tandem cells on Si. Wang *et al.*, for instance, demonstrated 20.6% efficiency for such a cell in a three-terminal configuration [192]. The graded Si_xGe_{1-x} buffer used in the structure was around 5-μm thick and was grown by reduced-pressure chemical vapor deposition. The rest of the device was grown by MOVPE.

Two-junction cells with Si as an active cell

The record efficiency for MJ cells made of $III - V$ materials grown on Si was long held by Soga *et al.* with an $AlGaAs/Si$ tandem cell of 21.2% efficiency under AM0 [193]. The authors used complex TCG procedures to achieve sufficient MOVPE epitaxial quality. More recently, Grassman *et al.* demonstrated a functioning $GaAsP/Si$ dual-junction cell with an efficiency of 13.1% grown by MOVPE [194]. The device employed a GaP nucleation layer and a step-graded $GaAs_xP_{1-x}$ buffer layer whose thicknesses were not specified. TDD was estimated to the order of $10^7 \ cm^{-2}$.

Three-junction cells with Si as an active cell

The record efficiency for III-V MJ cells directly grown on Si was very recently broken by the Fraunhofer institute [195] [196]. Their $GaInP/GaAs/Si$ cell had an efficiency of 22.3% and used a GaP nucleation layer and a $GaAs_yP_{1-y}$ metamorphic buffer grown by MOVPE.

Non-epitaxial approaches

Although they circumvent the problems related to the high lattice mismatch between III-V materials and Si, the non-epitaxial approaches face several challenges as well. On top of the difficulty of finding an appropriate optically transparent bonding layer, one should also

bear in mind the discrepancy in thermal properties between the materials. The process temperature should be compatible with both materials and minimize the bowing of the films and the formation and propagation of cracks in the sample. In the following, both two-terminal and three-/four-terminal configurations were used to characterize the cells, which gives a fair idea of the electric losses at the interfaces. The measurement conditions are mentioned for each result.

SJ cells with Si as an inactive substrate
No SJ solar cells heterogeneously integrated on Si have been reported thus far.

Two-junction cells with Si as an inactive substrate
In 2014, Dimroth *et al.* used wafer bonding to stack a dual-junction $GaInP/GaAs$ solar cell on an inactive Si substrate [171]. The device demonstrated an efficiency of 26.0% in a two-terminal configuration. This wafer-bonded cell outperformed a similar $GaInP/GaAs$ cell grown on Si as a comparison point (efficiency of 16.4%).

Two-junction cells with Si as an active cell
Tanabe *et al.* demonstrated in 2012 the first direct fusion bonding forming an optically transparent and electrically conductive ohmic heterojunction between $GaAs$ and Si [197]. As part of their demonstration, they proposed a tandem cell made of an $AlGaAs$ top cell and a Si bottom cell. The device achieved 25.2% efficiency in a two-terminal configuration. Mechanical stacking has also been investigated to integrate III-V cells onto Si. Using mainly electrically insulated adhesive layers, this process is usually associated with four-terminal configuration measurements that provide higher efficiencies but increase the complexity of the PV module installation. Nowadays, the efficiency record is held by Essig *et al.* with $GaInP//Si$ and $GaAs//Si$ mechanically-stacked tandem cells with respective efficiencies of 32.5% and 32.8% (four-terminal) [29].

Three-junction cells with Si as an active cell
In 2013, Derendorf *et al.* used the direct wafer-bonding technique to connect a dual-junction $GaInP/GaAs$ cell with a Si bottom cell [71]. The device demonstrated 20.5% efficiency in a two-terminal configuration. A year later, the novel direct metal interconnect method was used to stack a $GaInP/InGaAs$ dual-junction cell on a Si cell [72]. The three-junction device exhibited 25.5% efficiency in a two-terminal configuration and 27.3%

in a three-terminal configuration. More recently, Essig *et al.* fabricated a three-junction cell made of a lattice-matched dual-junction $GaInP/GaAs$ cell mechanically stacked onto a Si cell [29]. The three-junction device reached 35.9% efficiency in the four-terminal configuration but only 30.9% efficiency in a two-terminal configuration. The losses were mainly attributed to a photocurrent limitation by the bottom cell. The record for measurements in the two-terminal configuration is now held by Cariou *et al.* with a dual-junction $GaInP/GaAs$ top cell wafer-bonded to a Si bottom cell [30]. The device achieved 33.3% efficiency.

5.1.4 Summary

In this section, we presented in detail the challenges of the heteroepitaxy of III-Sb on Si, along with the growth techniques. We then reviewed the main achievements in the integration of III-V solar cells onto Si for both epitaxial and non-epitaxial approaches. To our knowledge, no integration of III-Sb cell on Si has been attempted thus far.

5.2 Adapted fabrication process

5.2.1 Substrate preparation

Chemical treatment

Conversely to the $GaSb$ substrates, Si substrates require chemical treatment prior to loading into the MBE. Whenever quarters were needed for the growths, Si 2-inch wafers were diced with a diamond saw. The first step of the chemical preparation was a tri-solvent clean with $(CH_3)_2CO$, C_2H_6O and C_3H_8O (90 s each). We then proceeded to chemical deoxidation. The technique used during this project combined the strengths of both oxide- and H-passivation, taking advantage of the self-etching Si oxidation process (see Figure 5.2).

We followed the procedure described in [199]. The authors studied cycles of HF dips and O_2 plasma exposure. The former removes hydrocarbons and any contaminants trapped
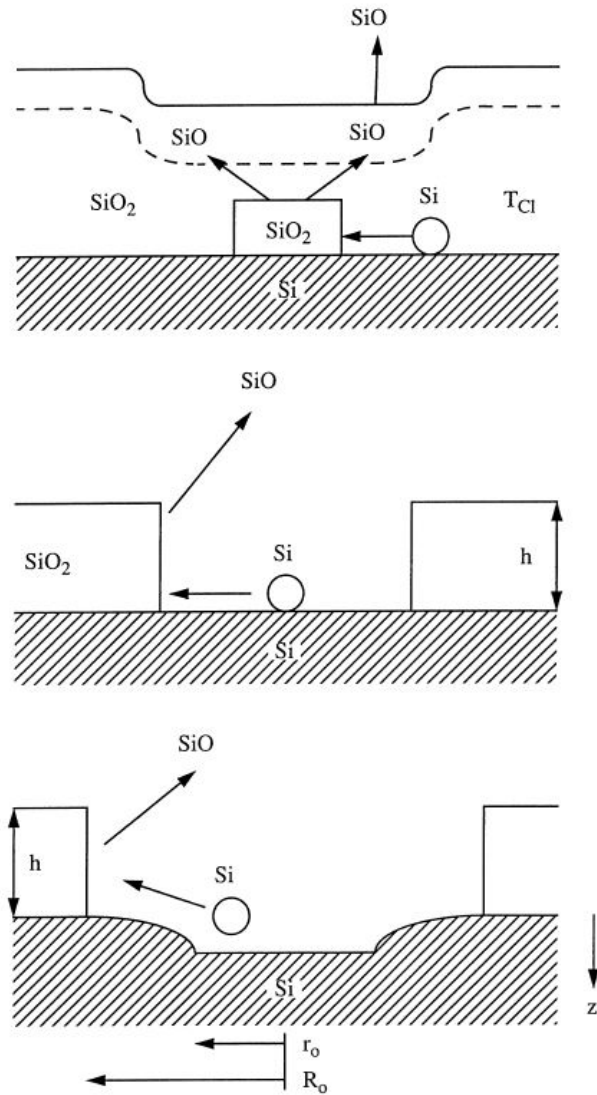
Figure 5.2: Two-step model for Si oxide desorption. Adapted from [198].

in the oxide layer while the latter creates a controlled oxide film on the surface, capturing residual impurities without adding external contaminants. By repeating the process several times, and because O diffuses into Si to create the oxide, the interface moves deeper into the substrate where impurities have not been previously exposed to cleaning. This allows the removal of contaminants that could be buried in the superficial layers of the wafer. It

was shown that two cycles are enough to obtain high-quality surfaces with a superficial layer left by HF thin enough to desorb easily once in the growth system.

In this work, after two cycles of HF dip and O_2 plasma were realized on the samples, the substrates were dipped in HF one last time in order to passivate the surface. From there, they were loaded into the MBE system within 10 min using plastic tweezers. During the entire substrate preparation, the Si samples were only manipulated with dedicated containers and tweezers to avoid cross-contamination.

Thermal treatment

Once transferred to the growth module, the substrates required a higher temperature for thermal cleaning, which could not be monitored accurately with the tools available in the system. Instead, the improvement in the sharpness of the RHEED pattern and the increase in the residual gas partial pressure of C on the quadrupole mass spectrometer (QMS) served as indicators of the passivation layer desorption. Si substrates were heated according to the following protocol:

1. Heat to 800 °C at 3 %/min (power)

2. When the substrate reaches 800 °C, cool immediately back down to 450°C at 3%/ min (power) and let the thermocouple stabilize

Madiomanana *et al.* [199] showed that a short annealing at 800°C formed smooth surfaces with a sharp streaky RHEED pattern. Long anneal times, on the other hand, led to a re-contamination of the surface with contaminants emanating from the hot sources enclosed in the system (cells).

Nucleation steps

After thermal cleaning, the substrate temperature was lowered to 450°C and left to stabilize. First, 4 ML $AlSb$ were grown at 0.35 ML/s, followed by a 50-nm $GaSb$ cap at 1 ML/s. Then, the Ga shutter was closed and the substrate temperature raised to 480°C

under Sb overpressure. For the second part of the epitaxy, a 1000-nm $GaSb$ buffer was grown at $480°C$. At the end of this buffer, the RHEED pattern displayed sharp streaks indicative of a smooth surface.

5.2.2 Solar cell epitaxy

Procedure
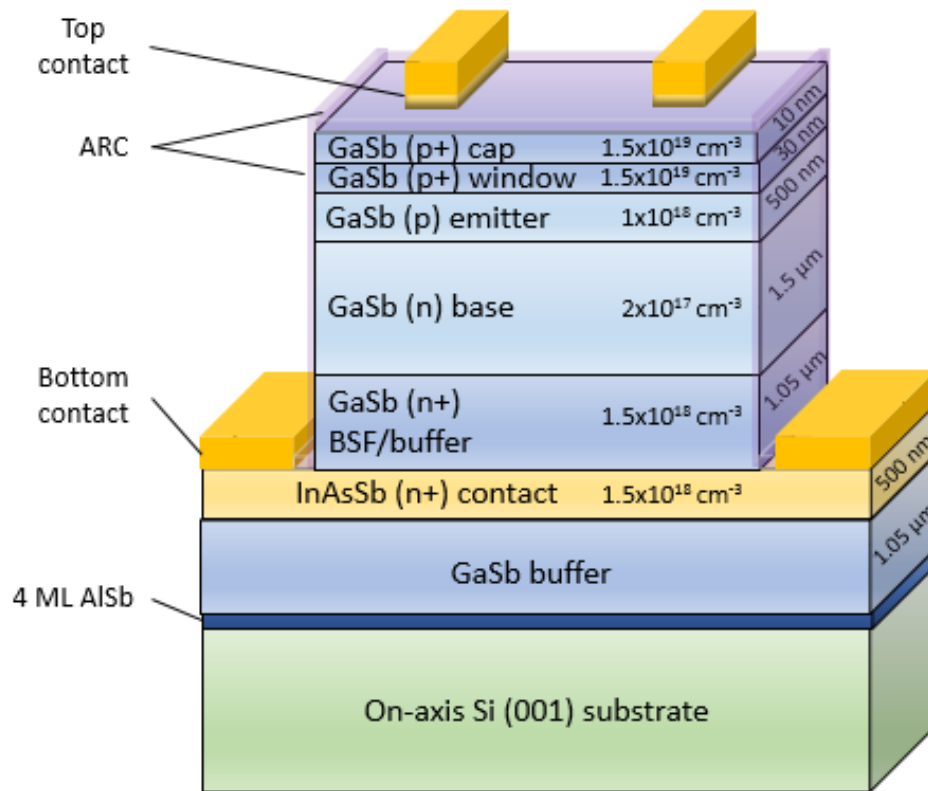
Figure 5.3: Schematic structure of the $GaSb$-on-Si solar cell.

The solar cell structure was grown on top of the buffer as shown in Figure 5.3. A 500-nm $InAs_{0.91}Sb_{0.09}$ contact layer was grown at $430°C$ to serve as the bottom contact and capped with 50 nm of $GaSb$. This alloy composition, lattice-matched to $GaSb$, will

simply be referred to as $InAsSb$ below. The temperature was then raised back to $480°C$ for the remainder of the growth, consisting of a 1000-nm BSF, a 1500-nm base, a 500-nm emitter, a 30-nm window and a 10-nm cap/contact layer. Once again, Be and Te were used for p- and n-type doping, respectively. The $InAsSb$ growth rate was 0.31 ML/s.

Material characterization

The surface was monitored during growth with RHEED. The crystalline quality was also assessed with XRD and AFM prior to processing. The $\omega - 2\theta$ scan is shown in Figure 5.4 on which the Si, $GaSb$ and $InAsSb$ peaks can clearly be identified. The position of the $GaSb$ peak corresponds to a 101% relaxed $GaSb$ layer. This extra 1% is likely due to the thermal stress undergone by the material upon cooling. It can be noted that the $InAsSb$ is not exactly lattice-matched to $GaSb$. A rocking curve of the sample was also measured, which allowed us to estimate the $GaSb$ FWHM at 295 $arcsec$, close to the values mentioned in the literature review. The measured value is very similar to the best ones reported in [170] and around $100 - 200$ $arcsec$ higher than the ones reported for Ge-on-Si [89] and $GaAs$-on-Si [90]. Last, the morphology of the sample was assessed with AFM (Figure 5.5). The RMS roughness was evaluated at 2 nm (size of the scan: 10 μm × 10 μm), again close to the values mentioned in the literature (in the lower range of [170], still above the < 1 nm of [89]). As a baseline for comparison, according to our own measurements on such samples, the typical value of RMS roughness for a homoepitaxial $GaSb$-on-$GaSb$ structure is in the 0.1-nm (sub-monolayer) range. The rougher morphology observed is expected because of the increased mismatch and because the substrate used in this work was an on-axis sample. As mentioned previously, on-axis substrates generate APDs and APBs. APDs exhibit dissimilar growth rates, leading to rougher surfaces.

5.2.3 Solar cell processing: the front-front contact configuration

The fabrication procedure had to be adapted to circumvent the high defect density at the Si/III-Sb interface. Keeping the back of the substrate as a bottom contact would indeed induce many electric losses via the hetero-interface. We therefore decided to bring
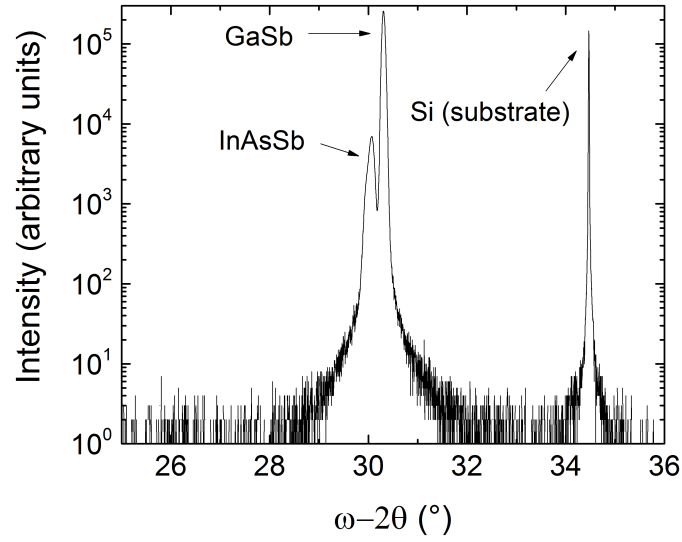
Figure 5.4: $\omega - 2\theta$ XRD scan of the $GaSb$-on-Si solar cell.
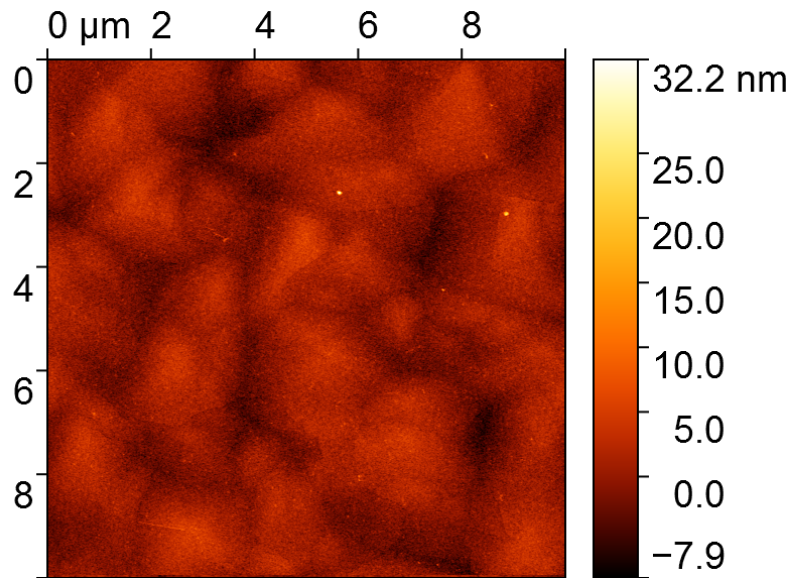
Figure 5.5: AFM 10 μm × 10 μm scan of the $GaSb$-on-Si sample prior to processing. The estimated RMS roughness is 2 nm.

both contacts to the front of the sample, leaving one at the very top of the solar cell and setting the other one at its base, as shown in Figure 5.3. The new process flow (shown in Figure 5.6) comprised three steps, namely mesa etching, surface and side passivation, and metallization (Ti/Au 30/250 nm, top and bottom simultaneously).

It was decided here to proceed first to passivation and then to contact deposition to avoid any metal from depositing on the sides of the solar cells, leading to electrical short. At the end of processing, the samples were cleaved into individual cells and mounted on TO-8 holders with silver paint. The solar cell bus bars and bottom contacts were connected
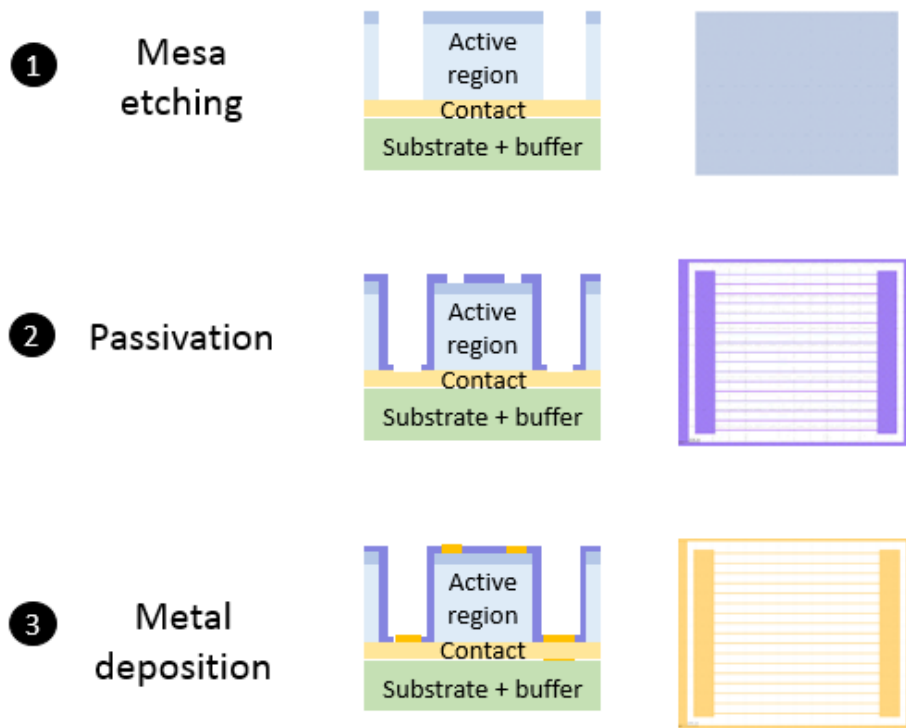
Figure 5.6: Schematic illustration of the processing steps for the fabrication of the $GaSb$-on-Si solar cell. For each step, a picture of the corresponding photolithography mask is displayed (right).

114

to the TO-8 pins by micro-welding.

The resulting cell is shown in Figure 5.7.
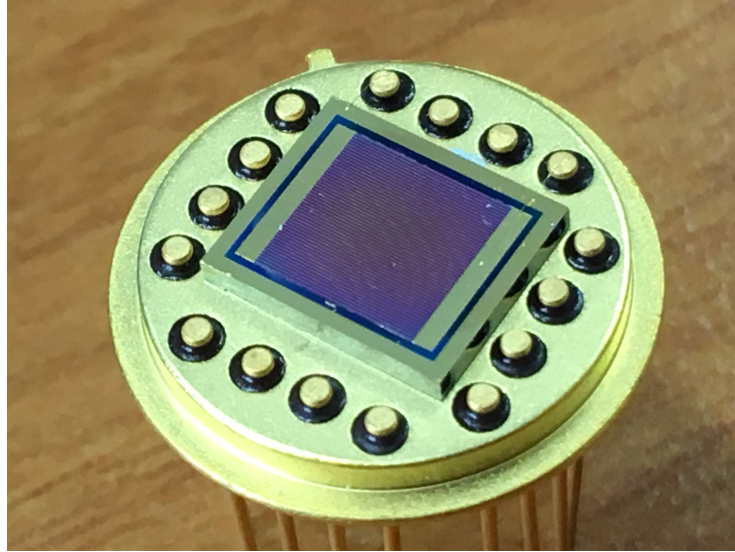
Figure 5.7: Fabricated $GaSb$-on-Si solar cell.

5.3 Device characterization

5.3.1 Electrical characterization

Figure 5.8 compares the J-V curves of the control and the best fabricated hybrid solar cell. The best fabricated hybrid cell showed a significantly reduced 1-sun efficiency of 0.60% with 80 mV V_{OC}, 23 mA/cm^2 J_{SC} and 31.3% FF. The extremely low value of the FF and V_{OC} reflects the high non-radiative recombination rate. Nevertheless, these parameters are close to the recently reported progress on $GaSb$-on-$GaAs$ cells. In particular, the measured J_{SC} and FF are between the values reported in [65] and [115]. Both references used front-back contact configurations. The front-front contact configuration used in this work circumvents the highest defect density zone, $i.e.$, the III-Sb/Si interface. It seems that this partially compensated for the much larger lattice mismatch ($\sim 12\%$ vs $\sim 8\%$
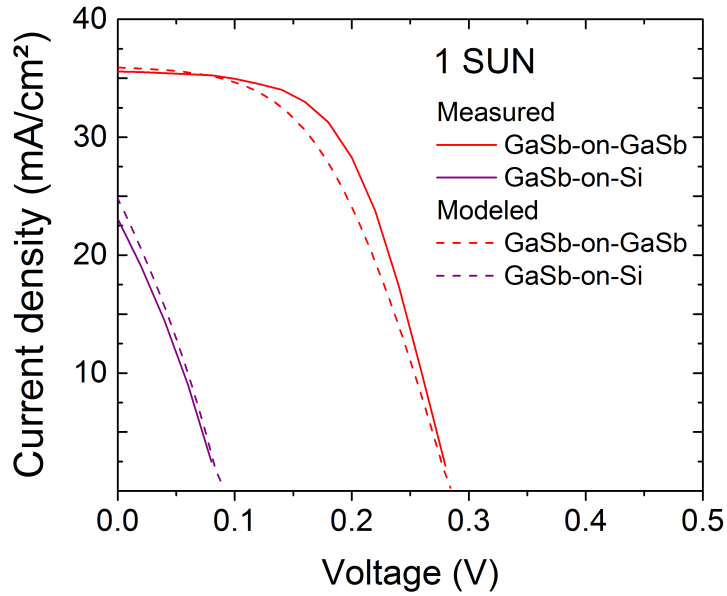
(a)
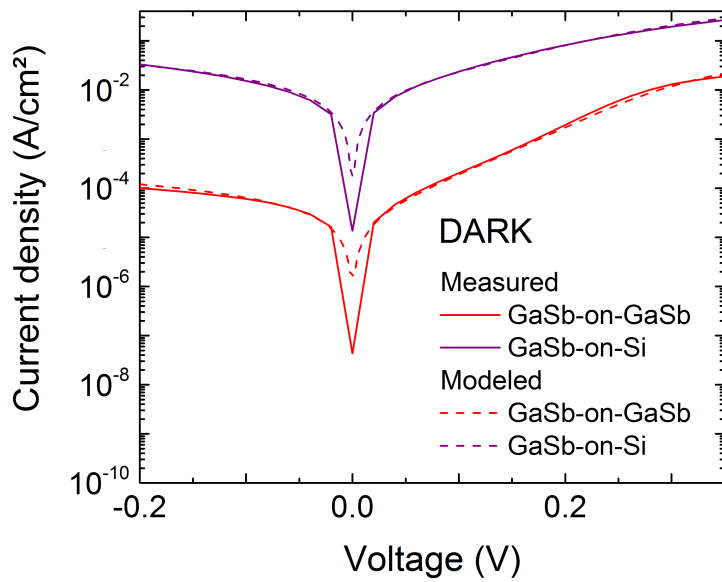
(b)

Figure 5.8: Measured (solid lines) and modeled (dashed lines) 1-sun (a) and dark current (b) J-V curves for the *GaSb*-on-*GaSb* control solar cell (red) and *GaSb*-on-*Si* hybrid solar cell (purple).

in the case of *GaSb*-on-*GaAs* cells). The use of a thicker buffer (two or more times as thick as the ones used in [65] and [115]) also likely contributed to the lattice mismatch compensation. However, the V_{OC} is lower in both cases, suggesting a still higher TDD in the active zone.

5.3.2 Comparison with stand-alone GaSb solar cells

To gain a deeper understanding, the dark and 1-sun J-V curves of the control and hybrid solar cells were compared, as shown in Figure 5.8. To do so, we used an in-house MATLAB code solving the coupled semiconductor equations (Poisson and continuity equations) in one dimension to fit the experimental curves. The optical generation was calculated with a transfer-matrix-based method, involving optical properties (n,k) taken from the literature (*GaSb*: [200]) or from experimental ellipsometry measurements ($SiN_x : H$). The bandgap and effective density values were taken from the literature [65] [201]. The mobility values were taken from measurements made during the doping calibration stage, fitted to a simple impurity-dependent model [202]. The parameters extracted from these simulations are listed in Table 5.2. They are valid for dark and 1-sun J-V data, along with QE data. The measured and modeled J-V curves are presented in Figure 5.8. They are in satisfactory agreement, both for the control *GaSb*-on-*GaSb* and the hybrid *GaSb*-on-*Si* solar cells.

The significantly reduced values of the effective minority carrier lifetime in the hybrid solar cell reflect the poorer material quality. The degraded value of the shunt resistance of the hybrid cell further reveals a higher number of short circuit paths. This corroborates the aforementioned material characterizations, as both the density of APDs [203] and the TDD (in the case of dislocations crossing the space-charge region) [204] directly impact the value of the shunt resistance. Last, the hybrid solar cell curve is largely dominated by shunt resistance, making the estimation of the series resistance difficult to provide. We nevertheless suggest that the improvement in the series resistance (4.0×10^{-1} Ω cm^2) compared with that of the control cell (2.0 Ω cm^2) can be correlated with the benefit of using an *InAsSb* contact layer. Overall, the resistance values estimated with this analysis are in good agreement with previous results on thermophotovoltaic *GaSb*-on-*GaAs* cells [205], despite the increased lattice mismatch.

Table 5.2: Parameters used for the *GaSb* cells simulation.

Parameter	Value
Bandgap, E_G	$0.726\ eV$
Effective density of states in the conduction band, $N_{C,eff}$	$2.1 \times 10^{17}\ cm^{-3}$
Effective density of states in the valence band, $N_{V,eff}$	$1.8 \times 10^{19}\ cm^{-3}$
Electron lifetime, $\tau_{n,eff}$ *GaSb*-on-*GaSb* fit	$0.4\ ns$
Electron lifetime, $\tau_{n,eff}$ *GaSb*-on-*Si* fit	$0.02\ ns$
Hole lifetime, $\tau_{p,eff}$ *GaSb*-on-*GaSb* fit	$24\ ns$
Hole lifetime, $\tau_{p,eff}$ *GaSb*-on-*Si* fit	$0.15\ ns$
Shunt resistance, R_{sh} *GaSb*-on-*GaSb* fit	$2.0 \times 10^{3}\ \Omega\ cm^{2}$
Shunt resistance, R_{sh} *GaSb*-on-*Si* fit	$6.7\ \Omega\ cm^{2}$
Series resistance, R_s *GaSb*-on-*GaSb* fit	$2.0\ \Omega\ cm^{2}$
Series resistance, R_s *GaSb*-on-*Si* fit	$4.0 \times 10^{-1}\ \Omega\ cm^{2}$

5.3.3   Quantum efficiency

Measured and modeled QEs of both solar cells are presented in Figure 5.9. The hybrid *GaSb*-on-*Si* solar cell EQE is significantly lower (around 30%) than the control *GaSb*-on-*GaSb* solar cell EQE. This result is consistent with a reduced effective minority carrier lifetime in the emitter and base. The one-dimensional simulation does not allow dissociating bulk from surface recombination, as it does not take into account surface recombination occurring at the mesa sidewalls. However, since the structure (thicknesses, doping) and passivation of the two cells are similar, we can consider their surface recombination velocities to be equivalent. The much poorer effective carrier lifetimes estimated in the hybrid cell (one or two orders of magnitude lower) can consequently be attributed to a higher volumetric non-radiative recombination rate. This would imply that the degradation of the hybrid cell performance dominantly stems from losses in the bulk, likely induced by the elevated TDD.
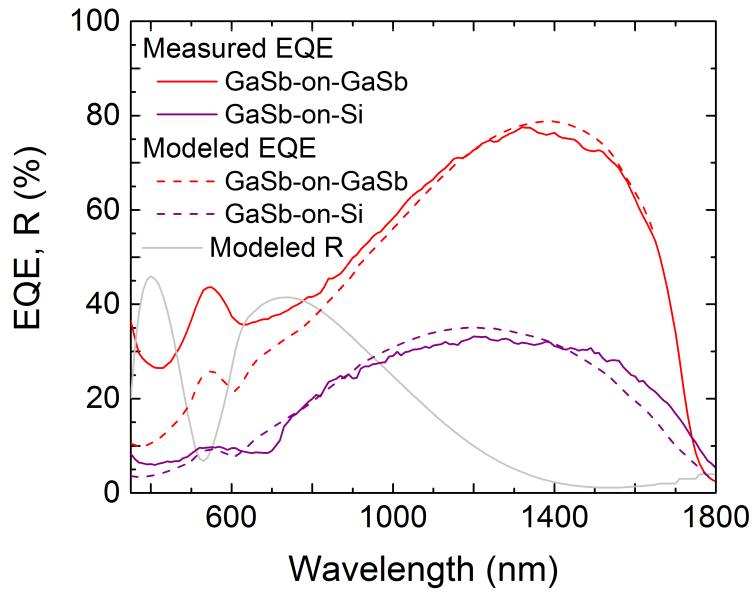
(a)
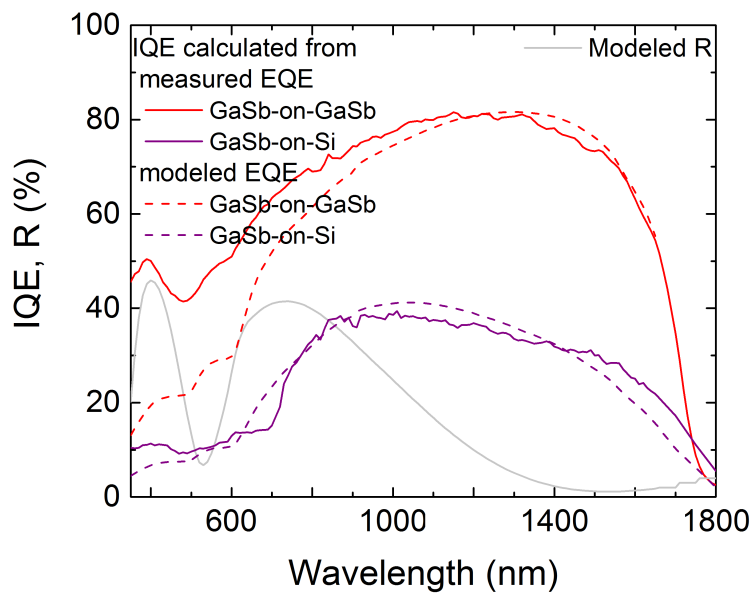
(b)

Figure 5.9: Measured (solid lines) and modeled (dashed lines) EQE (a) and IQE (b) curves for the *GaSb*-on-*GaSb* control solar cell (red) and the *GaSb*-on-*Si* hybrid solar cell (purple). The reflectance is also plotted in gray.

5.3.4 Avenues of research

Using a simple model by Yamaguchi *et al.*, we can approximate the minimum TDD at the bottom of the hybrid solar cell by $\frac{4}{\pi^3 L_p^2}$, where L_p is the minority carrier diffusion length [206]. With $L_p = 2.41 \times 10^{-5}$ cm estimated by our simulation, we compute a minimum TDD in the 2×10^8 cm^{-2} range, higher than in the case of [206]. This value is still far from the target. Other works, mentioned in the literature review, have employed much thicker buffer layers ($10 - 15$ μm *vs* 1 μm used in this work) to achieve TDDs in the 10^6 cm^{-2} range. One avenue of research would thus be to increase the $GaSb$ buffer thickness below the $InAsSb$ contact layer to move the active region further away from the high defect density region. At this point, we are not considering the SLS and TCA techniques, for the sake of simplicity.

Another avenue of research is the comparison between the front-back and front-front contact configurations for the hybrid solar cell. As explained previously, we used the front-front configuration here to circumvent the high-defect-density region at the hetero-interface and suppress associated losses. However, by doing so, and because the cells are 5 mm wide, we require that the carrier diffusion length is superior to 2.5 mm to enable total collection. According to the above calculus, this is far from being the case. It is therefore possible that the hybrid solar cell performs better with a front-back configuration, in spite of having a high-defect-density region within its active zone.

5.4 Summary and proposition of an improved structure

In this chapter, we focus on the integration of a $GaSb$ solar cell on Si. First, we explain the challenges of this integration and detail the available techniques for III-Sb materials. Then, we present the adapted fabrication procedure, which circumvents the high defect density region at the hetero-interface. Although the electrical performance of the hybrid cell is – as expected – drastically reduced compared with the stand-alone $GaSb$ cell, the results are close to those obtained for $GaSb$-on-$GaAs$ solar cells, despite a much larger lattice

mismatch. We further discuss possible improvements to both the growth (buffer thickness) and process flow (front-back contact configuration). We thus suggest the improved hybrid structure displayed in Figure 5.10.
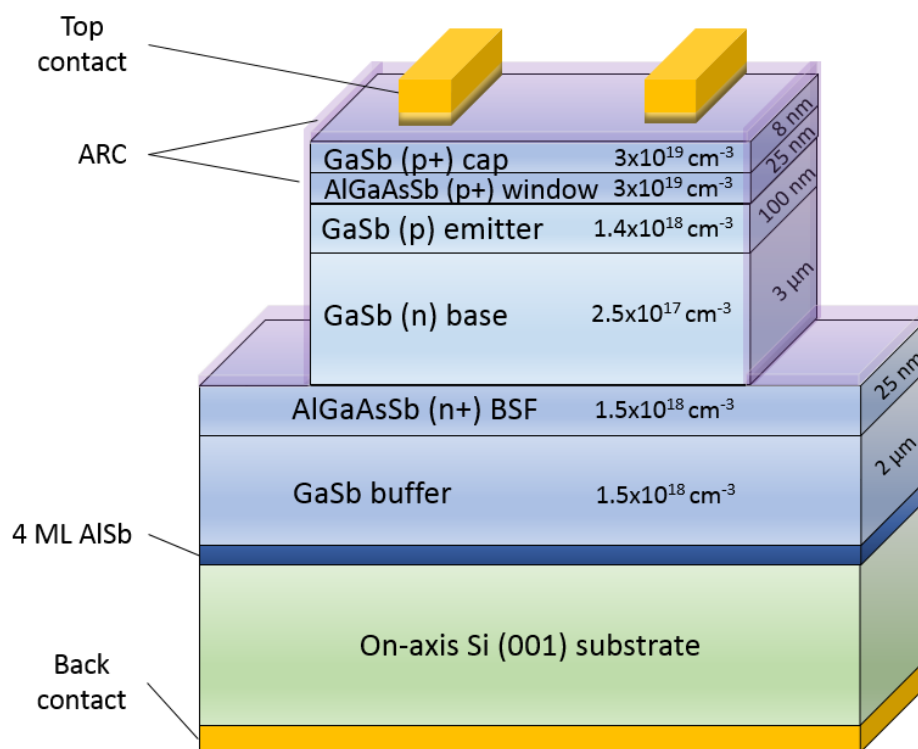
Figure 5.10: Schematic structure of the improved $GaSb$-on-Si solar cell.

Chapter 6

Conclusion and future outlook

It is clear today that PV energy is a key resource for our future. From this perspective, the research focus has been on developing of high-efficiency solar cells and integrating them on inexpensive substrates. MJ structures based on III-V semiconductors were elaborated to provide high-performance solar cells. These architectures involve a variety of fabrication techniques. We identified the all lattice-matched architecture as the best way to achieve greater efficiency without adding significantly to the complexity and cost of the system. We further proposed III-Sb materials as a basis for a high-efficiency and low-cost solar cell. The goal of this thesis was to demonstrate the advantages of the 6.1 $\mathring{A}$ materials system for MJ design and its integrability on a Si substrate.

6.1 Key accomplishments

In order to assess the potential of III-Sb materials for PV applications, we studied several aspects of the materials.

- We fabricated a $GaSb$ stand-alone solar cell whose performance is close to the best reported in the literature. This cell served as a control cell for the subsequent developments.

122

- We identified potential structures for all lattice-matched $GaSb$-based MJ solar cells. In particular, we studied the $AlInAsSb$ alloy, whose growth remains challenging and whose electronic properties remain uncertain. The resulting cell exhibited an efficiency lower than expected but constitutes a proof of concept for all lattice-matched $GaSb$-based MJ solar cells.

- We demonstrated the first monolithic integration of a $GaSb$ solar cell onto Si, taking advantage of the formation of an IMF at the III-V/Si interface. Although the cell's performance was drastically reduced compared with that of the homoepitaxial cell, we achieved results close to the latest progress made on $GaSb$-on-$GaAs$, despite the much larger lattice mismatch.

This exploratory work lays the foundation for an all lattice-matched $GaSb$-based MJ solar cell monolithically integrated onto Si. Each one of the research directions presented above, *i.e.*, the cell structure, the development of novel materials, and the heteroepitaxy is thus a building block toward the development of high-efficiency and low-cost solar cells.

6.2   Conclusion

The various aspects of III-Sb materials studied in this work let us conclude on their potential for PV applications. A basis $GaSb$ solar cell was obtained with reasonable quality using standard growth and processing techniques. We further proposed $AlInAsSb$ as the cornerstone of 6.1 $\mathring{A}$ MJ solar cells. We demonstrated that the alloy was able to attain a wide range of bandgap energies, although its electronic properties diverged from their theoretical estimations. Combined with a low-loss $GaSb/InAs$ TJ, it should facilitate the targeting of high efficiencies. Our first attempt at a tandem $AlInAsSb/GaSb$ cell did not show significant improvement over the SJ $GaSb$ cell. Nevertheless, it demonstrated its feasibility and pointed to the still insufficient quality of the alloy. Last, we showed that the $GaSb$ cell could be integrated onto Si by adapting the growth and processing techniques. Although the hybrid cell demonstrated significantly reduced performance, it is notable that it achieved results close to that of $GaSb$-on-$GaAs$ cells despite a much larger mismatch. This result is encouraging for the monolithic integration of III-V solar cells on Si.

The $AlInAsSb$ alloy ([46][137] [143]) and III-Sb growth on Si ([169] [170] [187] [188]) have both regained attention over the past years, leading us to conclude that the III-Sb materials system has potential for the development of high-efficiency, low-cost solar cells.

6.3   Prospects of future research

Paths of improvement were identified for each research axis in this project.

Optimization of the cell structure, notably the window layers, is the first applicable step. This work is currently being pursued in collaboration with the M@csee team of IES. It consists of simulating the proposed structures with different doping and thicknesses in order to identify their optimal combination. An in-house TCAD solver and the SCAPS software are used for these simulations. Also, contact resistivities have not been investigated in this work but would enhance cell performances. Last, a detailed study of surface passivation is required: double-layer ARCs could be considered and the uniformity of the mesa passivation should be verified.

For the MJ cells, it is fundamental to first improve the quaternary alloy quality. During our epitaxy attempts, we observed that the alloy composition was very sensitive to temperature. A good research direction would thus be to adapt the growth technique to ensure temperature uniformity through the wafer and over time. The incorporation of As, whose background level is known to increase over a long growth, has also to be monitored and counterbalanced to ensure more homogeneous layers. Post-growth treatments could be investigated in greater detail to bring the quaternary bandgap energy closer to the ideal. Once sufficient progress has been made on the material side, the cell design could be improved with simulations adapted to the observed electronic properties. A study of p-type metallic contacts to $AlInAsSb$ would also be of interest, along with changes in the passivation layer.

Concerning the integration onto Si, we intend to first change the mask configuration to switch back to a front-back metallization. There is indeed a compromise needed between circumventing the defects at the III-V/Si interface and enhancing carrier collection with a thicker cell. Preliminary study on metallic contacts to n-type Si would be required. Once

the optimal contact configuration is determined, changes in the buffer structure could be implemented. Further work includes improvements to the substrate preparation and nucleation sequence.

6.4 Scope and future outlook

$GaSb$-based all lattice-matched structures have been proposed in other works in the quest for high-efficiency solar cells [207] [66]. Lim *et al.* in particular proposed to complement III-Sb subcells with $ZnCdSeTe$ alloys to overcome bandgap energy limitations [207]. These alloys, lattice-matched to $GaSb$, could also be used in the TJs to minimize absorption. To our knowledge, however, an all lattice-matched MJ to the lattice parameter of $GaSb$ has not yet been demonstrated. The $AlInAsSb$ alloy that we investigated is also of interest for InP all lattice-matched MJ solar cells [124]. Combined efforts to enhance the alloy quality should help in developing these promising PV devices in the near future. There is also good hope that III-Sb solar cells could be integrated onto Si with the same quality as other hybrid devices ([81] [82] [83] [84]). Such developments would help to reduce the cost of PV systems, making them more competitive than other energy sources.

APPENDICES

PROMIS

Solar cell on GaSb – L1, L2, L4, L5

Cellule GaSb/GaSb :

Cap – GaSb(p) @1.5E19 – 10nm
Window – GaSb(p) @1.5E19 – 30nm
Emitter – GaSb(p) @1E18 – 500nm
Base – GaSb(n) @2E17 – 1500nm
BSF/Buffer – GaSb(n) @1.5E18 – 500nm
Substrat – GaSb(n)

Julie Tournet / Stefano Soresi / Roland Teissier / Eric Tournié

Alignment marks

	#	Step	Operation	Equipment	Date	Remarks
				Photolithography		
☐	1	Photomask L1.1 cleaning	(Acetone + Ethanol + IPA + DI water)	Ultrasonic bath		
☐	2	Surface cleaning	(Acetone + Ethanol + IPA)	Solvent hood		
☐	3	Photoresist application	Dehydration	Hot plate		
			Spincasting	Spin coater		
			Prebake	Hot plate		
☐	4	Mask L1.1 exposure	Exposure	MJB4		Soft contact
☐	5	Post exposure bake	Anneal	Hot plate		Do not forget !
☐	6	Developing	Developer	Developing hood		Etching rate GaSb 3 nm/min
☐	7	Rinsing	DI water	Developing hood		
☐	8	Photomask L1.1 cleaning	(Acetone + Ethanol + IPA + DI water)	Ultrasonic bath		
☐	9	Photoresist application verification		Optical microscope		Take image - **Observe the undercut profile**
☐	10	Photoresist thickness verification		Profilometer DEKTAK		

Comments:

	#	Step	Operation	Equipment	Date	Remarks
☐	1	Marks etching	Recipe GaSb slow	RIE ICP		Etching rate GaSb : 365-370 nm/min

Marks etching

Comments:
Careful to cover the whole back with oil to avoid heating and polymerization during RIE.
Careful to remove the oil without contaminating the front surface afterwards.

	#	Step	Operation	Equipment	Date	Remarks
☐	2	Photoresist removal	(Acetone + Ethanol + IPA)	Solvent hood		
			Plasma Ar:O$_2$	Plasma Nanomir		
☐	3	Mesa etching verification		Optical microscope		Take image

Comments:

Front side metallization (p)

	#	Step	Operation	Equipment	Date	Remarks
			Photolithography			
☐	1	Photomask L2 cleaning	(Acetone + Ethanol + IPA + DI water)	Ultrasonic bath		
☐	2	Surface cleaning	(Acetone + Ethanol + IPA)	Solvent hood		
☐	3	Photoresist application	Dehydration	Hot plate		
			Spincasting	Spin coater		
			Prebake	Hot plate		
☐	4	Mask L2 exposure	Exposure	MJB4		Soft contact
☐	5	Post exposure bake	Anneal	Hot plate		Do not forget !
☐	6	Developing	Developer	Developing hood		Etching rate GaSb 3 nm/min
☐	7	Rinsing	DI water	Developing hood		
☐	8	Photomask L2 cleaning	(Acetone + Ethanol + IPA + DI water)	Ultrasonic bath		
☐	9	Photoresist application verification		Optical microscope		Take image - **Observe the undercut profile**
☐	10	Photoresist thickness verification		Profilometer DEKTAK		

Comments:

	#	Step	Operation	Equipment	Date	Remarks
		Metallization p				
☐	1	Oxide removal	HCl : H_2O	Acid hood		
☐	2	Ti/Au deposition		Evaporation		Without rotation

Comments:

	#	Step	Operation	Equipment	Date	Remarks
		Lift-off				
☐	1	Lift-off	Acetone (dip+wash bottle+syringe if needed)	Solvent hood		
☐	2	Rinsing	Ethanol + IPA	Solvent hood		Careful to redeposition
☐	3	Lift-off verification		Optical microscope		Take image

Comments:

☐	4	Photoresist leftovers removal	Plasma Ar:O$_2$	Plasma Nanomir		
☐	5	Photoresist removal verification		Optical microscope		Take image
☐	6	Contacts thickness verification		Profilometer DEKTAK		

Comments:

We do not use a RTA afterwards to avoid damaging the GaSb. To investigate once we have satisfying results.

Mesas etching

	#	Step	Operation	Equipment	Date	Remarks
			Photolithography			
☐	1	Photomask L4 cleaning	(Acetone + Ethanol + IPA + DI water)	Ultrasonic bath		
☐	2	Surface cleaning	(Acetone + Ethanol + IPA)	Solvent hood		
☐	3	Photoresist application	Dehydration	Hot plate		
			Spincasting	Spin coater		
			Prebake	Hot plate		
☐	4	Mask L4 exposure	Exposure	MJB4		Soft contact
☐	5	Developing	Developer	Developing hood		Etching rate GaSb 3 nm/min
☐	6	Rinsing	DI water	Developing hood		
☐	7	Photomask L4 cleaning	(Acetone + Ethanol + IPA + DI water)	Ultrasonic bath		
☐	8	Photoresist application verification		Optical microscope		Take image
☐	9	Photoresist thickness verification		Profilometer DEKTAK		

Comments:

	#	Step	Operation	Equipment	Date	Remarks
☐	1	Mesa etching	Recipe GaSb slow	RIE ICP		Etching rate GaSb : 365-370 nm/min
☐	2	Mesa etching verification		Optical microscope		Take image
☐	3	Mesa depth verification		Profilometer DEKTAK		

Mesa etching

Comments:
Careful to cover the whole back with oil to avoid heating and polymerization during RIE.
Careful to remove the oil without contaminating the front surface afterwards.

	#	Step	Operation	Equipment	Date	Remarks
☐	4	Photoresist removal	(Acetone + Ethanol + IPA)	Solvent hood		
			Plasma Ar:O_2	Plasma Nanomir		
☐	5	Mesa etching verification		Optical microscope		Take image
☐	6	Mesa depth verification		Profilometer DEKTAK		

Comments:

ARC deposition

	#	Step	Operation	Equipment	Date	Remarks
		Dielectric deposition				
☐	~~1~~	~~Oxide removal~~	~~HCl:H$_2$O~~	~~Acid hood~~		
☐	2	ARC deposition		PECVD		Deposition rate : ~ 170 nm/min

Comments:

	#	Step	Operation	Equipment	Date	Remarks
		Photolithography				
☐	1	Photomask L5 cleaning	(Acetone + Ethanol + IPA + DI water)	Ultrasonic bath		
☐	2	Photoresist application	Dehydration	Hot plate		
			Spincasting	Spin coater		
			Anneal	Hot plate		
☐	3	Mask L5 exposure	Exposure	MJB4		Soft contact
☐	4	Developing	Developer	Developing hood		Etching rate GaSb 3 nm/min
☐	5	Rinsing	DI water	Developing hood		

	#	Step	Operation	Equipment		
☐	6	Photomask L5 cleaning	(Acetone + Ethanol + IPA + DI water)	Ultrasonic bath		
☐	7	Photoresist application verification		Optical microscope		Take image
☐	8	Photoresist thickness verification		Profilometer DEKTAK		

Comments:

Dielectric etching (opening to contacts)						
	#	Step	Operation	Equipment	Date	Remarks
☐	1	ARC etching	Recipe Atemi SiN	RIE ICP Corial		End point detection
☐	2	ARC etching verification		Optical microscope		Take image
☐	3	ARC thickness verification		Profilometer DEKTAK		

Comments:

☐	4	Photoresist removal	(Acetone + Ethanol + IPA)	Solvent hood		
			Plasma Ar:O_2	Plasma Nanomir		
☐	5	ARC etching verification		Optical microscope		Take image
☐	6	ARC thickness verification		Profilometer DEKTAK		

Comments:

The edges passivation is done.

Back side metallization (n)

	#	Step	Operation	Equipment	Date	Remarks
			Metallization n			
☐	1	Oxide removal	HCl : H_2O	Acid hood		
☐	2	Pd/AuGeNi deposition		Sputtering		

Comments:

Single junction solar cell on Si

Structure des échantillons

Cellule GaSb/Si:

Cap – GaSb(p) @3E19 – 10nm
Window – AlGaAsSb(p) @3+E19 – 25nm
Emitter – GaSb(p) @1.4E18 – 100nm
Base – GaSb(n) @2.5E17 – 3000nm
BSF/Buffer – GaSb(n) @1.5+E18 – 25nm
Buffer – GaSb (n) @1.5E18 – 50 nm
(Contact – InAsSb (n) @4.5E18 – 500 nm)
Buffer – GaSb (n) @1.5E18 – 5000 nm
Buffer – GaSb – 50+500 nm
Nucleation – AlSb – 4 ML
Substrat – GaSb(n)/Si

Alignment marks

	#	Step	Operation	Equipment	Date	Remarks
			Photolithography			
☐	1	Photomask L1.1 cleaning	(Acetone + Ethanol + IPA + DI water)	Ultrasonic bath		
☐	2	Surface cleaning	(Acetone + Ethanol + IPA)	Solvent hood		
☐	3	Photoresist application	Dehydration	Hot plate		
			Spincasting	Spin coater		
			Prebake	Hot plate		
☐	4	Mask L2 exposure	Exposure	MJB4		Soft contact
☐	5	Post exposure bake	Anneal	Hot plate		Do not forget !
☐	6	Developing	Developer	Developing hood		Etching rate GaSb 3 nm/min
☐	7	Rinsing	DI water	Developing hood		
☐	8	Photomask L2 cleaning	(Acetone + Ethanol + IPA + DI water)	Ultrasonic bath		
☐	9	Photoresist application verification		Optical microscope		Take image - **Observe the undercut profile**
☐	10	Photoresist thickness verification		Profilometer DEKTAK		

Comments:

	#	Step	Operation	Equipment	Date	Remarks
☐	1	Marks etching	Recipe GaSb slow	RIE ICP		Etching rate GaSb : 365-370 nm/min

Marks etching

Comments:

	#	Step	Operation	Equipment	Date	Remarks
☐	2	Photoresist removal	(Acetone + Ethanol + IPA)	Solvent hood		
			Plasma Ar:O$_2$	Plasma Nanomir		
☐	3	Mesa etching verification		Optical microscope		Take image

Comments:

Front side metallization (p)

	#	Step	Operation	Equipment	Date	Remarks
		Photolithography				
☐	1	Photomask L2 cleaning	(Acetone + Ethanol + IPA + DI water)	Ultrasonic bath		
☐	2	Surface cleaning	(Acetone + Ethanol + IPA)	Solvent hood		
☐	3	Photoresist application	Dehydration	Hot plate		
			Spincasting	Spin coater		
			Prebake	Hot plate		
☐	4	Mask L2 exposure	Exposure	MJB4		Soft contact
☐	5	Post exposure bake	Anneal	Hot plate		Do not forget !
☐	6	Developing	Developer	Developing hood		Etching rate GaSb 3 nm/min
☐	7	Rinsing	DI water	Developing hood		
☐	8	Photomask L2 cleaning	(Acetone + Ethanol + IPA + DI water)	Ultrasonic bath		
☐	9	Photoresist application verification		Optical microscope		Take image - **Observe the undercut profile**
☐	10	Photoresist thickness verification		Profilometer DEKTAK		

Comments:

	#	Step	Operation	Equipment	Date	Remarks
		Metallization p				
☐	1	Oxide removal	HCl : H_2O	Acid hood		
☐	2	Ti/Au deposition		Evaporation		Without rotation

Comments:

	#	Step	Operation	Equipment	Date	Remarks
		Lift-off				
☐	1	Lift-off	Acetone (dip+wash bottle+syringe if needed)	Solvent hood		**Avoid brush and ultrasons**
☐	2	Rinsing	Ethanol + IPA	Solvent hood		Careful to redeposition
☐	3	Lift-off verification		Optical microscope		Take image

Comments:

			Plasma Ar:O_2	Plasma Nanomir		
☐	4	Photoresist leftovers removal	Plasma Ar:O_2	Plasma Nanomir		
☐	5	Photoresist removal verification		Optical microscope		Take image
☐	6	Contacts thickness verification		Profilometer DEKTAK		

Comments:

We do not use a RTA afterwards to avoid damaging the GaSb. To investigate once we have satisfying results.

Mesas etching

	#	Step	Operation	Equipment	Date	Remarks
☐	1	Photomask L4 cleaning	(Acetone + Ethanol + IPA + DI water)	Ultrasonic bath		
☐	2	Surface cleaning	(Acetone + Ethanol + IPA)	Solvent hood		
☐	3	Photoresist application	Dehydration	Hot plate		1.8 µm
			Spincasting	Spin coater		
			Prebake	Hot plate		
☐	4	Mask L4 exposure	Exposure	MJB4		Soft contact
☐	5	Developing	Developer	Developing hood		Etching rate GaSb 3 nm/min
☐	6	Rinsing	DI water	Developing hood		
☐	7	Photomask L4 cleaning	(Acetone + Ethanol + IPA + DI water)	Ultrasonic bath		
☐	8	Photoresist application verification		Optical microscope		Take image
☐	9	Photoresist thickness verification		Profilometer DEKTAK		

Photolithography

Comments:

	#	Step	Operation	Equipment	Date	Remarks
☐	1	Mesa etching	Recipe GaSb slow	RIE ICP		GaSb etching: 365-370 nm/min **Laser monitoring**
☐	2	Mesa etching verification		Optical microscope		Take image
☐	3	Mesa depth verification		Profilometer DEKTAK		

Comments:

	#	Step	Operation	Equipment	Date	Remarks
☐	4	Photoresist removal	(Acetone + Ethanol + IPA)	Solvent hood		
			Plasma Ar:O_2	Plasma Nanomir		
☐	5	Mesa etching verification		Optical microscope		Take image
☐	6	Mesa depth verification		Profilometer DEKTAK		

Comments:

References

[1] B-C Chung, GF Virshup, and JG Werthen. High-efficiency, one-sun (22.3% at air mass 0; 23.9% at air mass 1.5) monolithic two-junction cascade solar cell grown by metalorganic vapor phase epitaxy. *Applied physics letters*, 52(22):1889–1891, 1988.

[2] RTE, SER, Enedis, and ADEeF. Panorama de l'électricité renouvelable en 2016. http://www.rte-france.com/sites/default/files/panorama_enr20161231.pdf. Accessed: 2017-08-23.

[3] French government. Code de l'énergie, article L100-4. https://www.legifrance.gouv.fr/affichCodeArticle.do?cidTexte=LEGITEXT000023983208&idArticle=LEGIARTI000023985182&dateTexte=&categorieLien=cid. Accessed: 2018-04-16.

[4] R. Perez and M. Perez. A fundamental look at energy reserves for the planet. *The IEA SHC Solar Update*, 50(2), 2009.

[5] A. Rosenthal. A record of NASA space missions since 1958. [http://ntrs.nasa.gov/archive/nasa/casi.ntrs.nasa.gov/19940003358.pdf. Accessed: 2018-09-04.

[6] Fraunhofer Institute for Solar Energy Systems. Photovoltaics report. https://www.ise.fraunhofer.de/content/dam/ise/de/documents/publications/studies/Photovoltaics-Report.pdf. Accessed: 2018-01-08.

[7] M.A. Green, Y. Hishikawa, E.D. Dunlop, D.H. Levi, J. Hohl-Ebinger, and A.W.Y. Ho-Baillie. Solar cell efficiency tables (version 52). *Progress in Photovoltaics*, 26(7), 2018.

[8] W. Shockley and H.J. Queisser. Detailed balance limit of efficiency of p-n junction solar cells. *Journal of applied physics*, 32(3):510–519, 1961.

[9] M. Schachinger. Module price index. https://www.pv-magazine.com/features/investors/module-price-index/. Accessed: 2019-05-13.

[10] Capgemini. World energy markets observatory 2017. https://www.capgemini.com/wp-content/uploads/2017/10/wemo-report-2017.pdf. Accessed: 2018-04-18.

[11] Cour des comptes. Le coût de production de l'électricité nucléaire actualisation 2014. https://www.ccomptes.fr/sites/default/files/EzPublish/20140527_rapport_cout_production_electricite_nucleaire.pdf. Accessed: 2018-04-18.

[12] Lazard. Lazard's levelized cost of energy analysis 2017. https://www.lazard.com/perspective/levelized-cost-of-energy-2017/. Accessed: 2018-04-18.

[13] RTE, SER, Enedis, and ADEeF. Panorama de l'électricité renouvelable au 30 septembre 2017. http://www.rte-france.com/sites/default/files/panorama_09-17-web.pdf. Accessed: 2018-01-28.

[14] A. Polman, M. Knight, E.C. Garnett, B. Ehrler, and W.C. Sinke. Photovoltaic materials: present efficiencies and future challenges. *Science*, 352(6283):aad4424, 2016.

[15] M.P. Lumb, S. Mack, K.J. Schmieder, M. González, M.F. Bennett, D. Scheiman, M. Meitl, B. Fisher, S. Burroughs, K.T. Lee, et al. GaSb-based solar cells for full solar spectrum energy harvesting. *Advanced Energy Materials*, 7(20), 2017.

[16] J.F. Geisz, M.A. Steiner, N. Jain, K.L. Schulte, R.M. France, W.E. McMahon, E.E. Perl, and D.J. Friedman. Building a six-junction inverted metamorphic concentrator solar cell. *IEEE Journal of Photovoltaics*, 2017.

[17] F. Dimroth and S. Kurtz. High-efficiency multijunction solar cells. *MRS bulletin*, 32(3):230–235, 2007.

[18] S.P. Philipps, A.W. Bett, K. Horowitz, and S. Kurtz. Current status of concentrator photovoltaic (CPV) technology. Technical report, NREL (National Renewable Energy Laboratory (NREL), Golden, CO (United States)), 2015.

[19] E.D. Jackson and I. Texas. Proposing increased conversion efficiency by employing stacked, multijunction cells. In *Proceedings of Transactions of the Conference on the Use of Solar Ener-gy. Arizona, USA*, volume 122, 1955.

[20] L.W. James and R.L. Moon. GaAs concentrator solar cell. *Applied Physics Letters*, 26(8):467–470, 1975.

[21] L.M. Fraas and R.C. Knechtli. Design of high-efficiency monolithic stacked multijunction solar cells. In *13th Photovoltaic Specialists Conference*, pages 886–891, 1978.

[22] S.M. Bedair, S.B. Phatak, and J.R. Hauser. Material and device considerations for cascade solar cells. *IEEE Transactions on Electron Devices*, 27(4):822–831, Apr 1980.

[23] J.A. Cacheux. Double heterojunction solar cells, March 4 1980. US Patent 4,191,593.

[24] S.M. Bedair, M.L. Timmons, and M. Simons. *Growth and characterization of cascade solar cells*, pages 408–412. Springer Netherlands, Dordrecht, 1981.

[25] S.P. Tobin, C. Bajgar, S.M. Vernon, L.M. Geoffroy, and C.J. Keavney. A 23.7 efficient one-sun GaAs solar cell. In *19th IEEE Photovoltaic Specialists Conference*, page 1492, 1987.

[26] R.R. King, N.H. Karam, J.H. Ermer, N. Haddad, P. Colter, T. Isshiki, H. Yoon, H.L. Cotal, D.E. Joslin, D.D. Krut, et al. Next-generation, high-efficiency III-V multijunction solar cells. In *Photovoltaic Specialists Conference, 2000. Conference Record of the Twenty-Eighth IEEE*, pages 998–1001. IEEE, 2000.

[27] R.R. King, D.C. Law, K.M. Edmondson, C.M. Fetzer, G.S. Kinsey, H. Yoon, R.A. Sherif, and N.H. Karam. 40% efficient metamorphic GaInP GaInAs Ge multijunction solar cells. *Applied Physics Letters*, 90(18):183516, 2007.

[28] F. Dimroth, T.N.D. Tibbits, M. Niemeyer, F. Predan, P. Beutel, C. Karcher, E. Oliva, G. Siefer, D. Lackner, P. Fuß-Kailuweit, A.W. Bett, R. Krause, C. Drazek, E. Guiot, J. Wasselin, A. Tauzin, and T. Signamarcheix. Four-junction wafer-bonded concentrator solar cells. *IEEE Journal of Photovoltaics*, 6(1):343–349, Jan 2016.

[29] S. Essig, C. Allebé, T. Remo, J.F. Geisz, M.A. Steiner, K. Horowitz, L. Barraud, J.S. Ward, M. Schnabel, A. Descoeudres, et al. Raising the one-sun conversion efficiency of III-V/Si solar cells to 32.8% for two junctions and 35.9% for three junctions. *Nature Energy*, 2(9):17144, 2017.

[30] R. Cariou, J. Benick, F. Feldmann, O. Höhn, H. Hauser, P. Beutel, N. Razek, M. Wimplinger, B. Bläsi, D. Lackner, et al. III-V-on-silicon solar cells reaching 33% photoconversion efficiency in two-terminal configuration. *Nature Energy*, 3(4):326, 2018.

[31] X. Sheng, C.A. Bower, S. Bonafede, J.W. Wilson, B. Fisher, M. Meitl, H. Yuen, S. Wang, L. Shen, A.R. Banks, et al. Printing-based assembly of quadruple-junction four-terminal microscale solar cells and their use in high-efficiency modules. *Nature materials*, 13(6):593–598, 2014.

[32] K. Xiong, H. Mi, T.H. Chang, D. Liu, Z. Xia, M.Y. Wu, X. Yin, S. Gong, W. Zhou, J.C. Shin, et al. AlGaAs/Si dual-junction tandem solar cells by epitaxial lift-off and print-transfer-assisted direct bonding. *Energy Science & Engineering*, 2018.

[33] A. Barnett, D. Kirkpatrick, C. Honsberg, D. Moore, M. Wanlass, K. Emery, R. Schwartz, D. Carlson, S. Bowden, D. Aiken, A. Gray, S. Kurtz, L. Kazmerski, M. Steiner, J. Gray, T. Davenport, R. Buelow, L. Takacs, N. Shatz, J. Bortz, O. Jani, K. Goossen, F. Kiamilev, A. Doolittle, I. Ferguson, B. Unger, G. Schmidt, E. Christensen, and D. Salzman. Very high efficiency solar cell modules. *Progress in Photovoltaics: Research and Applications*, 17(1):75–83, 2009.

[34] M.A. Green, M.J. Keevers, I. Thomas, J.B. Lasich, K. Emery, and R.R. King. 40% efficient sunlight to electricity conversion. *Progress in Photovoltaics: Research and Applications*, 23(6):685–691, 2015.

[35] R.I. Rabady and H. Manasreh. Thicknesses optimization of two-and three-junction photovoltaic cells with matched currents and matched lattice constants. *Solar Energy*, 158:20–27, 2017.

[36] J.M. Olson, S.R. Kurtz, A.E. Kibbler, and P. Faine. A 27.3% efficient $Ga_{0.5}In_{0.5}P$/GaAs tandem solar cell. *Applied Physics Letters*, 56(7):623–625, 1990.

[37] B.M. Kayes, L. Zhang, R. Twist, I.K. Ding, and G.S. Higashi. Flexible thin-film tandem solar cells with 30% efficiency. *IEEE Journal of Photovoltaics*, 4(2):729–733, 2014.

[38] M.A. Steiner, J.F. Geisz, I. Garcia, D.J. Friedman, A. Duda, W.J. Olavarria, M. Young, D. Kuciauskas, and S.R. Kurtz. Effects of internal luminescence and internal optics on V_{OC} and J_{SC} of III-V solar cells. *IEEE Journal of Photovoltaics*, 3(4):1437–1442, 2013.

[39] R.R. King, C.M. Fetzer, P.C. Colter, K.M. Edmondson, D.C. Law, A.P. Stavrides, H. Yoon, G.S. Kinsey, H.L. Cotal, J.H. Ermer, et al. Lattice-matched and metamorphic GaInP/GaInAs/Ge concentrator solar cells. In *Photovoltaic Energy Conversion, 2003. Proceedings of 3rd World Conference on*, volume 1, pages 622–625. IEEE, 2003.

[40] R.R. King, A. Boca, W. Hong, X.Q. Liu, D. Bhusari, D. Larrabee, K.M. Edmondson, D.C. Law, C.M. Fetzer, S. Mesropian, et al. Band-gap-engineered architectures for high-efficiency multijunction concentrator solar cells. In *24th European Photovoltaic Solar Energy Conference and Exhibition, Hamburg, Germany*, volume 21, page 55, 2009.

[41] V. Sabnis, H. Yuen, and M. Wiemer. High-efficiency multijunction solar cells employing dilute nitrides. In *AIP Conference Proceedings*, volume 1477, pages 14–19. AIP, 2012.

[42] D. Lackner, O. Höhn, A.W. Walker, M. Niemeyer, P. Beutel, G. Siefer, M. Schachtner, V. Klinger, E. Oliva, K. Hillerich, et al. Status of four-junction cell development at fraunhofer ISE. In *E3S Web of Conferences*, volume 16, page 03009. EDP Sciences, 2017.

[43] F. Suarez, T. Liu, A. Sukiasyan, J. Lang, E. Pickett, E. Lucow, T. Bilir, S. Chary, R. Roucka, I. Aeby, et al. Advances in dilute nitride multi-junction solar cells for space power applications. In *E3S Web of Conferences*, volume 16, page 03006. EDP Sciences, 2017.

[44] Y. Zhang, Q. Wang, X. Zhang, B. Chen, B. Wu, D. Ma, L. Zhang, and Z. Wang. AlGaInP/Ge double-junction solar cell with Sb incorporation directly used for lattice-matched five-junction solar cell application. *Japanese Journal of Applied Physics*, 56(2):025501, 2017.

[45] M. González, M.P. Lumb, M.K. Yakes, J. Abell, J.G. Tischler, C.G. Bailey, I. Vurgaftman, J.R. Meyer, L.C. Hirst, K.J. Schmieder, et al. Modeling, design and experimental results for high efficiency multi-junction solar cells lattice matched to InP. In *Physics, Simulation, and Photonic Engineering of Photovoltaic Devices III*, volume 8981, page 898117. International Society for Optics and Photonics, 2014.

[46] L.C. Hirst, M.P. Lumb, J. Abell, C.T. Ellis, J.G. Tischler, I. Vurgaftman, J.R. Meyer, R.J. Walters, and M. González. Spatially indirect radiative recombination in In-AlAsSb grown lattice-matched to InP by molecular beam epitaxy. *Journal of Applied Physics*, 117(21):215704, 2015.

[47] M.F. Bennett, M. González, M.P. Lumb, M.K. Yakes, K.J. Schmieder, S. Tomasulo, J. Abell, J.R. Meyer, and R.J. Walters. Development of wet etch processing for $In_xAl_{1-x}As_ySb_{1-y}$ solar cells grown on InP. In *Photovoltaic Specialist Conference (PVSC), 2015 IEEE 42nd*, pages 1–4. IEEE, 2015.

[48] M. Yamaguchi, K.H. Lee, K. Araki, N. Kojima, and Y. Ohshita. Potential and activities of III-V/Si tandem solar cells. *ECS Journal of Solid State Science and Technology*, 5(2):Q68–Q73, 2016.

[49] B.W. Dodson and J.Y. Tsao. Relaxation of strained-layer semiconductor structures via plastic flow. *Applied Physics Letters*, 51(17):1325–1327, 1987.

[50] E.A. Fitzgerald, A.Y. Kim, M.T. Currie, T.A. Langdo, G. Taraschi, and M.T. Bulsara. Dislocation dynamics in relaxed graded composition semiconductors. *Materials Science and Engineering: B*, 67(1):53–61, 1999.

[51] R.M. France, F. Dimroth, T.J. Grassman, and R.R. King. Metamorphic epitaxy for multijunction solar cells. *MRS Bulletin*, 41(3):202–209, 2016.

[52] T. Takamoto, H. Washio, and H. Juso. Application of InGaP/GaAs/InGaAs triple junction solar cells to space use and concentrator photovoltaic. In *Photovoltaic Specialist Conference (PVSC), 2014 IEEE 40th*, pages 0001–0005. IEEE, 2014.

[53] R.M. France, J.F. Geisz, I. García, M.A. Steiner, W.E. McMahon, D.J. Friedman, T.E. Moriarty, C. Osterwald, J.S. Ward, A. Duda, et al. Design flexibility of ultrahigh efficiency four-junction inverted metamorphic solar cells. *IEEE Journal of Photovoltaics*, 6(2):578–583, 2016.

[54] M.A. Green, Y. Hishikawa, W. Warta, E.D. Dunlop, D.H. Levi, J. Hohl-Ebinger, and A.W.H. Ho-Baillie. Solar cell efficiency tables (version 50). *Progress in Photovoltaics: Research and Applications*, 25(7):668–676, 2017.

[55] C.H. Henry. Limiting efficiencies of ideal single and multiple energy gap terrestrial solar cells. *Journal of applied physics*, 51(8):4494–4500, 1980.

[56] A. Marti and G.L. Araújo. Limiting efficiencies for photovoltaic energy conversion in multigap systems. *Solar Energy Materials and Solar Cells*, 43(2):203–222, 1996.

[57] S.P. Bremner, M.Y. Levy, and C. B. Honsberg. Analysis of tandem solar cell efficiencies under AM1.5G spectrum using a rapid flux calculation method. *Progress in photovoltaics: Research and Applications*, 16(3):225–233, 2008.

[58] S.P. Philipps and A.W. Bett. Chapter 4 III-V multi-junction solar cells. In *Advanced concepts in photovoltaics*, pages 87–117. The Royal Society of Chemistry, 2014.

[59] M.S. Leite, R.L. Woo, J.N. Munday, W.D. Hong, S. Mesropian, D.C. Law, and H.A. Atwater. Towards an optimized all lattice-matched InAlAs/InGaAsP/InGaAs

multijunction solar cell with efficiency 50%. *Applied Physics Letters*, 102(3):033901, 2013.

[60] S. Soresi, G. Hamon, A. Larrue, J. Alvarez, M.P. Pires, and J. Decobert. InP:S/AlInAs:C tunnel junction grown by MOVPE for photovoltaic applications. *physica status solidi (a)*, 215(8):1700427, 2018.

[61] S. Adachi. *Energy-band structure: energy band gaps.* 2009.

[62] O. Dier, C. Lauer, and M.C. Amann. n-InAsSb/p-GaSb tunnel junctions with extremely low resistivity. *Electronics Letters*, 42(7):419–420, 2006.

[63] B.M. Kayes, H. Nie, R. Twist, S.G. Spruytte, F. Reinhardt, I.C. Kizilyalli, and G.S. Higashi. 27.6% conversion efficiency, a new record for single-junction solar cells under 1 sun illumination. In *Photovoltaic Specialists Conference (PVSC), 2011 37th IEEE*, pages 000004–000008. IEEE, 2011.

[64] M. Wanlass. Systems and methods for advanced ultra-high-performance InP solar cells. Technical report, National Renewable Energy Lab.(NREL), Golden, CO (United States), 2017.

[65] G.T. Nelson, B.C. Juang, M.A. Slocum, Z.S. Bittner, R.B. Laghumavarapu, D.L. Huffaker, and S.M. Hubbard. GaSb solar cells grown on GaAs via interfacial misfit arrays for use in the III-Sb multi-junction cell. *Applied Physics Letters*, 111(23):231104, 2017.

[66] S. Parola, A. Vauthelin, F. Martinez, J. Tournet, J. El Husseini, J. Kret, E. Quesnel, Y. Rouillard, E. Tournié, and Y. Cuminal. Investigation of antimonide-based semiconductors for high-efficiency multi-junction solar cells. In *2018 IEEE 7th World Conference on Photovoltaic Energy Conversion (WCPEC)(A Joint Conference of 45th IEEE PVSC, 28th PVSEC & 34th EU PVSEC)*, pages 0937–0942. IEEE, 2018.

[67] NREL. Intro to CPV technology, opportunities and challenges. https://www.nrel.gov/docs/fy10osti/46924.pdf. Accessed: 2018-04-18.

154

[68] National Renewable Energy Laboratory. Best research-cell efficiencies chart. https://www.nrel.gov/pv/assets/images/efficiency-chart.png. Accessed: 2018-03-09.

[69] Soitec. Financial press release of may 21st, 2015. https://www.soitec.com/media/financialreleasedocuments/86/file/soitec_concensolar_pr_21may2015_final_en.pdf. Accessed: 2018-03-02.

[70] K.A.W. Horowitz, M. Woodhouse, H. Lee, and G.P. Smestad. A bottom-up cost analysis of a high-concentration PV module. In *AIP Conference Proceedings*, volume 1679, page 100001. AIP Publishing, 2015.

[71] K. Derendorf, S. Essig, E. Oliva, V. Klinger, T. Roesener, S.P. Philipps, J. Benick, M. Hermle, M. Schachtner, G. Siefer, et al. Fabrication of GaInP/GaAs//Si solar cells by surface activated direct wafer bonding. *IEEE Journal of Photovoltaics*, 3(4):1423–1428, 2013.

[72] J. Yang, Z. Peng, D. Cheong, and R. Kleiman. Fabrication of high-efficiency III-V on silicon multijunction solar cells by direct metal interconnect. *IEEE Journal of Photovoltaics*, 4(4):1149–1155, 2014.

[73] S.M. Vernon, S.P. Tobin, V.E. Haven, C. Bajgar, T.M. Dixon, M.M. Al-Jassim, R.K. Ahrenkiel, and K.A. Emery. Efficiency improvements in GaAs-on-Si solar cells. In *Proc. of 20th IEEE Photovoltaic Specialists Conference*, pages 481–485, 1988.

[74] S.M. Vernon, S.P. Tobin, V.E. Haven, L.M. Geoffroy, and M.M. Sanfacon. High-efficiency concentrator cells from GaAs on Si. In *Photovoltaic Specialists Conference, 1991., Conference Record of the Twenty Second IEEE*, pages 353–357. IEEE, 1991.

[75] Y. Ohmachi, Y. Kadota, Y. Watanabe, and H. Okamoto. High quality GaAs on Si and its application to a solar cell. *MRS Online Proceedings Library Archive*, 144, 1988.

[76] C.L. Andre, J.A. Carlin, J.J. Boeckl, D.M. Wilt, M.A. Smith, A.J. Pitera, M.L. Lee, E.A. Fitzgerald, and S.A. Ringel. Investigations of high-performance GaAs solar

155

cells grown on Ge-Si$_{1-x}$Ge$_x$-Si substrates. *IEEE Transactions on Electron Devices*, 52(6):1055–1060, 2005.

[77] C.L. Andre, D.M. Wilt, A.J. Pitera, M.L. Lee, E.A. Fitzgerald, and S.A. Ringel. Impact of dislocation densities on n+/p and p+/n junction GaAs diodes and solar cells on SiGe virtual substrates. *Journal of applied physics*, 98(1):014502, 2005.

[78] Y. Wang, Z. Ren, M. Thway, K. Lee, S.F. Yoon, I.M. Peters, T. Buonassisi, E.A. Fizgerald, C.S. Tan, and K.H. Lee. Fabrication and characterization of single junction GaAs solar cells on Si with As-doped Ge buffer. *Solar Energy Materials and Solar Cells*, 172:140–144, 2017.

[79] K.N. Yaung, M. Vaisman, J. Lang, and M.L. Lee. GaAsP solar cells on GaP/Si with low threading dislocation density. *Applied Physics Letters*, 109(3):032107, 2016.

[80] M. Vaisman, S. Fan, K. Nay Yaung, E. Perl, D. Martín-Martín, Z.J. Yu, M. Leilaeioun, Z.C. Holman, and M.L. Lee. 15.3%-efficient GaAsP solar cells on GaP/Si templates. *ACS Energy Letters*, 2(8):1911–1918, 2017.

[81] A. Jallipalli, M.N. Kutty, G. Balakrishnan, J. Tatebayashi, N. Nuntawong, S.H. Huang, L.R. Dawson, D.L. Huffaker, Z. Mi, and P. Bhattacharya. 1.54 μm GaSb/Al-GaSb multi-quantum-well monolithic laser at 77 K grown on miscut Si substrate using interfacial misfit arrays. *Electronics Letters*, 43(22):1198–1199, 2007.

[82] K.M. Ko, J.H. Seo, D.E. Kim, S.T. Lee, Y.K. Noh, M.D. Kim, and J.E. Oh. The growth of a low defect InAs HEMT structure on Si by using an AlGaSb buffer layer containing InSb quantum dots for dislocation termination. *Nanotechnology*, 20(22):225201, 2009.

[83] A. Castellano, L. Cerutti, J.B. Rodriguez, G. Narcy, A. Garreau, F. Lelarge, and E. Tournié. Room-temperature continuous-wave operation in the telecom wavelength range of GaSb-based lasers monolithically grown on Si. *APL Photonics*, 2(6):061301, 2017.

[84] H. Nguyen-Van, A.N. Baranov, Z. Loghmari, L. Cerutti, J.B. Rodriguez, J. Tournet, G. Narcy, G. Boissier, G. Patriarche, M. Bahriz, et al. Quantum cascade lasers grown on silicon. *Scientific reports*, 8(1):7206, 2018.

[85] S.H. Huang, G. Balakrishnan, A. Khoshakhlagh, L.R. Dawson, and D.L. Huffaker. Simultaneous interfacial misfit array formation and antiphase domain suppression on miscut silicon substrate. *Applied Physics Letters*, 93(7):071102, 2008.

[86] A. Trampert, E. Tournie, and K.H. Ploog. Defect control during growth of highly mismatched (100)InAsGaAs-heterostructures. *Journal of crystal growth*, 146(1-4):368–373, 1995.

[87] A. Rocher and E. Snoeck. Misfit dislocations in (001) semiconductor heterostructures grown by epitaxy. *Materials Science and Engineering: B*, 67(1-2):62–69, 1999.

[88] K. Akahane, N. Yamamoto, S. Gozu, A. Ueta, and N. Ohtani. Initial growth stage of GaSb on Si(001) substrates with AlSb initiation layers. *Journal of crystal growth*, 283(3-4):297–302, 2005.

[89] K.W. Shin, H.W. Kim, J. Kim, C. Yang, S. Lee, and E. Yoon. The effects of low temperature buffer layer on the growth of pure Ge on Si(001). *Thin Solid Films*, 518(22):6496–6499, 2010.

[90] Y.B. Bolkhovityanov and O.P. Pchelyakov. GaAs epitaxy on Si substrates: modern status of research and engineering. *Physics-Uspekhi*, 51(5):437–456, 2008.

[91] J.B. Rodriguez, L. Cerutti, G. Patriarche, L. Largeau, K. Madiomanana, and E. Tournié. Characterization of antimonide based material grown by molecular epitaxy on vicinal silicon substrates via a low temperature AlSb nucleation layer. *Journal of Crystal Growth*, 477:65–71, 2017.

[92] M.A. Herman and H. Sitter. *Molecular beam epitaxy fundamentals and current status*. 2012.

[93] J. Tsao. *Material fundamentals of molecular beam epitaxy*. Academic Press, 2012.

[94] R.F.C. Farrow. *Molecular beam epitaxy: application to key materials*. Elsevier Science, 2012.

[95] M. Henini. *Molecular beam epitaxy: from research to mass production*. Newnes, 2012.

[96] A.S. Bracker, M.J. Yang, B.R. Bennett, J.C. Culbertson, and W.J. Moore. Surface reconstruction phase diagrams for InAs, AlSb, and GaSb. *Journal of Crystal Growth*, 220(4):384–392, 2000.

[97] J. J. Harris, B. Joyce, and P. J. Dobson. Oscillations in the surface structure of Sn-doped GaAs during growth by MBE. *Surface Science*, 103(1):90–96, 1981.

[98] D. Keith Bowen and B.K. Tanner. *X-ray metrology in semiconductor manufacturing*. CRC Press, 2006.

[99] B.D. Cullity. *Elements of X-ray diffraction, 3rd edition*. Upper Saddle River Prentice Hall, 2001.

[100] Jacques I Pankove. *Optical processes in semiconductors*. Courier Corporation, 1975.

[101] H Angus Macleod and H Angus Macleod. *Thin-film optical filters*. CRC press, 2010.

[102] K.R. McIntosh and S.C. Baker-Finch. OPAL 2: rapid optical simulation of silicon solar cells. In *Photovoltaic Specialists Conference (PVSC), 2012 38th IEEE*, pages 000265–000271. IEEE, 2012.

[103] D.E. Aspnes and A.A. Studna. Dielectric functions and optical parameters of Si, Ge, GaP, GaAs, GaSb, InP, InAs, and InSb from 1.5 to 6.0 eV. *Physical review B*, 27(2):985, 1983.

[104] S. Subbanna, G. Tuttle, and H. Kroemer. N-type doping of gallium antimonide and aluminum antimonide grown by molecular beam epitaxy using lead telluride as a tellurium dopant source. *J. Electron. Mater.*, 17(4):297–303, July 1988.

[105] Samuel A Miller, Maxwell Dylla, Shashwat Anand, Kiarash Gordiz, G Jeffrey Snyder, and Eric S Toberer. Empirical modeling of dopability in diamond-like semiconductors. *npj Computational Materials*, 4(1):71, 2018.

[106] J.A. Robinson and S.E. Mohney. An improved In-based ohmic contact to n-GaSb. *Solid State Electronics*, 48:1667–1672, September 2004.

[107] K. Ikossi, M. Goldenberg, and J. Mittereder. Metallization options and annealing temperatures for low contact resistance ohmic contacts to n-type GaSb. *Solid-State Electronics*, 46(10):1627–1631, 2002.

[108] B. Tadayon, C.S. Kyono, M. Fatemi, S. Tadayon, and J.A. Mittereder. Extremely low specific contact resistivities for p-type GaSb, grown by molecular beam epitaxy. *Journal of Vacuum Science & Technology B: Microelectronics and Nanometer Structures Processing, Measurement, and Phenomena*, 13(1):1–3, 1995.

[109] F.Y. Soldatenkov, S.V. Sorokina, N.K. Timoshina, V.P. Khvostikov, Y.M. Zadiranov, M.G. Rastegaeva, and A.A. Usikova. A decrease in ohmic losses and an increase in power in GaSb photovoltaic converters. *Semiconductors*, 45(9):1219–1226, 2011.

[110] L.M. Fraas, J.E. Avery, V.S. Sundaram, V.T. Dinh, T.M. Davenport, J.W. Yerkes, J.M. Gee, and K.A. Emery. Over 35% efficient GaAs/GaSb stacked concentrator cell assemblies for terrestrial applications. In *Photovoltaic Specialists Conference, 1990., Conference Record of the Twenty First IEEE*, pages 190–195. IEEE, 1990.

[111] V.M. Andreev, S.V. Sorokina, N.K. Timoshina, V.P. Khvostikov, and M.Z. Shvarts. Solar cells based on gallium antimonide. *Semiconductors*, 43(5):668–671, 2009.

[112] A.S. Vlasov, V.P. Khvostikov, L.B. Karlina, S.V. Sorokina, N.S. Potapovich, M.Z. Shvarts, N.K. Timoshina, V.M. Lantratov, S.A. Mintairov, N.A. Kalyuzhnyi, et al. Spectral-splitting concentrator photovoltaic modules based on AlGaAs/GaAs/GaSb and GaInP/InGaAs(P) solar cells. *Technical Physics*, 58(7):1034–1038, 2013.

[113] A.W. Bett, C. Baur, R. Beckert, F. Dimroth, G. Letay, M. Hein, M. Muesel, S. van Riesen, U. Schubert, G. Siefer, et al. Development of high-efficiency mechanically stacked GaInP/GaInAs-GaSb triple-junction concentrator solar cells. In *Conference Record, 17th European Solar Energy Conference, Munich*, pages 84–87, 2001.

[114] M.Z. Shvarts, P.Y. Gazaryan, N.A. Kaluzhniy, V.P. Khvostikov, V.M. Lantratov, S.A. Mintairov, S.V. Sorokina, and N.K. Timoshina. InGaP/GaAs-GaSb and InGaP/GaAs/Ge-InGaAsSb hybrid monolithic/stacked tandem concentrator solar cells. *Proc. of 21st EUPVSEC*, 2006.

[115] A. Mansoori, S.J. Addamane, E.J. Renteria, D.M. Shima, M. Behzadirad, E. Vadiee, C. Honsberg, and G. Balakrishnan. Reducing threading dislocation density in GaSb photovoltaic devices on GaAs by using AlSb dislocation filtering layers. *Solar Energy Materials and Solar Cells*, 185:21–27, 2018.

[116] M. Burgelman, P. Nollet, and S. Degrave. Modelling polycrystalline semiconductor solar cells. *Thin Solid Films*, 361:527–532, 2000.

[117] E.Q.B. Macabebe and E.E. Van Dyk. Parameter extraction from dark current-voltage characteristics of solar cells. *South African Journal of Science*, 104(9-10):401–404, 2008.

[118] R King, D Law, C Fetzer, R Sherif, K Edmondson, S Kurtz, GS Kinsey, HL Cotal, DD Krut, JH Ermer, et al. Pathways to 40%-efficient concentrator photovoltaics. In *Proc. 20th European Photovoltaic Solar Energy Conference*, pages 10–11, 2005.

[119] T.H. Glisson, J.R. Hauser, M.A. Littlejohn, and C.K. Williams. Energy bandgap and lattice constant contours of III-V quaternary alloys. *Journal of Electronic Materials*, 7(1):1–16, 1978.

[120] R.L. Moon, G.A. Antypas, and L.W. James. Bandgap and lattice constant of GaInAsP as a function of alloy composition. *Journal of Electronic Materials*, 3(3):635–644, 1974.

[121] M. Kudo and T. Mishima. MBE growth of Si-doped InAlAsSb layers lattice-matched with InAs. *Journal of crystal growth*, 175:844–848, 1997.

[122] L.G. Vaughn. *Mid-infrared multiple quantum wells lasers using digitally-grown AlInAsSb barriers and strained InAsSb wells*. PhD thesis, The University of New Mexico, 2006.

[123] R. Magno, E.R. Glaser, B.P. Tinkham, J.G. Champlain, J.B. Boos, M.G. Ancona, and P.M. Campbell. Narrow band gap InGaSb, InAlAsSb alloys for electronic devices. *Journal of Vacuum Science & Technology B: Microelectronics and Nanometer Structures Processing, Measurement, and Phenomena*, 24(3):1622–1625, 2006.

[124] M.P. Lumb, M. Gonzalez, I. Vurgaftman, J.R. Meyer, J. Abell, M.K. Yakes, R. Hoheisel, J.G. Tischler, P.P. Jenkins, P. Stavrinou, et al. Simulation of novel InAlAsSb solar cells. In *Proc. SPIE*, volume 8256, page 82560S, 2012.

[125] W.L. Sarney, S.P. Svensson, D. Wang, D. Donetsky, G. Kipshidze, L. Shterengas, Y. Lin, and G. Belenky. AlInAsSb for M-LWIR detectors. *Journal of Crystal Growth*, 425:357–359, 2015.

[126] M. Ren, S. Maddox, Y. Chen, M. Woodson, J.C. Campbell, and S. Bank. AlInAsSb/-GaSb staircase avalanche photodiode. *Applied Physics Letters*, 108(8):081101, 2016.

[127] K. Onabe. Unstable regions in III-V quaternary solid solutions composition plane calculated with strictly regular solution approximation. *Japanese Journal of Applied Physics*, 21(6 Part 2):L323, 1982.

[128] A. Yildirim. *Phase separation and defect formation in stable, metastable, and unstable GaInAsSb alloys for infrared applications.* PhD thesis, University of Iowa, 2014.

[129] A.N. Semenov, V.A. Solov'Ev, B.Y. Meltser, Y.V. Terent'ev, L.G. Prokopova, and S.V. Ivanov. Molecular beam epitaxy of AlInAsSb alloys near the miscibility gap boundary. *Journal of crystal growth*, 278(1):203–208, 2005.

[130] J.S. Rojas-Ramirez, S. Wang, R. Contreras-Guerrero, M. Caro, K. Bhatnagar, M. Holland, R. Oxland, G. Doornbos, M. Passlack, C.H. Diaz, et al. $Al_xIn_{1-x}As_ySb_{1-y}$ alloys lattice matched to InAs(100) grown by molecular beam epitaxy. *Journal of Crystal Growth*, 425:33–38, 2015.

[131] T. Zederbauer, A.M. Andrews, D. MacFarland, H. Detz, W. Schrenk, and G. Strasser. Enhanced crystal quality of $Al_xIn_{1-x}As_ySb_{1-y}$ for terahertz quantum cascade lasers. In *Photonics*, volume 3, page 20. Multidisciplinary Digital Publishing Institute, 2016.

[132] E.R. Glaser, R. Magno, B.V. Shanabrook, and J.G. Tischler. Optical characterization of $In_{0.27}Ga_{0.73}Sb$ and $In_xAl_{1-x}As_ySb_{1-y}$ epitaxial layers for development of 6.2-å-based heterojunction bipolar transistors. *Journal of Vacuum Science & Technology B: Microelectronics and Nanometer Structures Processing, Measurement, and Phenomena*, 24(3):1604–1606, 2006.

[133] D. Washington-Stokes, T.P. Hogan, P.C. Chow, T.D. Golding, U. Kirschbaum, C.L. Littler, and R. Lukic. $Al_xIn_{1-x}As1 - ySb_y$/GaSb effective mass superlattices grown by molecular beam epitaxy. *Journal of crystal growth*, 201:854–857, 1999.

[134] L.G. Vaughn, L.R. Dawson, E.A. Pease, L.F. Lester, H. Xu, Y. Jiang, and A.L. Gray. Type I mid-infrared MQW lasers using AlInAsSb barriers and InAsSb wells. In *Proc. SPIE*, volume 5722, page 307, 2005.

[135] T.Y. Seong, A.G. Norman, I.T. Ferguson, and G.R. Booker. Transmission electron microscopy and transmission electron diffraction structural studies of heteroepitaxial $InAs_ySb_{1-y}$ molecular-beam epitaxial layers. *Journal of applied physics*, 73(12):8227–8236, 1993.

[136] H. Fu. Optical characterization of AlInAsSb digital alloy films. *2015 NNIN Research Accomplishments*, pages 138–139, 2015.

[137] S.J. Maddox, S.D. March, and S.R. Bank. Broadly tunable AlInAsSb digital alloys grown on GaSb. *Crystal Growth & Design*, 16(7):3582–3586, 2016.

[138] T. Nuytten, M. Hayne, B. Bansal, H.Y. Liu, M. Hopkinson, and V.V. Moshchalkov. Charge separation and temperature-induced carrier migration in $Ga_{1-x}In_xN_yAs_{1-y}$ multiple quantum wells. *Physical Review B*, 84(4):045302, 2011.

[139] M. González, M.P. Lumb, L.C. Hirst, S. Tomasulo, J.G. Tischler, W. Yoon, J. Abell, I. Vurgaftman, M.F. Bennett, K.J. Schmieder, et al. Rapid thermal annealing of InAlAsSb lattice-matched to InP for top cell applications. In *Photovoltaic Specialist Conference (PVSC), 2015 IEEE 42nd*, pages 1–4. IEEE, 2015.

[140] N. Baladés, D.L. Sales, M. Herrera, F.J. Delgado, M. González, K. Clark, P. Pinsunkajana, N. Hoven, S. Hubbard, S. Tomasulo, et al. Effect of annealing on the compositional modulation of InAlAsSb. *Applied Surface Science*, 395:105–109, 2017.

[141] J. Hernández-Saz, M. Herrera, F.J. Delgado, S. Duguay, T. Philippe, M. Gonzalez, J. Abell, R.J. Walters, and S.I. Molina. Atom-scale compositional distribution in InAlAsSb-based triple-junction solar cells by atom probe tomography. *Nanotechnology*, 27(30):305402–305402, 2016.

[142] J. Hernández-Saz, M. Herrera, J. Pizarro, P.L. Galindo, M. Gonzalez, J. Abell, R.J. Walters, S.I. Molina, and S. Duguay. Influence of the growth temperature on the composition distribution at sub-nm scale of InAlAsSb for solar cells. *Journal of Alloys and Compounds*, 2018.

[143] Y. Lyu, X. Han, Y. Sun, Z. Jiang, C. Guo, W. Xiang, Y. Dong, J. Cui, Y. Yao, D. Jiang, et al. Digitally grown AlInAsSb for high gain separate absorption, grading, charge, and multiplication avalanche photodiodes. *Journal of Crystal Growth*, 482:70–74, 2018.

[144] O. Dier, M. Sterkel, M. Grau, C. Lin, C. Lauer, and M.C. Amann. Tunnel junctions for ohmic intra-device contacts on GaSb-substrates. *Applied physics letters*, 85(12):2388–2389, 2004.

[145] K. Vizbaras, M. Törpe, S. Arafin, and M.C. Amann. Ultra-low resistive GaSb/InAs tunnel junctions. *Semiconductor Science and Technology*, 26(7):075021, 2011.

[146] M.P. Lumb, S. Mack, M. Gonzalez, K. Schmieder, and R.J. Walters. Tunnel diode with broken-gap quantum well, July 21 2016. US Patent App. 14/995,357.

[147] G.P. Donati, R. Kaspi, and K.J. Malloy. Interpolating semiconductor alloy parameters: Application to quaternary III-V band gaps. *Journal of Applied Physics*, 94(9):5814–5819, 2003.

[148] J. Burdick and T. Glatfelter. Spectral response and I-V measurements of tandem amorphous-silicon alloy solar cells. *Solar Cells*, 18(3-4):301–314, 1986.

[149] M. Meusel, C. Baur, G. Létay, A.W. Bett, W. Warta, and E. Fernandez. Spectral response measurements of monolithic GaInP/Ga(In)As/Ge triple-junction solar cells: measurement artifacts and their explanation. *Progress in Photovoltaics: Research and Applications*, 11(8):499–514, 2003.

[150] I. Vurgaftman, J.R. Meyer, and L.R. Ram-Mohan. Band parameters for III-V compound semiconductors and their alloys. *Journal of applied physics*, 89(11):5815–5875, 2001.

[151] V.K. Yang, M. Groenert, C.W. Leitz, A.J. Pitera, M.T. Currie, and E.A. Fitzgerald. Crack formation in GaAs heteroepitaxial films on Si and SiGe virtual substrates. *Journal of applied physics*, 93(7):3859–3865, 2003.

[152] D. Keith Bowen and B. K. Tanner. *High resolution X-ray diffractometry and topography*. Taylor and Francis, 2005.

[153] T.J. Grassman, M.R. Brenner, S. Rajagopalan, R. Unocic, R. Dehoff, M. Mills, H. Fraser, and S.A. Ringel. Control and elimination of nucleation-related defects in GaP/Si(001) heteroepitaxy. *Applied Physics Letters*, 94(23):232106, 2009.

[154] T.W. Poon, S. Yip, P.S. Ho, and F.F. Abraham. Equilibrium structures of Si(100) stepped surfaces. *Physical review letters*, 65(17):2161, 1990.

[155] D. Jarek and M. Hans-Joachim. *Silicon surfaces and formation of interfaces: basic science in the industrial world*. World Scientific, 2000.

[156] M. Akiyama, Y. Kawarada, and K. Kaminishi. Growth of single domain GaAs layer on (100)-oriented Si substrate by MOCVD. *Japanese Journal of Applied Physics*, 23(11A):L843, 1984.

[157] T. Nishinaga, T. Nakano, and S. Zhang. Epitaxial lateral overgrowth of GaAs by LPE. *Japanese journal of applied physics*, 27(6A):L964, 1988.

[158] R. Fischer, H. Morkoc, D.A. Neumann, H. Zabel, C. Choi, N. Otsuka, M. Longerbone, and L.P. Erickson. Material properties of high-quality GaAs epitaxial layers grown on Si substrates. *Journal of applied physics*, 60(5):1640–1647, 1986.

[159] S.F. Fang, K. Adomi, S. Iyer, H. Morkoc, H. Zabel, C. Choi, and N. Otsuka. Gallium arsenide and other compound semiconductors on silicon. *Journal of Applied Physics*, 68(7):R31–R58, 1990.

[160] R.J. Malik, J.P. Van Der Ziel, B.F. Levine, C.G. Bethea, and J. Walker. Molecular-beam epitaxy of GaSb/AlSb optical device layers on Si(100). *Journal of applied physics*, 59(11):3909–3911, 1986.

[161] C. Chang, H. Takaoka, L.L. Chang, and L. Esaki. Molecular beam epitaxy of AlSb. *Applied Physics Letters*, 40(11):983–985, 1982.

[162] G. Griffiths, K. Mohammed, S. Subbana, H. Kroemer, and J.L. Merz. GaSb/AlSb multiquantum well structures: molecular beam epitaxial growth and narrow-well photoluminescence. *Applied physics letters*, 43(11):1059–1061, 1983.

[163] H. Gotoh, K. Sasamoto, S. Kuroda, and M. Kimata. Molecular beam epitaxy of AlSb on GaAs and GaSb on AlSb films. *physica status solidi (a)*, 75(2):641–645, 1983.

[164] K. Akahane, N. Yamamoto, S. Gozu, and N. Ohtani. Heteroepitaxial growth of GaSb on Si(001) substrates. *Journal of crystal growth*, 264(1):21–25, 2004.

[165] Y.H. Kim, J.Y. Lee, Y.G. Noh, M.D. Kim, S.M. Cho, Y.J. Kwon, and J.E. Oh. Growth mode and structural characterization of GaSb on Si(001) substrate: a transmission electron microscopy study. *Applied physics letters*, 88(24):241907, 2006.

[166] Y.H. Kim, Y.K. Noh, M.D. Kim, J.E. Oh, and K.S. Chung. Transmission electron microscopy study of the initial growth stage of GaSb grown on Si(001) substrate by molecular beam epitaxy method. *Thin solid films*, 518(8):2280–2284, 2010.

[167] G. Balakrishnan, S. Huang, L.R. Dawson, Y.C. Xin, P. Conlin, and D.L. Huffaker. Growth mechanisms of highly mismatched AlSb on a Si substrate. *Applied Physics Letters*, 86(3):034105, 2005.

[168] G. Balakrishnan, S. Huang, A. Khoshakhlagh, L.R. Dawson, Y.C. Xin, P. Conlin, and D.L. Huffaker. High quality AlSb bulk material on Si substrates using a monolithic self-assembled quantum dot nucleation layer. *Journal of Vacuum Science &*

Technology B: Microelectronics and Nanometer Structures Processing, Measurement, and Phenomena, 23(3):1010–1012, 2005.

[169] S.H. Vajargah, S. Ghanad-Tavakoli, J.S. Preston, R.N. Kleiman, and G.A. Botton. Growth mechanisms of GaSb heteroepitaxial films on Si with an AlSb buffer layer. *Journal of Applied Physics*, 114(11):113101, 2013.

[170] J.B. Rodriguez, K. Madiomanana, L. Cerutti, A. Castellano, and E. Tournié. X-ray diffraction study of GaSb grown by molecular beam epitaxy on silicon substrates. *Journal of Crystal Growth*, 439:33–39, 2016.

[171] F. Dimroth, T. Roesener, S. Essig, C. Weuffen, A. Wekkeli, E. Oliva, G. Siefer, K. Volz, T. Hannappel, D. Häussler, et al. Comparison of direct growth and wafer bonding for the fabrication of GaInP/GaAs dual-junction solar cells on silicon. *IEEE Journal of Photovoltaics*, 4(2):620–625, 2014.

[172] J.W. Lee, H. Shichijo, H.L. Tsai, and R.J. Matyi. Defect reduction by thermal annealing of GaAs layers grown by molecular beam epitaxy on Si substrates. *Applied Physics Letters*, 50(1):31–33, 1987.

[173] M. Yamaguchi, T. Nishioka, and M. Sugo. Analysis of strained-layer superlattice effects on dislocation density reduction in GaAs on Si substrates. *Applied physics letters*, 54(1):24–26, 1989.

[174] M. Yamaguchi. Dislocation density reduction in heteroepitaxial III-V compound films on Si substrates for optical devices. *Journal of Materials Research*, 6(2):376–384, 1991.

[175] K. Akahori, G. Wang, K. Okumura, T. Soga, T. Jimbo, and M. Umeno. Improvement of the MOCVD-grown InGaP-on-Si towards high-efficiency solar cell application. *Solar energy materials and solar cells*, 66(1-4):593–598, 2001.

[176] W. Stolz, Y. Horikoshi, M. Naganuma, and K. Nozawa. Optimized growth start and controlled formation of misfit dislocations for heteroepitaxial GaAs on (100)Si grown by migration-enhanced epitaxy. *Journal of Crystal Growth*, 95(1-4):87–90, 1989.

[177] P.J. Taylor, W.A. Jesser, J.D. Benson, M. Martinka, J.H. Dinan, J. Bradshaw, M. Lara-Taysing, R.P. Leavitt, G. Simonis, W. Chang, et al. Optoelectronic device performance on reduced threading dislocation density GaAs/Si. *Journal of Applied Physics*, 89(8):4365–4375, 2001.

[178] W.Y. Uen, S. Sakawa, and T. Nishinaga. Comparative study of amorphous and crystalline buffer layers in MBE growth of GaAs on Si. *Journal of crystal growth*, 115(1-4):122–127, 1991.

[179] W.Y. Uen and T. Nishinaga. Growth of GaAs on Si by employing AlAs/GaAs double amorphous buffer. *Journal of crystal growth*, 128(1-4):521–526, 1993.

[180] M. Peach and J.S. Koehler. The forces exerted on dislocations and the stress fields produced by them. *Physical Review*, 80(3):436, 1950.

[181] J.W. Matthews and A.E. Blakeslee. Defects in epitaxial multilayers: I. Misfit dislocations. *Journal of Crystal growth*, 27:118–125, 1974.

[182] J.S. Whelan, T. George, E.R. Weber, S. Nozaki, A.T. Wu, and M. Umeno. Transmission electron microscopy investigation of dislocation bending by GaAsP/GaAs strained-layer superlattices on heteroepitaxial GaAs/Si. *Journal of applied physics*, 68(10):5115–5118, 1990.

[183] Z. Mi, J. Yang, P. Bhattacharya, and D.L. Huffaker. Self-organised quantum dots as dislocation filters: the case of GaAs-based lasers on silicon. *Electronics Letters*, 42(2):1, 2006.

[184] W. Qian, M. Skowronski, and R. Kaspi. Dislocation density reduction in GaSb films grown on GaAs substrates by molecular beam epitaxy. *Journal of the Electrochemical Society*, 144(4):1430–1434, 1997.

[185] D.H. Nguyen, J. Park, Y.K. Noh, M.D. Kim, D. Lee, and J.E. Oh. Strong photoluminescence at 1.53 μm from GaSb/AlGaSb multiple quantum wells grown on Si substrate. *Applied Physics Letters*, 95(6):061910, 2009.

[186] Y.K. Noh, M.D. Kim, J.E. Oh, W.C. Yang, and Y.H. Kim. Growth of low defect AlGaSb films on Si(100) using AlSb and InSb quantum dots intermediate layers. *Journal of Crystal Growth*, 323(1):405–408, 2011.

[187] S.K. Madisetti, V. Tokranov, A. Greene, S. Novak, M. Yakimov, S. Oktyabrsky, S. Bentley, and A.P. Jacob. GaSb on Si: structural defects and their effect on surface morphology and electrical properties. *MRS Online Proceedings Library Archive*, 1635:115–120, 2014.

[188] S. Sasaki, K. Dropiewski, S. Madisetti, V. Tokranov, M. Yakimov, S. Oktyabrsky, S. Bentley, R. Galatage, and A.P. Jacob. Electrical properties related to growth defects in metamorphic GaSb films on Si. *Journal of Vacuum Science & Technology B, Nanotechnology and Microelectronics: Materials, Processing, Measurement, and Phenomena*, 35(1):011203, 2017.

[189] N. Jain and M.K. Hudait. III-V multijunction solar cell integration with silicon: present status, challenges and future outlook. *Energy Harvesting and Systems*, 1(3-4):121–145, 2014.

[190] M. Yamaguchi, K.H. Lee, K. Araki, and N. Kojima. A review of recent progress in heterogeneous silicon tandem solar cells. *Journal of Physics D: Applied Physics*, 51(13):133002, 2018.

[191] M.R. Lueck, C.L. Andre, A.J. Pitera, M.L. Lee, E.A. Fitzgerald, and S.A. Ringel. Dual junction GaInP/GaAs solar cells grown on metamorphic SiGe/Si substrates with high open circuit voltage. *IEEE Electron Device Letters*, 27(3):142–144, 2006.

[192] L. Wang, B. Conrad, A. Soeriyadi, X. Zhao, D. Li, M. Diaz, A. Lochtefeld, A. Gerger, I. Perez-Wurfl, and A. Barnett. Current matched three-terminal dual junction GaAsP/SiGe tandem solar cell on si. *Solar Energy Materials and Solar Cells*, 146:80–86, 2016.

[193] T. Soga, K. Baskar, T. Kato, T. Jimbo, and M. Umeno. MOCVD growth of high efficiency current-matched AlGaAs/Si tandem solar cell. *Journal of crystal growth*, 174(1-4):579–584, 1997.

[194] T.J. Grassman, D.J. Chmielewski, S.D. Carnevale, J.A. Carlin, and S.A. Ringel. GaAs$_{0.75}$P$_{0.25}$/Si dual-junction solar cells grown by MBE and MOCVD. *IEEE Journal of Photovoltaics*, 6(1):326–331, 2016.

[195] M.A. Green, Y. Hishikawa, E.D. Dunlop, D.H. Levi, J. Hohl-Ebinger, M. Yoshita, and A.W.Y. Ho-Baillie. Solar cell efficiency tables (version 53). *Progress in Photovoltaics: Research and Applications*, 27(1):3–12, 2019.

[196] Markus Feifel, Jens Ohlmann, Jan Benick, Martin Hermle, Jürgen Belz, Andreas Beyer, Kerstin Volz, Thomas Hannappel, Andreas W Bett, David Lackner, et al. Direct growth of III-V/Silicon triple-junction solar cells with 19.7% efficiency. *IEEE Journal of Photovoltaics*, (99):1–6, 2018.

[197] K. Tanabe, K. Watanabe, and Y. Arakawa. III-V/Si hybrid photonic devices by direct fusion bonding. *Scientific reports*, 2:349, 2012.

[198] E. Kasper, M. Bauer, and M. Oehme. Quantitative secondary ion mass spectrometry analysis of SiO$_2$ desorption during in situ heat cleaning. *Thin Solid Films*, 321(1–2):148–152, 1998.

[199] K. Madiomanana, M. Bahri, J.B. Rodriguez, L. Largeau, L. Cerutti, O. Mauguin, A. Castellano, G. Patriarche, and E. Tournié. Silicon surface preparation for III-V molecular beam epitaxy. *Journal of Crystal Growth*, 413(0):17–24, 2015.

[200] E.D. Palik. Handbook of optical constants of solids Academic Press. *Inc., New York*, 1985.

[201] Ioffe. GaSb band structure and carrier concentration. http://www.ioffe.ru/SVA/NSM/Semicond/GaSb/bandstr.html. Accessed: 2018-08-10.

[202] L. Tang, L.M. Fraas, Z. Liu, C. Xu, and X. Chen. Performance improvement of the GaSb thermophotovoltaic cells with n-type emitters. *IEEE transactions on electron devices*, 62(9):2809–2815, 2015.

[203] B. Galiana, I. Rey-Stolle, I. Beinik, C. Algora, C. Teichert, J.M. Molina-Aldareguia, and P. Tejedor. Characterization of antiphase domains on GaAs grown on Ge substrates by conductive atomic force microscopy for photovoltaic applications. *Solar Energy Materials and Solar Cells*, 95(7):1949–1954, 2011.

[204] H. El Ghitani, M. Pasquinelli, and S. Martinuzzi. Influence of dislocations on photovoltaic properties of multicrystalline silicon solar cells. *Journal de Physique III*, 3(10):1941–1946, 1993.

[205] B.C. Juang, R.B. Laghumavarapu, B.J. Foggo, P.J. Simmonds, A. Lin, B. Liang, and D.L. Huffaker. GaSb thermophotovoltaic cells grown on GaAs by molecular beam epitaxy using interfacial misfit arrays. *Applied Physics Letters*, 106(11):111101, 2015.

[206] M. Yamaguchi and C. Amano. Efficiency calculations of thin-film GaAs solar cells on Si substrates. *Journal of applied physics*, 58(9):3601–3606, 1985.

[207] S.H. Lim, C.R. Allen, D. Ding, X. Liu, J.K. Furdyna, D. Vasileska, and Y.H. Zhang. Cascade tunnel diode incorporating InAs/GaSb broken gap interface for multi-junction solar cells. In *Photovoltaic Specialists Conference (PVSC), 2011 37th IEEE*, pages 000252–000255. IEEE, 2011.